

INAUGURAL – DISSERTATION

submitted to the
Combined Faculty of Natural Sciences and Mathematics
of the Ruperto Carola University Heidelberg, Germany
for the degree of
Doctor of Natural Sciences

Put forward by

M.Sc. Simon Schmidt

Born in: Bietigheim-Bissingen, Germany

Oral examination: May 11th, 2020

On the Quantification of Fluid Mechanical Properties by Means of Magnetic Resonance Imaging

Referees : Prof. Dr. Peter Bachert

Prof. Dr. Lothar Schad

Für meine Familie

On the Quantification of Fluid Mechanical Properties by Means of Magnetic Resonance Imaging

Magnetic resonance imaging (MRI) provides a versatile tool to determine a variety of fluid mechanical properties, but similarly the quantification is biased by the acquisition itself and the technique has limitations among which are limited spatial resolution and low signal-to-noise-ratio.

To overcome such issues, phase contrast MRI methods have been investigated at 7 T. At this field strength variations of the transmit field pose a substantial problem. Additionally, so-called displacement artifacts become important, since they scale with spatial resolution. Transmit field variations are addressed in this work by multi-spoke RF pulses, which are not straightforwardly applicable to velocity quantification. They require a detailed investigation of displacement artifacts that arise due to differences in the encoding time points of velocity and space. This work investigates three different encoding schemes, for conventional excitation as well as for multi-spoke excitation, which yield different displacement artifacts. Their impact on derived haemodynamic parameters, such as wall shear stress, which had been unknown so far, are investigated. Moreover, spoke pulses are further fine-tuned by using asymmetric pulse shapes. Besides the correct determination of the velocity at 7 T, the precise quantification of acceleration is another important factor, which is solved in this work by developing an acceleration-encoded sequence free of artifacts. Furthermore, another confounding factor in MRI-based velocimetry, the intravoxel velocity distributions, affect the velocity encoding process. This effect has been investigated and, based on measured velocity spectra, noise-optimized velocity encoding sensitivity (VENC) values have been proposed. Finally, the potential of precise MR-based velocity measurements is demonstrated for a well-known fluid dynamic test case (flow over periodic hills) with a REYNOLDS number of 60,000. For this case, the REYNOLDS stress tensor has been quantified.

In conclusion, the presented techniques improve the precision at which fluid mechanical properties can be quantified by means of MRI.

Über die Quantifizierung strömungsmechanischer Eigenschaften mit Hilfe der Magnetresonanztomographie

Die Magnetresonanztomographie (MRT) bietet ein vielseitiges Werkzeug zur Bestimmung einer Vielzahl von strömungsmechanischen Eigenschaften. Zugleich jedoch ist die Quantifizierung durch die Aufnahme selbst beeinträchtigt und die Technik hat ihre Grenzen. Zu diesen zählen die limitierte räumliche Auflösung und das geringe Signal-zu-Rausch-Verhältnis.

Um diese Schwierigkeiten zu überwinden, wurden Phasenkontrast-MRT-Methoden bei 7 T untersucht. Bei dieser Feldstärke stellen Variationen des Sendefeldes ein erhebliches Problem dar. Zusätzlich werden sogenannte Verschiebungsartefakte wichtig, da diese mit der räumlichen Auflösung skalieren. Sendefeldvariationen werden in dieser Arbeit durch Mehrspeichen-HF-Impulse kompensiert, welche jedoch nicht ohne Weiteres auf die Geschwindigkeitsquantifizierung anwendbar sind. Vielmehr ist eine detaillierte Untersuchung von Verschiebungsartefakten erforderlich, welche durch Unterschiede in den Kodierungszeitpunkten von Geschwindigkeit und Ort entstehen. In dieser Arbeit werden drei verschiedene Kodierungsschemata untersucht, sowohl für konventionelle als auch für Mehrspeichenanregung, welche unterschiedliche Verschiebungsartefakte erzeugen. Ihr Einfluss auf abgeleitete hämodynamische Parameter wird untersucht, wie z.B. auf die Wandschubspannung, der bisher unbekannt war. Darüber hinaus werden die Mehrspeichen-HF-Impulse durch die Verwendung asymmetrischer Pulsformen optimiert. Neben der korrekten Bestimmung der Geschwindigkeit bei 7 T ist die genaue Quantifizierung der Beschleunigung ein weiterer wichtiger Faktor, welcher in dieser Arbeit durch die Entwicklung einer artefaktfreien beschleunigungskodierten Sequenz gelöst wird. Ein weiterer Störfaktor in der MRT-basierten Geschwindigkeitsmessung besteht darin, dass Geschwindigkeitsverteilungen innerhalb der Voxel den Geschwindigkeitskodierungsprozess beeinflussen. Dieser Effekt wurde untersucht und, auf der Grundlage gemessener Geschwindigkeitsspektren, rauschoptimierte Werte für die Empfindlichkeit der Geschwindigkeitskodierung (engl. velocity encoding sensitivity, VENC) vorgeschlagen. Schließlich wird das Potenzial präziser MR-basierter Geschwindigkeitsmessungen für einen bekannten strömungsmechanischen Testfall (Strömung über periodische Hügel) mit einer REYNOLDS-Zahl von 60.000 demonstriert. Für diesen Fall wurde außerdem der REYNOLDS-Spannungstensor quantifiziert.

Zusammenfassend lässt sich sagen, dass die vorgestellten Techniken die Präzision verbessern, mit der die strömungsmechanischen Eigenschaften mittels MRT quantifiziert werden können.

Contents

1	Introduction	1
2	Theory	5
2.1	FOURIER transform	5
2.2	Nuclear magnetic resonance	6
2.2.1	Nuclear spin and magnetic moment	6
2.2.2	Macroscopic magnetization	8
2.2.3	Manipulation of the macroscopic magnetization	10
2.3	Magnetic resonance imaging	11
2.3.1	Spatial encoding	12
2.3.2	Parallel imaging	14
2.3.3	Excitation k-space	15
2.3.4	SHINNAR-LE ROUX algorithm	17
2.4	Ultra high field MRI	18
2.4.1	Static magnetic field inhomogeneity	19
2.4.2	Radio frequency field inhomogeneity	19
2.4.3	Parallel transmission	20
2.4.4	B_1 shimming	21
2.4.5	Multi-spoke RF pulses	21
2.5	MRI of non-stationary magnetization	24
2.5.1	Gradient moments	25
2.5.2	Spatial encoding	28
2.5.3	Velocity encoding	29
2.5.4	Acceleration encoding	31
2.5.5	Phase errors	31
2.5.6	FOURIER velocity encoding	33
2.5.7	Quantification of the REYNOLDS stress tensor	34
2.6	Fundamentals of fluid mechanics	36
2.6.1	Continuity equation	36
2.6.2	NAVIER-STOKES equation	36
2.6.3	Wall shear stress	37
2.6.4	Turbulent flow	38

3	Methods	41
3.1	Hardware	41
3.1.1	MR systems	41
3.1.2	RF coils	41
3.1.3	Flow Pump	43
3.1.4	Phantoms	44
3.2	Pulse sequences	46
3.2.1	Velocity mapping	46
3.2.2	Acceleration mapping	52
3.2.3	SYNC SPI	54
3.2.4	REYNOLDS stress tensor mapping	54
3.2.5	B_1 mapping	54
3.2.6	B_0 mapping	55
3.3	Measurements	56
3.3.1	Velocity encoded and compensated multi-spoke RF pulses	56
3.3.2	Velocity encoded and compensated asymmetric multi-spoke RF pulses	56
3.3.3	Impact of the displacement artifact on WSS quantification	57
3.3.4	VENC optimization	57
3.3.5	Acceleration quantification	57
3.3.6	REYNOLDS stress tensor quantification	58
3.3.7	Measurement parameters	58
3.4	Data analysis	69
3.4.1	Background phase removal	69
3.4.2	VENC optimization	69
3.4.3	Wall shear stress estimation	70
3.4.4	REYNOLDS stress tensor quantification	71
4	Results	73
4.1	Velocity encoded and compensated multi spoke RF pulses	73
4.1.1	Gradient waveform design	73
4.1.2	Phantom measurements	75
4.1.3	In vivo measurements	78
4.2	Velocity encoded and compensated asymmetric multi-spoke RF pulses	99
4.2.1	Simulations	99
4.2.2	Phantom measurements	99
4.2.3	In vivo measurements	100

4.3	Impact of the displacement artifact on wall shear stress quantification . . .	108
4.3.1	Phantom measurements	108
4.4	VENC optimization	118
4.4.1	Phantom measurements	118
4.5	Acceleration quantification	124
4.5.1	Phantom measurements	124
4.5.2	In vivo measurements	124
4.6	REYNOLDS stress tensor quantification	128
4.6.1	Phantom measurements	128
5	Discussion and Outlook	137
5.1	Velocity quantification	137
5.1.1	Multi-spoke RF pulses	139
5.1.2	VENC optimization	141
5.2	Acceleration quantification	142
5.3	Wall shear stress estimation	143
5.4	REYNOLDS stress tensor quantification	144
5.5	Outlook	145
6	Appendix	147
6.1	Abbreviations	147
6.2	Publications	149
	Bibliography	153
	Danksagung	161

1 Introduction

Flowing fluids are omnipresent in our daily lives and have, therefore, always been of scientific interest. EULER formulated the equations of motion for ideal fluids in the 18th century, which were extended in the first half of the 19th century by viscous terms to the NAVIER-STOKES equations, which realistically model flow. In the further course of history, fluid mechanics was extended by the theory of turbulent flow through the work of REYNOLDS, KOLMOGOROV, and many others. Despite these many scientific achievements, it is still only partially possible to describe or solve fluid mechanical problems sufficiently precise for many practical flow problems. In many cases, therefore, flows can only be reliably investigated using experimental methods.

The investigation of fluid mechanical properties plays an important role in technical flows, in which e.g. transport processes have to be optimized, or in safety-relevant flows such as in cooling circuits of nuclear power plants. However, the characterization of blood flow in the human cardiovascular system is equally important, especially with regard to cardiovascular diseases, which are the leading cause of death worldwide today [1].

Common experimental methods for the determination of fluid mechanical properties range from simple mechanical anemometers and pressure probes to thermal measurement methods, such as the hot-wire anemometer, to optical methods, such as laser doppler velocimetry or particle image velocimetry. However, most of these methods have the disadvantage that either a measuring probe has to be inserted into the fluid, which itself influences the flow to be investigated, or they are dependent on the optical accessibility of the flow. Besides, many of these methods only provide information about the fluid mechanical properties at a single point in space. As a consequence, the acquisition of a three-dimensional scalar or vector field is in many cases very time-consuming and may require measurement times up to the order of days or months. The long measurement times and the invasiveness of these methods render them unfeasible for clinical application in-vivo and, therefore, limit their use to technical issues.

Doppler ultrasonography allows the non-invasive quantification of blood flow velocities in vivo with high temporal resolution, but, as used in clinical routine, has certain limitations. It does not provide information about the complete velocity vector field, is limited to certain body regions and often has suboptimal image quality.

Already in the early years of magnetic resonance imaging (MRI), CARR and PURCELL

[2] as well as HAHN [3] observed the flow sensitivity of the magnetic resonance (MR) signal. In the 1980s, the first in vivo applications were reported [4–7] and the velocity vector field in the human vascular system was measured for the first time with MRI. These techniques were subsequently further optimized. Today, two-dimensional and time-resolved acquisitions of the velocity vector field have become clinical standard on all modern MR systems. The latest developments have extended these methods towards the acquisition of blood flow dynamics with full volumetric coverage, which is known as *4D flow MRI* [8].

MR-based, time-resolved velocity mapping techniques typically suffer from low signal-to-noise-ratio (SNR), limited spatial resolution, and long acquisition times. Therefore, an increase in SNR is favorable, as it could allow higher spatial resolutions and higher acceleration factors to speed up image acquisition. In recent years, substantial efforts have been made to realize MR systems with increasingly higher field strengths. Recently, 7 T has entered the range of clinically approved field strengths and investigatory whole-body systems with field strengths of up to 10.5 T have been designed. First studies have already shown the potential of these so-called ultra high fields (UHF) (≥ 7 T) for MR velocimetry. In comparison to measurements at 3 T, a 2.2-fold higher SNR in the human aorta [9] and a 2.6-fold increase of the SNR in the brain [10] were reported for flow quantification at 7 T. This gain is expected to further increase at field strengths beyond 7 T.

In addition to the increased SNR at UHF, new challenges also arise. A major challenge is the local variation of the transmit field B_1 , which is necessary to generate the MR signal. These variations were shown to negatively influence the velocity quantification [11] and are, therefore, a fundamental problem of MR-based velocimetry at UHF. One possible way to overcome these difficulties is to use radio frequency (RF) coils with multiple transmit elements in combination with B_1 shimming. Here, the transmit phase and/or amplitude of each transmit element can be adjusted individually, which has been used in flow quantification studies at 7 T before [9, 11]. Furthermore, it was shown for morphological imaging that further improvement can be achieved by using slice or slab selective three-dimensional tailored (“multi-spoke”) parallel transmission (pTx) pulses [12, 13]. These pulses gain even more importance at field strengths > 7 T [14].

The aim of this work was, therefore, to investigate the use of such multi-spoke RF pulses for velocity quantification. To achieve this, a detailed analysis of the influence of the flow on the individual sub-pulses was necessary, which in turn led to another fundamental problem of MRI in the presence of flow. Due to the nature of the MR data acquisition, MRI is prone to the so-called displacement artifact. Although first described in the early 1990s [15, 16], this artifact receives little attention today. To address this problem,

different approaches were investigated within the scope of this work and its impact on the quantified velocity vector fields was studied. In addition, the wall shear stress (WSS) and the acceleration vector field are both potentially important clinical parameters. Therefore, the effect of the displacement artifact on both parameters was also considered.

Besides the quantification of fluid mechanical properties in laminar flows, MRI is also able to measure quantities, which can be attributed to turbulent processes [17–20]. These may be equally important in technical flows as well as in human haemodynamics, as they are typically associated with an impairment of the transport efficiency of the fluid. To this end, MRI-based quantification of the REYNOLDS stress tensor (RST) was performed under controlled conditions in a well-known fluid dynamic test case, the flow over periodic hills.

The precise quantification of fluid mechanical properties is of high scientific, technical as well as clinical interest, but still relies on experimental methods. MRI provides a versatile tool to determine a variety of these properties, but similarly has its own limitations. Overcoming those and further developing this tool is the driving force behind this work.

2 Theory

The following chapter covers the physical basics, which are necessary for the understanding of this thesis. This includes the basic principles of the phenomenon of nuclear magnetic resonance (NMR) and the magnetic resonance imaging based on it. Furthermore, the encoding of fluid mechanical parameters by means of magnetic resonance imaging are covered as well as basic concepts of fluid mechanics. A complete overview of the required theory would go beyond the scope of this work, which is why the focus in the following is on the most important basics necessary to understand this work.

2.1 Fourier transform

Since the FOURIER transform as a mathematical operation plays a central role in this work, its most important properties are summarized here. In general, the FOURIER transform \hat{f} of an integrable function $f : \mathbb{R} \rightarrow \mathbb{C}$ is defined as

$$\mathcal{F}(f(x)) = \hat{f}(\xi) = \int_{-\infty}^{\infty} f(x)e^{-i2\pi x\xi} dx, \quad (2.1)$$

while the inverse transform is given by

$$\mathcal{F}^{-1}(\hat{f}(\xi)) = f(x) = \int_{-\infty}^{\infty} \hat{f}(\xi)e^{i2\pi x\xi} d\xi, \quad (2.2)$$

such that

$$\mathcal{F}^{-1}(\mathcal{F}(f(x))) = f(x). \quad (2.3)$$

The most important properties of the FOURIER transform are:

Linearity:

$$\mathcal{F}(af(x) + bg(x)) = a\hat{f}(\xi) + b\hat{g}(\xi) \quad (2.4)$$

Shift theorem:

$$\mathcal{F}(f(x - x_0)) = \hat{f}(\xi)e^{-i2\pi x_0\xi} \quad (2.5)$$

Reality condition:

$$\hat{f}(-\xi) = \hat{f}(\xi) \quad \Leftrightarrow \quad f \text{ is real valued} \quad (2.6)$$

Convolution theorem:

$$(f * g)(x) = \hat{f}(\xi) \cdot \hat{g}(\xi) \quad (2.7)$$

2.2 Nuclear magnetic resonance

2.2.1 Nuclear spin and magnetic moment

Every atom is composed of electrons and a nucleus, which itself consists of one or more protons and a number of neutrons. Protons and neutrons both have an intrinsic quantised angular momentum, the nuclear spin, which can be derived from the inner components of the nucleons themselves. Just as nucleons inherit the nuclear spin from their constituents, atoms can also have a finite nuclear spin \vec{J} , depending on their composition from nucleons. In the following, only the ${}^1\text{H}$ atom will be considered, because it is the most common element in the human body, has a finite nuclear spin and is the only element that has been examined in the context of this thesis.

As a quantum mechanical angular momentum, the nuclear spin follows the angular momentum algebra and can be represented as state vector $|j, m\rangle$ with spin quantum number $j = \frac{1}{2}$ and magnetic spin quantum number $m \in [-\frac{1}{2}, +\frac{1}{2}]$. Furthermore, it satisfies the following eigenvalue equations and commutator relations:

$$\hat{J}^2 |j, m\rangle = \hbar^2 j(j+1) |j, m\rangle \quad (2.8)$$

$$\hat{J}_z |j, m\rangle = \hbar m |j, m\rangle \quad (2.9)$$

$$[\hat{J}_x, \hat{J}_y] = i\hbar \epsilon_{lmn} \hat{J}_z \quad (2.10)$$

$$[\hat{J}_z, \hat{J}^2] = 0. \quad (2.11)$$

Here, \hbar is the reduced PLANCK constant and ϵ_{lmn} the totally anti-symmetric tensor. It follows directly from the vanishing commutator in equation 2.11 that the magnitude and a single component of the angular momentum can be determined simultaneously. The finite nuclear spin of the ${}^1\text{H}$ atom gives rise to a nuclear magnetic moment $\vec{\mu}$ that is

linked to the nuclear spin via the proportionality constant $\gamma = 2\pi \cdot 42.576 \text{ MHz T}^{-1}$, the gyromagnetic ratio.

$$\vec{\mu} = \gamma \vec{J} \quad (2.12)$$

The nuclear magnetic moment $\vec{\mu}$ can interact with an external magnetic field \vec{B}_0 , which gives rise to the phenomenon of NMR. Without loss of generality, it can be assumed that the external magnetic field points in the z-direction ($\vec{B}_0 = (0, 0, B_z)^\top$), in which case the HAMILTON operator of the interaction can be written as

$$\hat{\mathcal{H}} = -\hat{\vec{\mu}} \cdot \vec{B}_0 = -\gamma \hat{J}_z B_z. \quad (2.13)$$

Since the eigenvalues of the angular momentum operator \hat{J}_z are given by equation 2.9, one can directly deduce the two discrete eigenvalues of the Hamilton operator:

$$E_{+\frac{1}{2}} = -\frac{1}{2} \gamma \hbar B_z \quad (2.14)$$

$$E_{-\frac{1}{2}} = +\frac{1}{2} \gamma \hbar B_z \quad (2.15)$$

This splitting of the energy eigenstates in an external magnetic field is called the ZEEMAN effect in analogy to the behavior of an electron in such a field. For the ^1H atom, these two energy states directly imply that there is only one single transition with the energy difference

$$\Delta E = \gamma \hbar B_z. \quad (2.16)$$

To induce this transition, a photon with suitable energy must either be absorbed or emitted. The resonance condition $\hbar\omega_L = \Delta E$, therefore, defines the so called LARMOR frequency ω_L :

$$\omega_L = \gamma B_z. \quad (2.17)$$

For a static magnetic field strength of 7 T, this results in $\omega_L = 298.03 \text{ MHz}$.

Having a half integer spin quantum number, the ^1H atom is a fermion and, therefore, follows the FERMI-DIRAC statistics with regard to the population of the two energy eigenstates in a system with thermodynamic equilibrium. In practice, experiments are conducted at room temperature or in vivo, which justifies a high temperature approximation. In this limit, the FERMI-DIRAC distribution approaches the BOLTZMANN distribution and

the occupation probability of a state with the energy E_m (c.f. equations 2.14 and 2.15) can be described as follows:

$$p(E_m) = \frac{e^{-E_m/k_b T}}{Z} \quad (2.18)$$

$$Z = \sum_m e^{-E_m/k_b T}. \quad (2.19)$$

Here, k_b is the BOLTZMANN constant, T the temperature of the probe and Z the partition function.

The elimination of the degeneracy of the eigenstates, and the thus different energy eigenvalues, lead to a different occupation of the two states. This deviation from uniform distribution can be characterized by the polarization η :

$$\eta = \frac{e^{\frac{\gamma \hbar B_z}{2k_b T}} - e^{-\frac{\gamma \hbar B_z}{2k_b T}}}{e^{\frac{\gamma \hbar B_z}{2k_b T}} + e^{-\frac{\gamma \hbar B_z}{2k_b T}}} = \tanh\left(\frac{\gamma \hbar B_z}{2k_b T}\right) \approx \frac{\gamma \hbar B_z}{2k_b T}. \quad (2.20)$$

Here, the high temperature approximation was assumed again in the last step, which is valid in this case for temperatures $T > 10^{-4}$ K. For values of $B_z = 7$ T and $T = 310$ K (normal body temperature) the polarization is $\eta \approx 23.07 \cdot 10^{-6}$.

This number underlines the sensitivity problem of NMR. Only the excess of the occupation number of the energetically more favorable eigenstate leads to a measurable signal. Equation 2.20, however, also directly implies that the polarization is linearly dependent on B_z , which motivates the efforts towards higher field strengths.

2.2.2 Macroscopic magnetization

So far, the properties of the nuclear spin and its interaction with an external static magnetic field have been described from a quantum mechanical point of view. In an NMR experiment, however, the measured signal originates from a macroscopic number of magnetic moments, which allows a classical description of the system. The resulting macroscopic magnetization is defined as follows:

$$\vec{M} = \frac{1}{V} \sum_{i=1}^N \langle \vec{\mu}_i \rangle \quad (2.21)$$

$$= \frac{1}{V} \sum_{i=1}^N \gamma \langle \vec{J}_i \rangle. \quad (2.22)$$

While the x- and y-components have a vanishing expectation value, $\langle J_z \rangle$ can be derived from equation 2.18 within the large temperature approximation:

$$\langle J_z \rangle = \frac{\gamma \hbar^2 B_z}{4k_b T}. \quad (2.23)$$

Therefore, the macroscopic magnetization in thermal equilibrium points in the z-direction and is given by

$$M_z = \frac{N \gamma^2 \hbar^2 B_z}{V 4k_b T}. \quad (2.24)$$

The averaging over a large number of nuclear spins leads to a macroscopic property, which can, therefore, be described with classical mechanics. The equation of motion of this non-interacting magnetization vector is described by:

$$\frac{\partial \vec{M}}{\partial t} = \vec{M} \times \gamma \vec{B}_0. \quad (2.25)$$

From this equation it immediately follows that the temporal derivative vanishes in the case of $\vec{M} \parallel \vec{B}_0$ and that a finite transverse magnetization precesses around \vec{B}_0 with the frequency of γB_z .

In reality, however, there are interactions between the individual spins as well as between the spins and the environment, which is why BLOCH introduced the phenomenological equations named after him in 1946 [21]. The following equations describe the motion of the magnetization under the influence of relaxation, which is characterized by the two time constants T_1 and T_2 :

$$\frac{dM_x(t)}{dt} = \gamma \left(\vec{M} \times \vec{B} \right)_x - \frac{M_x(t)}{T_2} \quad (2.26)$$

$$\frac{dM_y(t)}{dt} = \gamma \left(\vec{M} \times \vec{B} \right)_y - \frac{M_y(t)}{T_2} \quad (2.27)$$

$$\frac{dM_z(t)}{dt} = \gamma \left(\vec{M} \times \vec{B} \right)_z - \frac{M_z(t) - M_0}{T_1}. \quad (2.28)$$

Here, M_0 denotes the magnetization in thermal equilibrium ($M(t \rightarrow \infty)$). By introducing a transversal magnetization $M_\perp = M_x + iM_y$ and a longitudinal magnetization $M_\parallel = M_z$, the solution of the BLOCH equations, in absence of an RF pulse (i.e. $\vec{B} = (0, 0, B_z)^\top$), are exponential functions:

$$M_{\perp}(t) = M_{\perp}(0)e^{-i\omega_L t}e^{-t/T_2} \quad (2.29)$$

$$M_{\parallel}(t) = M_{\parallel}(0)e^{-t/T_1} + M_0(1 - e^{-t/T_1}). \quad (2.30)$$

This means that the transversal magnetization precesses around \vec{B}_0 with the LARMOR frequency ω_L , while its magnitude decays exponentially with the time constant T_2 . At the same time, the longitudinal component relaxes back to the equilibrium magnetization M_0 . The two time constants introduced by BLOCH indicate two different physical processes.

Longitudinal relaxation (T_1): The solution of the BLOCH equations implies that the longitudinal component of the magnetization vector relaxes towards thermal equilibrium. The thermal movement of the molecules causes fluctuations in the local magnetic field, which induce a transfer of energy between the spins and the environment. This leads to a return of the population numbers to the equilibrium state, which is given by the BOLTZMANN statistics. Since the nomenclature originated from solid state NMR, this process is often called spin-lattice relaxation.

Transversal relaxation (T_2): Due to the interaction between the spins, they experience local magnetic fields that vary in time, which in turn lead to different local precession frequencies. As a result, the phase coherence between the spins is lost without energy transfer. With this process, the system does not aim at minimizing the energy, but at maximizing the entropy. Due to the nature of this relaxation path, it is also called spin-spin relaxation.

In addition to the spin-spin interaction mentioned above, local magnetic field inhomogeneities cause an additional dephasing of the spins, resulting in an even faster signal decay, which is described by the time constant T_2^* , also called apparent T_2 relaxation.

2.2.3 Manipulation of the macroscopic magnetization

In order to generate an NMR signal from a sample, the magnetization must be deflected out of equilibrium. For this purpose, an additional, time-varying magnetic field $\vec{B}_1(t) \perp \vec{B}_0$ is applied. In this context, it is common to introduce a rotating reference frame $(x', y', z')^{\top}$, whose axis of rotation $\vec{\Omega}$ is parallel to \vec{B}_0 . The magnetization vector in this rotating reference frame is connected to the resting reference frame via:

$$\left. \frac{\partial \vec{M}}{\partial t} \right|_{rot} = \vec{M} \times (\gamma \vec{B}_0 + \vec{\Omega}) \quad (2.31)$$

$$= \vec{M} \times \gamma \vec{B}_{eff}. \quad (2.32)$$

Here, $\vec{B}_{eff} = \vec{B}_0 + \frac{\vec{\Omega}}{\gamma}$ describes an effective magnetic field that dictates the precession axis in the rotating reference frame. If the resonance condition $|\vec{\Omega}| = -\gamma|\vec{B}_0|$ is fulfilled, i.e. $\vec{B}_{eff} = 0$, the temporal derivative of \vec{M} vanishes, which means that \vec{M} is static in the rotating reference frame. This transformation significantly simplifies the description of the effect of the radiofrequency \vec{B}_1 field on the magnetization vector \vec{M} .

Supposed that the duration over which the \vec{B}_1 field is applied is short enough, relaxation effects can be neglected during that time interval. If the frequency of the RF field is chosen to match ω_L , the magnetization precesses around the axis defined by \vec{B}_1 in the rotating reference frame. Defining the amplitude of the \vec{B}_1 field as B_1 and the phase relative to the x' -axis as ϕ , the effect of the applied \vec{B}_1 field can be expressed by equation 2.25:

$$\left. \frac{\partial \vec{M}}{\partial t} \right|_{rot} = \vec{M} \times \gamma \begin{pmatrix} B_1(t) \sin \phi \\ B_1(t) \cos \phi \\ 0 \end{pmatrix}. \quad (2.33)$$

By transforming into the rotating reference frame, the RF oscillation is demodulated and the RF field is transformed into the time-dependent envelope $B_1(t)$. The angle of rotation by which the magnetization is rotated around \vec{B}_1 is the so-called flip angle α :

$$\alpha(\tau) = \gamma \int_0^{\tau} B_1(t) dt. \quad (2.34)$$

Within the rotating reference frame, equation 2.29 is simplified to a real valued exponential function, if the resonance condition is fulfilled. The decay of the signal is then given by $s(t) \propto e^{-t/T_2^*}$; the Free Induction Decay (FID), which represents the measurand of NMR.

2.3 Magnetic resonance imaging

Previously, the physical phenomenon of nuclear magnetic resonance was dealt with, which ultimately leads to the FID, which is a measurable quantity. However, in order to use this phenomenon for diagnostic imaging applications, it is necessary to localize the NMR

signal. The basic principle of this localization is the application of linear gradient fields $\vec{G}(t)$, which introduce a spatial dependence into equation 2.17:

$$\vec{G}(t) = \vec{\nabla} B_z(t) \quad (2.35)$$

$$\Rightarrow \omega_L(\vec{r}, t) = \gamma \left(B_z + \vec{r} \cdot \vec{G}(t) \right). \quad (2.36)$$

Through a superposition of gradient fields, the resonance frequency can be varied in any spatial direction. Since, as will be shown later in this chapter, magnetic resonance imaging can distinguish between three logical directions: the logical coordinate axes RO (readout), PE (phase encoding) and SS (slice/slab selection) are also used for description in addition to the physical axes x, y and z.

2.3.1 Spatial encoding

In the following, an object with non-interacting transversal magnetization in the rotating reference frame is considered, which appears static if precessing with $\omega_L = \gamma B_z$ in the laboratory frame. By applying a temporally constant linear gradient over the duration t , the precession frequency is altered linearly in space according to equation 2.36. After the gradient is switched off, the precession frequency is constant in space again, but the magnetization has accumulated a phase relative to the magnetization at $\vec{r} = 0$:

$$\phi(\vec{r}, t) = - \int_0^t \omega_L(\vec{r}, t') dt' \quad (2.37)$$

$$= -\gamma \int_0^t \vec{r} \cdot \vec{G}(t') dt'. \quad (2.38)$$

The acquired signal of the object, characterized by the spatial magnetization distribution $M_{\perp}(\vec{r})$, is equivalent to the integral over the complex transversal magnetization and, therefore, given by

$$s(t) = \int M_{\perp}(\vec{r}) e^{-i\phi(\vec{r}, t)} d\vec{r}. \quad (2.39)$$

If one introduces the spatial frequency \vec{k} (which spans the so called k-space) as

$$\vec{k}(t) = \frac{\gamma}{2\pi} \int_0^t \vec{G}(t') dt', \quad (2.40)$$

the signal can be rewritten as

$$s(\vec{k}) = \int M_{\perp}(\vec{r}) e^{-i2\pi\vec{k}\vec{r}} d\vec{r}. \quad (2.41)$$

From equation 2.41 it becomes apparent that the measured signal is the FOURIER transform of the spatial magnetization distribution $M_{\perp}(\vec{r})$. This again means that if $s(\vec{k})$ is known for all \vec{k} , $M_{\perp}(\vec{r})$ can be obtained by the inverse FOURIER transform:

$$M_{\perp}(\vec{r}) = \int s(\vec{k}) e^{i2\pi\vec{k}\vec{r}} d\vec{k}. \quad (2.42)$$

It is obvious that $s(\vec{k})$ cannot be determined for all \vec{k} , but only for a finite number of points. This discrete sampling can follow a variety of trajectories in k-space, but only CARTESIAN sampling, which derives its name from a trajectory on a CARTESIAN grid, is to be considered here. From the NYQUIST-SHANNON-theorem the following relationships can be obtained for the distance between sampling points in k-space and the field of view (FOV) as well as for the maximum \vec{k} and the spatial resolution:

$$\Delta\vec{k} = (FOV_x^{-1}, FOV_y^{-1}, FOV_z^{-1})^{\top} \quad (2.43)$$

$$2\vec{k}_{max} = (\Delta x^{-1}, \Delta y^{-1}, \Delta z^{-1})^{\top}. \quad (2.44)$$

In CARTESIAN sampling, one dimension is typically encoded frequency encoding (RO direction), while the others are encoded via phase encoding. Although the basic physical process is the same for both, the applications of the two encoding mechanisms are clearly different.

Frequency encoding: In clinical applications, frequency encoding is typically applied along one direction, as it enables the acquisition of a whole line instead of a single point in k-space. For this purpose, a gradient of constant amplitude over time is applied during the data sampling period, resulting in a linear evolution of k_{RO} over time. During the finite data sampling period, a number N of discrete sampling points are acquired, depending on the FOV and spatial resolution in RO direction. Since the gradient amplitude is constant during this process, the k-space is traversed with constant speed and each sampling point contains accumulated information from a segment of the k-space trajectory acquired during a time interval τ . This gives rise to the definition of a bandwidth Δf of

a single k-space point as

$$\Delta f = \frac{1}{\tau}. \quad (2.45)$$

Defining the total acquisition time as $T_{acq} = N\tau$, this can also be rewritten as a bandwidth per pixel BW :

$$BW = \frac{\Delta f}{N} = \frac{1}{T_{acq}}. \quad (2.46)$$

Phase encoding: In the phase encoding direction, a gradient is applied before the acquisition period and the k-space is sampled step-wise by linearly varying k_{PE} . In three dimensional acquisitions, phase encoding can be applied in two directions, spanning the three-dimensional k-space.

2.3.2 Parallel imaging

Up to now, the properties of the receive coil used to detect the NMR signal have not been taken into account. In fact, almost all receive coils used in clinical imaging today are phased array coils, consisting of multiple independent receive elements. Originally, this coil concept was introduced to improve the SNR [22] but it can also be used to speed up the imaging process, which is called parallel imaging.

Each of the receiving coils has a spatially varying receive sensitivity $\mathcal{S}(\vec{r})$, whereby equation 2.41 can be formulated for the i th receive coil as follows:

$$s_i(\vec{k}) = \int \mathcal{S}_i(\vec{r}) M_{\perp}(\vec{r}) e^{-i2\pi\vec{k}\vec{r}} d\vec{r}. \quad (2.47)$$

Since the receive sensitivities of a phased array already contain spatial information, the k-space does not have to be completely sampled during acquisition to reconstruct an artifact-free image. The missing data can be estimated from the acquired k-space data and additional knowledge about the receive sensitivities. There are several reconstruction techniques based on this concept that can be performed either in image space or in k-space. The most established methods are sensitivity encoding (SENSE) [23] and generalized autocalibrating partial parallel acquisition (GRAPPA) [24].

2.3.3 Excitation k-space

The previously introduced concept of k-space is a powerful tool to understand the spatial encoding process of the NRM signal from the perspective of sampling spatial frequencies. Until now, the necessary disturbance of the equilibrium state of the magnetization, which is essential for the measurement of the NMR signal, has not been considered in detail. The following section, therefore, deals with this topic and introduces the concept of the excitation k-space [25], which can be defined in analogy to the already defined acquisition k-space.

Neglecting relaxation effects during the excitation process, the BLOCH equation in the rotating reference frame can be expressed in matrix notation as

$$\begin{pmatrix} \frac{\partial M_x}{\partial t} \\ \frac{\partial M_y}{\partial t} \\ \frac{\partial M_z}{\partial t} \end{pmatrix} = \gamma \begin{pmatrix} 0 & \vec{G}(t) \cdot \vec{r} & -B_{1,y}(t) \\ -\vec{G}(t) \cdot \vec{r} & 0 & B_{1,x}(t) \\ B_{1,y}(t) & -B_{1,x}(t) & 0 \end{pmatrix} \begin{pmatrix} M_x \\ M_y \\ M_z \end{pmatrix}. \quad (2.48)$$

Here, $\vec{G}(t)$ is the applied linear gradient and $B_{1,x}(t)$ and $B_{1,y}(t)$ is the applied RF field along the x and y axes, respectively. Within the small-tip-angle approximation, the magnetization vector is assumed to be rotated by only a small flip angle, resulting in a constant longitudinal magnetization that is approximately equal to its equilibrium state,

$$M_z \approx M_0 = \text{const.} \quad (2.49)$$

Taking into account this assumption and the definition of the complex valued transverse magnetization as

$$M_{\perp} = M_x + iM_y, \quad (2.50)$$

as well as the complex valued RF field as

$$B_1 = B_{1,x} + iB_{1,y}, \quad (2.51)$$

the first two components of equation 2.48 can be decoupled from the third and be written as a single complex valued differential equation:

$$\frac{\partial M_{\perp}}{\partial t} = i\gamma \vec{G} \cdot \vec{r} M_{\perp} + i\gamma B_1 M_0 \quad (2.52)$$

If the magnetization was in the thermal equilibrium before the excitation, the boundary condition $\vec{M}(t=0) = (0, 0, M_0)^{\top}$ can be used to solve this differential equation at time T :

$$M_{\perp}(\vec{r}, T) = i\gamma M_0 \int_0^T B_1(t) e^{-i\gamma\vec{r} \cdot \int_t^T \vec{G}(t') dt'} dt \quad (2.53)$$

Analogous to the spatial frequency variable defined by equation 2.40, which spans the acquisition k-space, the excitation k-space can be introduced at this point by

$$\vec{k}(t) = -\frac{\gamma}{2\pi} \int_t^T \vec{G}(t') dt'. \quad (2.54)$$

It is important to note that, in contrast to the definition of the acquisition k-space (c.f. equation 2.40), the integration limits have changed here.

Substituting equation 2.54 into equation 2.53, the solution of the differential equation may be rewritten as

$$M_{\perp}(\vec{r}, T) = i\gamma M_0 \int_0^T B_1(t) e^{i2\pi\vec{r} \cdot \vec{k}(t)} dt. \quad (2.55)$$

In a last step, one can write the exponential factor as an integral of a three-dimensional delta function ${}^3\delta$ and interchange the order of integration, which leads to

$$M_{\perp}(\vec{r}, T) = i\gamma M_0 \int \left\{ \int_0^T B_1(t) {}^3\delta(\vec{k}(t) - \vec{k}) dt \right\} e^{i2\pi\vec{r} \cdot \vec{k}} d\vec{k}. \quad (2.56)$$

Here, the inner integral over time

$$\rho(\vec{k}, T) = \int_0^T B_1(t) {}^3\delta(\vec{k}(t) - \vec{k}) dt \quad (2.57)$$

can be interpreted as a three-dimensional path in excitation k-space weighted by the RF excitation field $B_1(t)$. Thus, the solution of the differential equation can finally be represented as follows:

$$M_{\perp}(\vec{r}, T) = i\gamma M_0 \int_{\vec{K}} \rho(\vec{k}, T) e^{i2\pi\vec{r} \cdot \vec{k}} d\vec{k}. \quad (2.58)$$

The formalism of the excitation k-space introduced above can be summarized in words: In the small-tip-angle approximation, the transverse magnetization resulting from an excitation is the FOURIER transform of the excitation k-space trajectory weighted by the RF excitation field $B_1(t)$. By choosing a suitable weighted excitation k-space trajectory

by applying gradient fields and an appropriate B_1 field, any desired spatial distribution of the transverse magnetization can be achieved.

From this point of view, conventional slice-selective excitation can be easily understood. In this case, the desired transverse magnetization distribution is a real valued rectangular function along the z -axis, whose FOURIER transform is given by a sinc-shaped function. Therefore, a trajectory along k_z with a sinc-shaped weighting must be applied in excitation k -space. Since the slice-select gradient played out during the RF pulse has a constant amplitude, the k -space is sampled linearly. At the same time, the RF field weights the trajectory accordingly by its sinc-shaped waveform. From the definition of the excitation k -space (see equation 2.54) it becomes clear why a refocusing gradient is needed after the slice-select gradient, since the origin in k -space is always reached when the residual gradient integrates to zero. By applying the refocusing gradient, this happens in the middle of the RF waveform and after the refocusing gradient. This means that the k -space is symmetrically weighted, which according to the reality theorem, corresponds to a real valued FOURIER transform, i.e. the excited slice is rephased.

Due to the finite duration of the RF pulse, the sinc-shaped function has to be truncated, resulting in deviations from the ideal rectangular slice profile. Instead of simply cutting off the ideal sinc-shaped function, which would lead to discontinuous first derivatives, the RF pulse is additionally apodized (typically by a HAMMING or HANNING window). Such RF pulses are characterized by the dimensionless bandwidth-time-product

$$BWT = \Delta f \cdot t. \quad (2.59)$$

Here, Δf is the bandwidth of the RF pulse and t its duration. For a given slice-select gradient amplitude G_{SS} , the full width at half maximum of the excited slice is given by

$$FWHM = \frac{2\pi BWT}{\gamma G_{SS} t}. \quad (2.60)$$

Keeping the full width at half maximum constant, but changing the bandwidth-time-product and G_{SS} , yields different slice profiles as shown in figure 2.1.

2.3.4 Shinnar-Le Roux algorithm

As shown in the previous subsection, the excited transverse magnetization distribution is the FOURIER transform of the weighted excitation k -space trajectory in the small-tip-angle approximation. For large flip angles (greater than 90°), however, this approximation

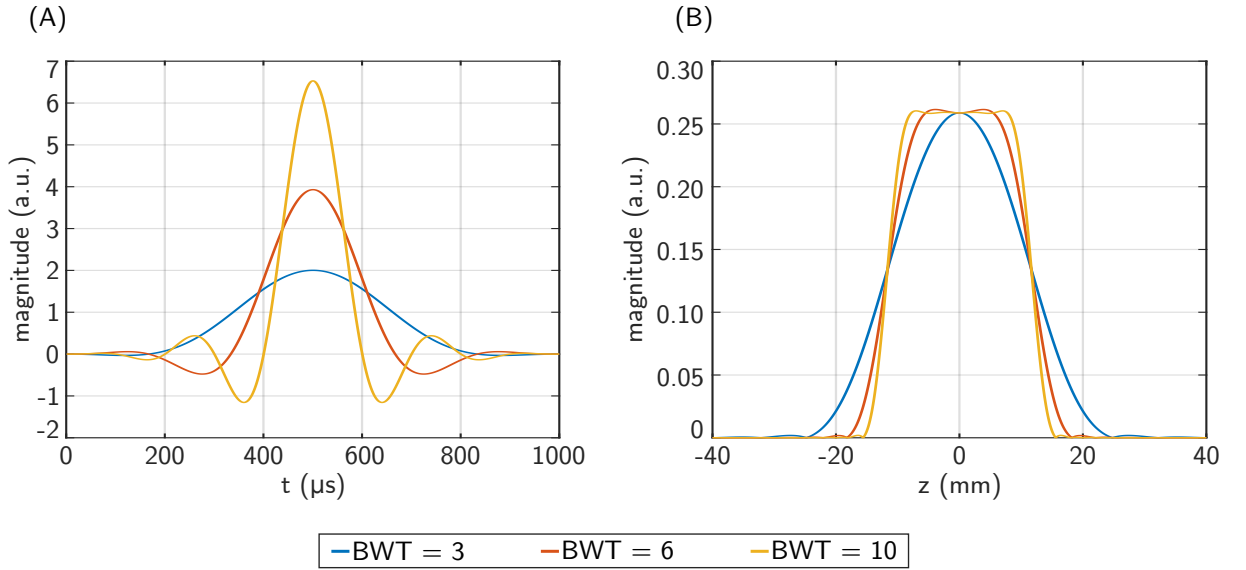


Figure 2.1: Hanning filtered sinc-shaped RF pulses (A) with a duration of 1 ms each, but different BWT . The RF pulses have been normalized to achieve the same flip angle as defined in equation 2.34. It should be noted that an increase in BWT leads to an increase in the required B_1 magnitude and the required amplitude of G_{SS} (not shown here). The different RF pulses lead to different slice profiles (B), having the same full width at half maximum, but different shapes. For a fixed slice thickness high BWT pulses lead to more rectangular slice profiles.

does not apply and the first two components of the differential equation 2.48 may not be decoupled from the third. In this case, the pulse design problem is nonlinear, but can still be directly solved by the SHINNAR-LE ROUX (SLR) algorithm for selective excitation [26–30].

The forward SLR transform maps an RF pulse waveform into two complex polynomial functions that characterize the resulting excitation slice profile. In contrast, the inverse SLR transform can be used to calculate the RF pulse that produces these polynomials.

In order to design a desired RF pulse, two polynomials have to be designed that correspond to the desired excitation slice profile. These polynomials can be computed using well-known digital filter design algorithms and finally be transformed into an RF pulse waveform via the inverse SLR transform.

2.4 Ultra high field MRI

The NMR signal is directly proportional to the strength of the static magnetic field, which has driven the technical development towards ever higher field strengths. Today,

field strengths of 1.5 T and 3 T have become standard in clinical routine and recently even 7 T has been approved for clinical use. Furthermore, experimental systems with 9.4 T, 10.5 T and 11.7 T have been realized and are used as investigational devices. From field strengths of 7 T on, one speaks of so-called UHF MRI.

On the one hand, the major advantage of going to higher fields is the positive impact on the SNR. On the other hand, UHF MRI also comes along with challenges, namely inhomogeneities of the static magnetic field and the RF field, which can significantly affect the image quality. While the former has been addressed through the use of higher order shimming coils, some techniques to compensate for the inhomogeneous radio frequency field follow.

2.4.1 Static magnetic field inhomogeneity

At UHF, imperfections of the static magnetic field B_0 occur to a greater extent. In addition, differences in susceptibility are proportional to B_0 . Therefore, differences between different tissue types, mainly between tissue and air, lead to macroscopic B_0 inhomogeneities [31]. The field inhomogeneity ΔB_0 causes a locally varying off-resonance of the magnetization, leading to a phase accumulation over time relative to an on-resonant reference. This phase is given by

$$\Delta\phi(\vec{r}, t) = - \int_0^t \gamma \Delta B_0(\vec{r}, t') dt' \quad (2.61)$$

$$= - \int_0^t \Delta\omega_L(\vec{r}, t') dt'. \quad (2.62)$$

2.4.2 Radio frequency field inhomogeneity

An increase of the static magnetic field \vec{B}_0 leads to an increase of the LARMOR frequency according to equation 2.17 and, thus, to a decrease of the wavelength of the RF field. At 7 T, the wavelength in empty space is approximately 100 cm, which is further reduced in biological tissue due to the high relative permittivity, resulting in wavelengths in the order of 10-15 cm. This is below the dimension of the human body, especially when looking at the abdomen and, therefore, leads to interference effects. Constructive interference typically leads to hyperintensities in the acquired images for most low flip angle gradient echo sequences, while destructive interference can completely suppress any signal in some parts of the region of interest (ROI). In order to mitigate these inhomogeneities, several

methods have been proposed, most including the need for multi-channel transmission arrays.

2.4.3 Parallel transmission

In a traditional MRI experiment a single transmit coil is used, which generates the B_1 field required to excite the magnetization. In analogy to parallel imaging, the concept of pTx was developed, in which several individual transmission elements are used simultaneously. Each of these elements has its own spatially varying transmission sensitivity $\mathcal{T}(\vec{r})$. By exploiting the spatial variation of these transmission sensitivities, spatially selective multidimensional RF pulses can be improved by for example shortening the pulse duration or reducing the required RF power. The consideration of these transmission sensitivities in the solution of the BLOCH equations in the small-tip-angle approximation (c.f. equation 2.55) leads to the following equation:

$$M_{\perp}(\vec{r}, T) = i\gamma M_0 \sum_{c=1}^{N_c} \mathcal{T}_c(\vec{r}) \int_0^T B_{1,c}(t) e^{i\gamma \Delta B_0(\vec{r})} e^{i2\pi \vec{r} \cdot \vec{k}(t)} dt. \quad (2.63)$$

Here, the index c counts through the N_c transmit channels and the additional phase factor $e^{i\gamma \Delta B_0(\vec{r})}$ accounts for off-resonance effects. By discretizing time and space, this equation can be represented in matrix notation, which is the basis of the spatial domain method for RF pulse design [32]:

$$M = A b. \quad (2.64)$$

In this representation, the vector b contains the RF waveforms (discretized in N_t time steps) for all N_c transmit channels. A is the system matrix that accounts for the excitation trajectory, transmission sensitivities and off-resonance effects. For a target transverse magnetization M_t , one can find the suitable vector b by solving an optimization problem by for example magnitude least squares optimization [32]:

$$\hat{b} = \underset{b}{\operatorname{argmin}} \left(\| |A b| - |M_t| \|_w^2 + \lambda \|b\|^2 \right). \quad (2.65)$$

Here, w is a diagonal matrix containing a spatial error weighting to exclude points outside the ROI and λ a regularization parameter that controls the the total RF energy $\|b\|^2$.

This general pulse design method allows for the design of arbitrary RF waveforms that excite any target transverse magnetization distribution. If the hardware allows, the RF pulses may differ not only in amplitude and phase, but a completely different waveform

can be applied to the individual transmit channels. However, the finite lifetime of the transverse magnetization and system imperfections pose limitations on the design of such RF pulses. Furthermore, certain applications do not require the full degree of freedom of this general approach, which can lead to a significant reduction in the complexity of the RF pulse design problem.

In the following, two special cases of RF pulse design are covered, namely B_1 shimming and multi-spoke RF pulses.

2.4.4 B_1 shimming

In B_1 shimming, the same RF waveform is applied to all transmit channels, but either phase φ_c or amplitude A_c or both are variable and are determined by the optimization described above in order to yield optimal spatial excitation homogeneity. If only the RF phase φ_c of each transmit channel is optimized, this is called B_1 phase shimming.

As a measure for spatial excitation homogeneity, the so-called coefficient of variation (CV) can be used

$$CV = \frac{std_w(|Ab|)}{mean_w(|Ab|)} \quad (2.66)$$

that is calculated within the target region defined by w .

2.4.5 Multi-spoke RF pulses

Many MRI experiments are conducted in a slice-selective fashion, whereby the excited magnetization along the z -direction is restricted to a certain slice (2D) or slab (3D). Because of the slice-selective excitation, the variation of the transmit sensitivities $\mathcal{T}_c(\vec{r})$ in the z -direction can be neglected, leading to 2D transmit sensitivities $\mathcal{T}_c(x, y)$. In this case, the desired transverse magnetization distribution can be split into two parts [12] and can be defined as

$$M_t(\vec{r}) = p(z)q(x, y) = \frac{p(z)}{\sum_{c=1}^{N_c} \mathcal{T}_c(x, y)}. \quad (2.67)$$

Here, $p(z)$ is defined as the slice profile along the z -direction and $q(x, y)$ as the inverse of the sum of the non-uniform transmit sensitivities $\mathcal{T}_c(x, y)$. Furthermore, it is assumed that $\sum_{c=1}^{N_c} \mathcal{T}_c(x, y) \neq 0$. As explained in subsection 2.3.3, any desired transverse magnetization distribution can be achieved by appropriately weighting a trajectory in the excitation k -space. The FOURIER transform $\mathcal{P}(k_z)$ of $p(z)$ is given by a sinc function, if the target

transverse magnetization distribution in z-direction is a rectangular function. Therefore, the excitation k-space has to be weighted accordingly along the k_z -direction.

At UHF, the inhomogeneity of the transmit sensitivity typically manifests itself as a smoothly varying function. Therefore, $q(x, y)$ can typically be approximated by the sum of a small number of cosine functions, the FOURIER transform $\mathcal{Q}(k_x, k_y)$ of which is a sum of DIRAC δ functions

$$\mathcal{Q}(k_x, k_y) = \sum_{j=1}^N A_j e^{i\phi_j} \delta(k_{x,j}, k_{y,j}). \quad (2.68)$$

As explained in subsection 2.3.3, the position in excitation k-space ($k_{x,j}$ and $k_{y,j}$) is defined by the applied gradients. Therefore, small gradients (so-called gradient blips) have to be applied between successive RF pulses to distribute the DIRAC δ functions in the k_x - k_y -plane. Furthermore, the number N of DIRAC δ functions can be decreased or increased, which is a balancing of the excitation duration against the excitation homogeneity.

The resulting DIRAC δ functions in the k_x - k_y -plane that are sinc-shaped along k_z are called multi-spoke RF pulses [12].

In summary, multi-spoke RF pulses consist of a train of slice-selective (sinc-shaped) RF pulses that are distributed in the k_x - k_y -plane (c.f. figure 2.2 and 2.3) via the application of small in-plane gradient blips. In the case of pTx, each spoke is applied with an individual B_1 shim setting.

In comparison to B_1 shimming, not only amplitude and phase of multiple RF pulses can be optimized for multi-spoke RF pulses, but also the position of these in the k_x - k_y -plane represents an additional degree of freedom. Therefore, multi-spoke RF pulses allow a further increase in flip angle homogeneity and are expected to gain additional importance at fields beyond 7 T.

In general, one can distinguish between so-called monopolar and bipolar excitation in the context of multi-spoke RF pulses. Here, these terms refer to the polarity of the slice-selection gradients of successive RF pulses. While monopolar excitation has proven insensitive to gradient delays [33, 34], bipolar excitation can significantly shorten the overall excitation time.

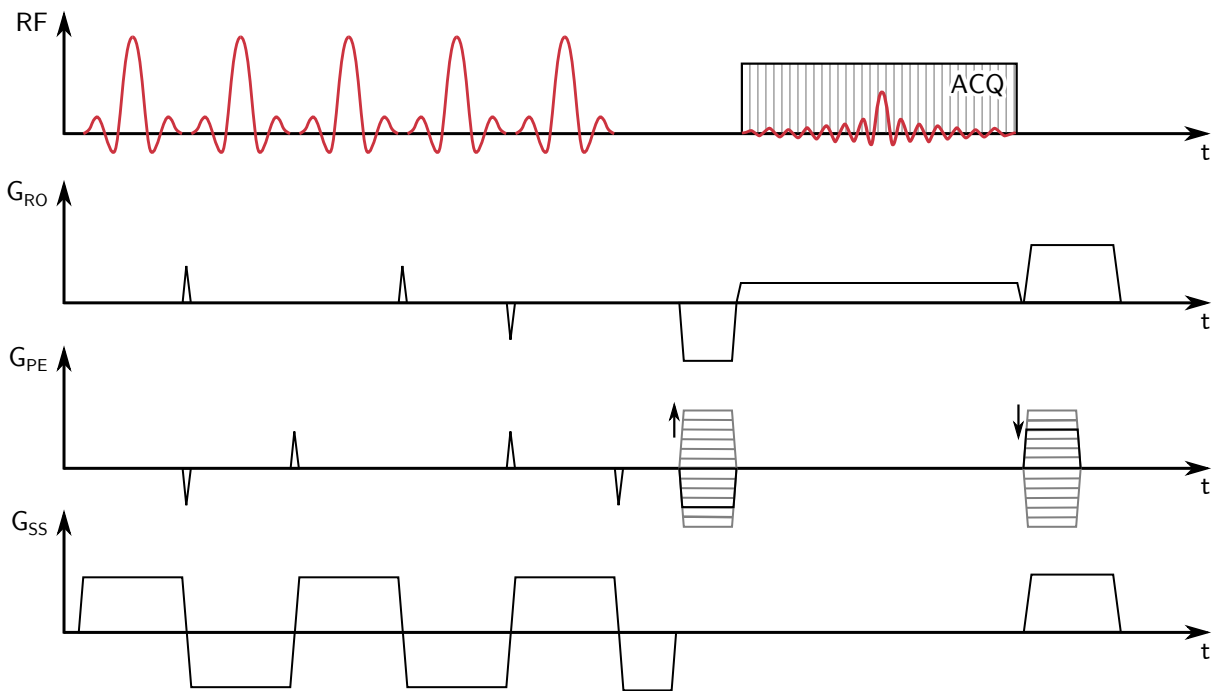


Figure 2.2: Example sequence diagram of a bipolar multi-spoke excitation. The five sinc-shaped RF pulses are played out consecutively, each creating a sinc-shaped weighting along k_z . By applying small gradient blips between the RF pulses, the different spokes are distributed in the k_x - k_y -plane.

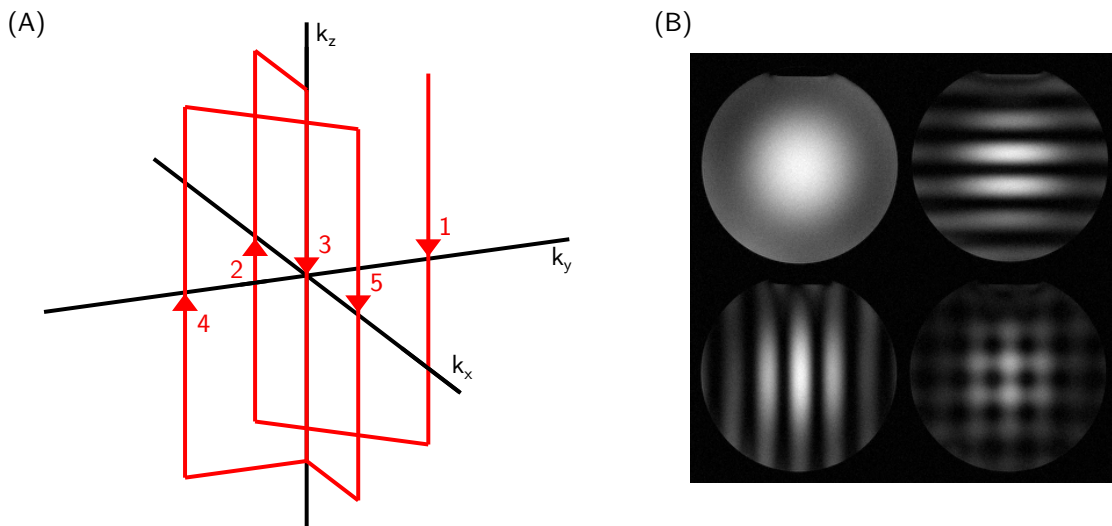


Figure 2.3: Excitation k -space trajectory (A) corresponding to the sequence diagram in figure 2.2. The excitation k -space is traversed according to the arrows and numbering. The effect of multi-spoke RF pulses can be seen in (B). Excitation patterns corresponding to different multi-spoke RF pulses are shown, i.e. spokes number 3, 1+3+4, 2+3+5, and all five RF pulses (left to right, top to bottom).

2.5 MRI of non-stationary magnetization

Previously, the general concept of MRI was explained for the special case of static magnetization. In particular, the concept of k-space was introduced, which allows the interpretation of data acquisition as a sampling of spatial frequencies. The central object of spatial encoding is the accumulation of phase due to linear gradient fields:

$$\phi(\vec{r}, t) = -\gamma \int_0^t \vec{r} \cdot \vec{G}(t') dt'. \quad (2.69)$$

Within the small-tip-angle approximation, the generation of the transverse magnetization is often reduced to a single point of instantaneous excitation. For symmetric sinc-shaped pulses, this point is located at the RF center and coincides with the isophase point t_{ISO} , at which all spins are phase-aligned during excitation [35]. Therefore, the temporal origin (lower integration limit in equation 2.69) is set to this point. If non-stationary magnetization is considered, the spatial coordinate \vec{r} becomes explicitly time dependent and can be expressed by a truncated TAYLOR expansion at the expansion point t_{exp} :

$$\vec{r}(t, t_{exp}) = \vec{r}_0 + \vec{v}_0(t - t_{exp}) + \frac{1}{2}\vec{a}_0(t - t_{exp})^2. \quad (2.70)$$

Here, \vec{r}_0 , \vec{v}_0 and \vec{a}_0 denote the position, velocity and acceleration of the magnetization at t_{exp} . Substituting equation 2.70 into equation 2.69 gives an expression for the accumulated phase of the non-stationary magnetization:

$$\phi(t, t_{exp}) = \phi_0 - \gamma \int_{t_{ISO}}^t \vec{r}(t', t_{exp}) \cdot \vec{G}(t') dt' \quad (2.71)$$

$$\begin{aligned} &= \phi_0 - \gamma \int_{t_{ISO}}^t \vec{r}_0 \cdot \vec{G}(t') dt' \\ &\quad - \gamma \int_{t_{ISO}}^t \vec{v}_0 \cdot \vec{G}(t') \cdot (t' - t_{exp}) dt' \\ &\quad - \gamma \int_{t_{ISO}}^t \frac{1}{2}\vec{a}_0 \cdot \vec{G}(t') \cdot (t' - t_{exp})^2 dt'. \end{aligned} \quad (2.72)$$

The additional phase term ϕ_0 accounts for a constant background phase that is present in an MRI experiment and can for example arise from off-resonance effects. Defining the

n th gradient moment as

$$\vec{m}_n(t, t_{exp}) = \int_{t_{ISO}}^t \vec{G}(t') \cdot (t' - t_{exp})^n dt' \quad (2.73)$$

yields

$$\phi(t, t_{exp}) = \phi_0 - \gamma \vec{r}_0 \cdot \vec{m}_0(t) - \gamma \vec{v}_0 \cdot \vec{m}_1(t, t_{exp}) - \gamma \frac{1}{2} \vec{a}_0 \cdot \vec{m}_2(t, t_{exp}). \quad (2.74)$$

This equation plays an important role in the following subsections, since it describes the accumulated phase of the non-stationary magnetization in terms of the gradient moments and the spatial coordinate as well as its temporal derivatives.

2.5.1 Gradient moments

The motion sensitivity of MRI can be conveniently expressed in terms of the gradient moments defined by equation 2.73. Therefore, some important properties of the gradient moments are discussed below.

While the zeroth gradient moment \vec{m}_0 is invariant with respect to temporal shifts of the expansion point, all higher gradient moments are explicitly time-dependent. The following equations express the relationship between gradient moments computed for two expansion time points $t_{exp,1}$ and $t_{exp,2}$:

$$\vec{m}_0(t, t_{exp,2}) = \vec{m}_0(t, t_{exp,1}) \quad (2.75)$$

$$\vec{m}_1(t, t_{exp,2}) = \vec{m}_1(t, t_{exp,1}) - \Delta t \cdot \vec{m}_0(t, t_{exp,1}) \quad (2.76)$$

$$\vec{m}_2(t, t_{exp,2}) = \vec{m}_2(t, t_{exp,1}) - 2\Delta t \cdot \vec{m}_1(t, t_{exp,1}) + \Delta t^2 \cdot \vec{m}_0(t, t_{exp,1}). \quad (2.77)$$

Here, Δt is the time difference ($t_{exp,2} - t_{exp,1}$) between the two expansion time points. In CARTESIAN imaging, ideal gradient waveforms would have rectangular shape, which would also significantly simplify the calculation of gradient moments. However, due to hardware limitations, namely the finite slew rate of the gradient system, this cannot be realized, and trapezoidal gradients are used instead. Nevertheless, mainly for reasons of symmetry, the gradient moments of these real gradient waveforms can be expressed in a compact way.

In the following, the gradient moments of such trapezoidal gradients will be examined more closely, since they are a central subject of this work. For simplicity, the vector notation is discarded here. Furthermore, the integration limit in equation 2.73 are assumed to be

$\pm\infty$. Therefore, the upper integration limit is omitted in the following expressions (e.g. $m_1(t, t_{exp}) = m_1(t_{exp})$).

A trapezoidal gradient can be described in terms of a ramp time t_r , a total duration T and an amplitude A (see figure 2.4).

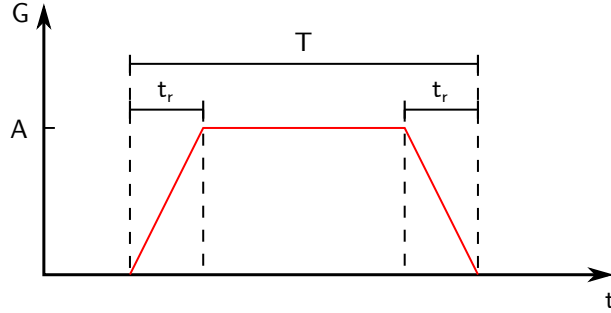


Figure 2.4: Trapezoidal gradient waveform (red) characterized by the ramp time t_r , the total duration T and the amplitude A .

The zeroth gradient moment, which is independent of the expansion time point t_{exp} of such a waveform, is given by

$$m_0 = A \cdot (T - t_r). \quad (2.78)$$

The first gradient moment can be easily obtained by placing the expansion time point in the center of the trapezoidal gradient. For reasons of symmetry, m_1 vanishes in this special case (integral over an asymmetric function with symmetrical integration limits). If any expansion point other than the center of the waveform is chosen, equation 2.76 can be used to obtain

$$m_1(t_{exp}) = \Delta t \cdot m_0 = \Delta t \cdot A \cdot (T - t_r), \quad (2.79)$$

in which Δt is the difference between t_{exp} and the center of the gradient waveform.

Similar considerations can be applied to the second gradient moment. In this case, m_2 does not vanish by choosing the center of the gradient waveform as the expansion time point, but computes to

$$m_2(t_{exp} = t_{center}) = \frac{1}{12} A \cdot (T - t_r) \cdot (2t_r^2 - 2t_r T + T^2). \quad (2.80)$$

For any other expansion time point, equation 2.77 leads to

$$m_2(t_{exp}) = \frac{1}{12} A \cdot (T - t_r) \cdot (2t_r^2 - 2t_r T + T^2) + \Delta t^2 \cdot m_0 \quad (2.81)$$

$$= \frac{1}{12} A \cdot (T - t_r) \cdot (2t_r^2 - 2t_r T + T^2 + 12\Delta t^2). \quad (2.82)$$

In order to control the zeroth and the first gradient moment simultaneously, bipolar gradients are used as shown in figure 2.5.

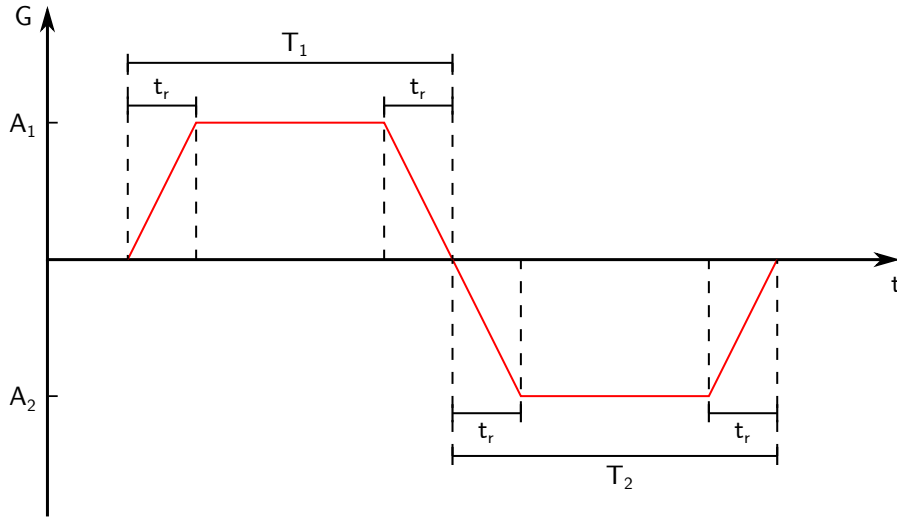


Figure 2.5: Bipolar gradient waveform (red) characterized by the ramp time t_r , the total durations T_1 and T_2 and the amplitudes A_1 and A_2 .

The gradient moments of such a waveform can be obtained from the sum of the gradient moments of the two trapezoidal gradients. This results in

$$m_0 = A_1 \cdot (T_1 - t_r) + A_2 \cdot (T_2 - t_r) \quad (2.83)$$

$$m_1(t_{exp}) = \Delta t_1 \cdot A_1 \cdot (T_1 - t_r) + \Delta t_2 \cdot A_2 \cdot (T_2 - t_r) \quad (2.84)$$

$$m_2(t_{exp}) = \frac{1}{12} A_1 \cdot (T_1 - t_r) \cdot (2t_r^2 - 2t_r T_1 + T_1^2 + 12\Delta t_1^2) \quad (2.85)$$

$$+ \frac{1}{12} A_2 \cdot (T_2 - t_r) \cdot (2t_r^2 - 2t_r T_2 + T_2^2 + 12\Delta t_2^2).$$

Here, Δt_1 and Δt_2 denote the difference between t_{exp} and the center of the first and second trapezoidal gradient, respectively. For the special case of $A_2 = -A_1$ and $T_2 = T_1$, these equations simplify to

$$m_0 = 0 \quad (2.86)$$

$$m_1 = -T_1 \cdot A_1 \cdot (T_1 - t_r) \quad (2.87)$$

$$m_2(t_{exp}) = A_1 \cdot (T_1 + t_r) \cdot (2\Delta t_1 \cdot T_1 - T_1^2). \quad (2.88)$$

Because this bipolar gradient has vanishing m_0 , the first gradient moment m_1 becomes independent of t_{exp} . For $\Delta t_1 = \frac{T_1}{2}$, which corresponds to placing the expansion time point in the center between the two trapezoidal gradients, m_2 vanishes. This can also be easily obtained for reasons of symmetry. In general, gradient moments are only independent of t_{exp} if all lower-order moments are zero.

2.5.2 Spatial encoding

As discussed earlier, the accumulated phase due to linear gradients is attributed to the acquisition k-space ($\vec{k}(t) = \frac{\gamma}{2\pi} \vec{m}_0(t)$), the space linked to spatial coordinates via the FOURIER transform. However, for non-stationary magnetization, the accumulated phase is given by equation 2.74 and any phase contributions originating from velocity or acceleration of the magnetization will be misinterpreted and linked to the spatial coordinate. This effect becomes apparent by rearranging equation 2.74 to

$$\phi(t, t_{exp}) = \phi_0 - \left(\vec{r}_0 + \vec{v}_0 \cdot \frac{\vec{m}_1(t, t_{exp})}{\vec{m}_0(t)} + \frac{1}{2} \vec{a}_0 \frac{\vec{m}_2(t, t_{exp})}{\vec{m}_0(t)} \right) \cdot \gamma \vec{m}_0(t). \quad (2.89)$$

Only if the expansion time point t_{exp} matches the time point t_0 , defined as the time point for which \vec{m}_1 and \vec{m}_2 vanish, the attribution of the phase to the acquisition k-space is correct and, therefore, the encoded spatial coordinate corresponds to $\vec{r}_0(t_0)$ [36, 37]. In other words, the spatial coordinate of the non-stationary magnetization is encoded at one instant in time, at which all higher order gradient moments vanish. This time point, denoted by t_0 , is referred to as the spatial encoding time point in this work.

Along the frequency encoding axis of a CARTESIAN imaging experiment, a gradient is active during the data acquisition. This leads to a linear variation of the zeroth gradient moment m_0^{RO} , corresponding to the acquisition of a single line in k-space. At the same time, however, m_1^{RO} and m_2^{RO} also vary during data acquisition and no t_0^{RO} exists that leads to a vanishing m_1^{RO} and m_2^{RO} for all k-space positions along the RO direction. However, it has been shown previously by WEDEEN et al. [38] that non-stationary magnetization will be imaged along the RO axis at its position at the center of the echo and will additionally be blurred. Therefore, the spatial encoding time point along the RO axis corresponds to

the center of the echo.

Along the PE axis, k-space is sampled stepwise and, therefore, m_1^{PE} and m_2^{PE} can be adjusted independently of m_0^{PE} for each k-space line. As a consequence, the encoding gradients can be designed to explicitly null m_1^{PE} and m_2^{PE} for a given t_0^{PE} . This means that along the PE axis the spatial encoding time point is an adjustable parameter, which can be chosen arbitrarily. If a conventional phase-encoding gradient is used that has fixed timings and only varies the gradient amplitude from k-space line to k-space line, t_0^{PE} corresponds to the temporal center of the phase-encoding gradient. In many clinical sequences that are not explicitly designed for flow applications, this encoding scheme is used due its time efficiency, leading to t_0^{PE} somewhere between the isophase point and the center of the echo. However, by using a bipolar phase-encoding gradient, m_1^{PE} can be explicitly nulled for an arbitrary t_0^{PE} . Since a bipolar gradient does not allow to additionally control m_2^{PE} , the resulting spatial encoding will still be biased by acceleration, which could be avoided by the use of tripolar phase-encoding gradients.

By designing the phase-encoding gradients such that t_0^{PE} coincides with the center of the echo, the spatial encoding time point along the PE axis can be synchronized with the RO axis, which is well-known to minimize misregistration artifacts [15, 16, 37, 39, 40]. If any other spatial encoding time point is chosen in the PE direction, the reconstructed position of the magnetization in RO and PE direction does not necessarily match. This may cause the non-stationary magnetization to be imaged at a wrong location and, in case of blood flow in a vessel, may lead to a signal of the moving magnetization outside the vessel lumen.

2.5.3 Velocity encoding

So far, only the time point for spatial encoding has been discussed, but for a velocity sensitive measurement, it is equivalently important, at which point in time the velocity is encoded. In order to encode the velocity information in the MR image, a finite first gradient moment \vec{m}_1 is applied. This generates a phase in the final image that is proportional to the velocity \vec{v} . However, there is also an unknown background phase ϕ_0 that can originate for example from off-resonance effects. Therefore, the velocity is obtained from the phase difference between two individual experiments that differ in their respective gradient moments. This is called a phase contrast (PC) measurement.

The resulting phase difference can be described following equation 2.74, but by replacing the gradient function $\vec{G}(t)$ by the gradient difference function $\Delta\vec{G}(t)$ between the two measurements:

$$\phi(t, t_{exp}) = -\gamma \vec{r}_0 \cdot \Delta \vec{m}_0(t) - \gamma \vec{v}_0 \cdot \Delta \vec{m}_1(t, t_{exp}) - \gamma \frac{1}{2} \vec{a}_0 \cdot \Delta \vec{m}_2(t, t_{exp}). \quad (2.90)$$

Here, $\Delta \vec{m}_0$ is typically set to zero, thus, $\Delta \vec{m}_1$ is independent of t_{exp} . $\Delta \vec{m}_2$, however, still depends on t_{exp} and, therefore, a time point $t_{exp} = t_1$ exists, at which $\Delta \vec{m}_2$ vanishes or is at least minimized. Since for this time point the complete phase difference is attributed to the velocity, the measured phase difference $\Delta \phi$ can be interpreted to correspond to the instantaneous velocity at t_1 [41]. Typically, the gradient difference function of a PC measurement is given by a bipolar gradient. In this case, t_1 corresponds to a point close to the center of gravity of this bipolar gradient difference function.

Depending on the timings of the gradients on the different axes, t_1 does not necessarily coincide for all three encoding axes, but the difference is typically on the order of a few hundred μ s.

The resulting phase difference $\Delta \phi$ yields the velocity of the magnetization, which can be calculated by

$$\vec{v} = \frac{\Delta \phi}{\gamma \Delta \vec{m}_1}. \quad (2.91)$$

The calculated velocity corresponds to the projection of the true velocity onto the axis defined by $\Delta \vec{m}_1$. In order to obtain all three components of the true velocity, at least four measurements have to be performed with $\Delta \vec{m}_1$ along three linearly independent directions. If these images themselves are three-dimensional and the velocity vector field is encoded in a time resolved manner, this technique is often termed 4D flow MRI.

There are different ways to encode the three velocity components in these four measurements that can be represented as encoding matrices E . In the case of the so-called single-sided encoding, this matrix is as follows:

$$E_{s.s.} = |\Delta \vec{m}_1| \cdot \begin{pmatrix} 0 & 0 & 0 \\ 1 & 0 & 0 \\ 0 & 1 & 0 \\ 0 & 0 & 1 \end{pmatrix}. \quad (2.92)$$

A compensated measurement is followed by three measurements encoding the velocity projection along a single axis of the three axes RO, PE and SS.

Another commonly used encoding scheme is the so-called two-sided or balanced encoding that corresponds to four points at the vertices of a cube. The corresponding encoding matrix is given by:

$$E_{t.s.} = \frac{|\Delta\vec{m}_1|}{2} \cdot \begin{pmatrix} -1 & -1 & -1 \\ +1 & -1 & -1 \\ -1 & +1 & -1 \\ -1 & -1 & +1 \end{pmatrix}. \quad (2.93)$$

Due to the 2π periodicity of the phase, there is a maximum velocity that can be encoded by a certain $\Delta\vec{m}_1$, before phase aliasing occurs. This value is referred to as the velocity encoding sensitivity and is given by

$$VENC = \frac{\pm\pi}{\gamma\Delta\vec{m}_1}. \quad (2.94)$$

Since velocities exceeding this value would result in aliasing, the approximate maximum velocity in an experiment must be known in advance in order to select a corresponding *VENC* value.

2.5.4 Acceleration encoding

For acceleration encoding, the same considerations apply as in the previous section on velocity encoding, except that tripolar, rather than bipolar, gradients are required to simultaneously control \vec{m}_0 , \vec{m}_1 and \vec{m}_2 . In this case, there exists an acceleration encoding time point t_2 for which the effect of gradient moments other than \vec{m}_2 vanish or are minimized. Therefore, the acceleration can be regarded as the instantaneous acceleration at this time point. The acceleration can be calculated from the measured phase difference via

$$\vec{a} = \frac{\Delta\phi}{\gamma\frac{1}{2}\Delta\vec{m}_2}. \quad (2.95)$$

In analogy to the velocity encoding sensitivity *VENC*, one can define the acceleration encoding sensitivity *AENC* as

$$AENC = \frac{\pm\pi}{\gamma\frac{1}{2}\Delta\vec{m}_2}. \quad (2.96)$$

2.5.5 Phase errors

The PC techniques described above assume that the phase difference between the individual images can be attributed solely to the variation of the gradient moments. However, it is well-known that phase offset errors are caused by distortions of the linear gradient

fields, which can be attributed to two main causes: eddy currents [42] and concomitant gradients [43] (MAXWELL terms).

According to FARADAY'S law, eddy currents are induced in conducting structures of the MR system by time-varying magnetic fields (i.e. the gradient fields). These currents themselves generate magnetic fields, which are superimposed on the actual gradient field and always oppose the change in the field causing them (LENZ'S law). Since the velocity-encoding gradients of the individual acquisitions of a PC measurement differ, the phases induced by eddy currents do not cancel out completely in the phase-difference image and need to be corrected in the post-processing.

Concomitant fields also arise from the applied gradient fields and are a direct consequence of the MAXWELL equations (hence the term MAXWELL terms):

$$\vec{\nabla} \cdot \vec{B} = 0 \quad (2.97)$$

$$\frac{1}{\mu_0} \vec{\nabla} \times \vec{B} = \varepsilon_0 \frac{\partial \vec{E}}{\partial t} + \vec{J}. \quad (2.98)$$

Here, \vec{E} is the electric field, \vec{J} the current density, and μ_0 and ε_0 are the permeability and permittivity of free space, respectively. If the displacement current density $\varepsilon_0 \frac{\partial \vec{E}}{\partial t}$ and the real current density \vec{J} are negligible, these equations can be expressed as four scalar equations:

$$\frac{\partial B_x}{\partial x} + \frac{\partial B_y}{\partial y} + \frac{\partial B_z}{\partial z} = 0 \quad (2.99)$$

$$\frac{\partial B_x}{\partial y} = \frac{\partial B_y}{\partial x} \quad (2.100)$$

$$\frac{\partial B_x}{\partial z} = \frac{\partial B_z}{\partial x} \quad (2.101)$$

$$\frac{\partial B_y}{\partial z} = \frac{\partial B_z}{\partial y}. \quad (2.102)$$

By defining the linear gradients $G_x = \frac{\partial B_z}{\partial x}$, $G_y = \frac{\partial B_z}{\partial y}$, $G_z = \frac{\partial B_z}{\partial z}$ and assuming a cylindrical gradient coil (for details see [43]), the concomitant field B_c can be expressed as

$$B_c = \frac{1}{2B_0} \left[\left(G_x z - \frac{G_z x}{2} \right)^2 + \left(G_y z - \frac{G_z y}{2} \right)^2 \right]. \quad (2.103)$$

In principle, the phase accumulated due to the concomitant fields can be calculated analytically and subtracted from the individual images of a phase contrast measurement,

however, it also can be removed within a single background phase removal step by fitting eddy currents and concomitant fields induced phase errors simultaneously.

2.5.6 Fourier velocity encoding

The previous subsections were based on the assumption that there is only one velocity or acceleration value in each voxel. In reality, however, there is a continuous distribution that has a finite width. Therefore, in the following, these distributions in the case of velocity encoding will be discussed.

By taking an intravoxel velocity distribution into account, the distribution of the transverse magnetization can be expanded to a six-dimensional function $M_{\perp}(\vec{r}, \vec{v})$ of space and velocity. Furthermore, in analogy to the k-space, a velocity frequency variable \vec{f} can be defined by

$$\vec{f}(t) = \frac{\gamma}{2\pi} \int_0^t t' \cdot \vec{G}(t') dt' = \frac{\gamma}{2\pi} \vec{m}_1(t) \quad (2.104)$$

that spans the f-space, which is defined as the dual space of velocities. With this definition, equation 2.41 can be written with a six-dimensional FOURIER transform

$$s(\vec{k}, \vec{f}) = \int M_{\perp}(\vec{r}, \vec{v}) e^{-i2\pi(\vec{k}\vec{r} + \vec{f}\vec{v})} d\vec{r} d\vec{v}. \quad (2.105)$$

Accordingly, the distribution of the transverse magnetization as a function of space and velocity can be obtained by the inverse FOURIER transform

$$M_{\perp}(\vec{r}, \vec{v}) = \int s(\vec{k}, \vec{f}) e^{-i2\pi(\vec{k}\vec{r} + \vec{f}\vec{v})} d\vec{k} d\vec{f}. \quad (2.106)$$

The acquisition k-space has thus been generalized to six dimensions, allowing both, the spatial and velocity, distribution of the transverse magnetization to be encoded. Since the velocity distribution is now also obtained by the FOURIER transform of the f-space, this method is termed FOURIER velocity encoding. Analogous to the FOV and the resolution in the spatial domain, these quantities can be defined in the velocity domain and follow the same relations:

$$\Delta\vec{f} = \left(FOV_{v_x}^{-1}, FOV_{v_y}^{-1}, FOV_{v_z}^{-1} \right)^{\top} \quad (2.107)$$

$$2\vec{f}_{max} = \left(\Delta v_x^{-1}, \Delta v_y^{-1}, \Delta v_z^{-1} \right)^{\top}. \quad (2.108)$$

In principle, the complete sampling of this six-dimensional space would allow the reconstruction of a three-dimensional image with a three-dimensional velocity distribution in each voxel. However, since the total measurement time required increases exponentially with the dimensions of the space to be sampled, this is typically not feasible. Under certain assumptions, however, the required measurement time can be drastically reduced, as will be shown below.

Although it was shown here only for velocity, it is in principle possible to apply FOURIER encoding to any higher temporal derivative of the spatial coordinate.

2.5.7 Quantification of the Reynolds stress tensor

In case of turbulent flow, the covariance of the fluctuating velocity components v' can be characterized by the REYNOLDS stress tensor (RST) τ . A detailed introduction of the RST can be found in subsection 2.6.4. In general, the velocity distribution $p(\vec{v})$ resulting from the velocity fluctuations can be arbitrarily shaped, but, in principle, can be resolved by FOURIER velocity encoding. In many cases, however, the velocity distribution can be assumed to be a GAUSSIAN distribution, which simplifies the encoding process and reduces the measurement time considerably. In this case the RST

$$\tau_{ij} = \rho \overline{v'_i v'_j} \quad (2.109)$$

represents the covariance matrix of a 3D GAUSSIAN distribution. The general expression of this distribution is

$$p(\vec{v}) = A \cdot \exp \left[-\frac{1}{2} (\vec{v} - \vec{\mu})^\top \Sigma^{-1} (\vec{v} - \vec{\mu}) \right]. \quad (2.110)$$

Here, A is a scaling factor, μ is the mean vector and Σ the (symmetric) covariance matrix of the GAUSSIAN distribution. Multiplying Σ by the fluid density ρ is equal to the RST τ . Since the FOURIER transform of a GAUSSIAN distribution is itself a GAUSSIAN distribution, the corresponding distribution in f-space can also be easily described. According to the FOURIER shift theorem (c.f. equation 2.5), a non-zero mean vector μ leads to a linear phase in f-space. The scaling factor A and the six entries of the symmetric REYNOLDS stress tensor τ can, therefore, be obtained from the magnitude of seven independent measurements [20], which differ in their respective first gradient moments and, thus, in their position in f-space.

Typically a 3D GAUSSIAN distribution is fitted to the magnitude data of seven velocity-encoded measurements in f-space. Via the inverse FOURIER transform, τ can then be

calculated. These seven measurements are acquired with the following encoding matrix E , according to the ICOSA6 [44] encoding scheme and an additional compensated measurement:

$$E = |\vec{m}_1| \cdot \begin{pmatrix} 0 & 0 & 0 \\ \frac{1}{\sqrt{1+\psi^2}} & 0 & \frac{\psi}{\sqrt{1+\psi^2}} \\ \frac{1}{\sqrt{1+\psi^2}} & 0 & \frac{-\psi}{\sqrt{1+\psi^2}} \\ \frac{\psi}{\sqrt{1+\psi^2}} & \frac{1}{\sqrt{1+\psi^2}} & 0 \\ \frac{-\psi}{\sqrt{1+\psi^2}} & \frac{1}{\sqrt{1+\psi^2}} & 0 \\ 0 & \frac{\psi}{\sqrt{1+\psi^2}} & \frac{1}{\sqrt{1+\psi^2}} \\ 0 & \frac{-\psi}{\sqrt{1+\psi^2}} & \frac{1}{\sqrt{1+\psi^2}} \end{pmatrix}. \quad (2.111)$$

Here, $\psi = \frac{1+\sqrt{5}}{2}$ is the golden ratio and $|\vec{m}_1|$ is the applied encoding moment. These measurements correspond to six points on a shell with radius $|\vec{m}_1|$ plus an additional compensated measurement.

With the definition of f-space (given by equation 2.104), the GAUSSIAN signal distribution $s(\vec{f})$ in f-space is linked to the RST via

$$\vec{f}^\top \tau \vec{f} = -2 \ln \left(\left| \frac{s(\vec{f})}{s(0)} \right| \right). \quad (2.112)$$

For N velocity encoded measurements, this can be rewritten in matrix notation as

$$\begin{pmatrix} f_{x,1}^2 & f_{y,1}^2 & f_{z,1}^2 & f_{x,1}f_{y,1} & f_{x,1}f_{z,1} & f_{y,1}f_{z,1} \\ f_{x,2}^2 & f_{y,2}^2 & f_{z,2}^2 & f_{x,2}f_{y,2} & f_{x,2}f_{z,2} & f_{y,2}f_{z,2} \\ \vdots & \vdots & \vdots & \vdots & \vdots & \vdots \\ f_{x,N}^2 & f_{y,N}^2 & f_{z,N}^2 & f_{x,N}f_{y,N} & f_{x,N}f_{z,N} & f_{y,N}f_{z,N} \end{pmatrix} \cdot \begin{pmatrix} \tau_{xx} \\ \tau_{yy} \\ \tau_{zz} \\ \tau_{xy} \\ \tau_{xz} \\ \tau_{yz} \end{pmatrix} = \begin{pmatrix} -2 \ln \left(\left| \frac{s(\vec{f}_1)}{s(0)} \right| \right) \\ -2 \ln \left(\left| \frac{s(\vec{f}_2)}{s(0)} \right| \right) \\ \vdots \\ -2 \ln \left(\left| \frac{s(\vec{f}_N)}{s(0)} \right| \right) \end{pmatrix}. \quad (2.113)$$

Here, each row represents a linear equation for one of the N measurements and this system of linear equations can be solved.

2.6 Fundamentals of fluid mechanics

In the following, the fluid mechanical fundamentals are considered, which are necessary to describe and understand the phenomena investigated in the context of this work. A more detailed overview can be found in the literature, such as the book by DURST [45].

Since the trajectory along which fluid elements move in a flow is only a function of time, any physical quantity (like velocity or heat) of this fluid element can also only be a function of time. Therefore, the time derivatives of these physical quantities are given by the so-called material derivative operator

$$\frac{D}{Dt} = \frac{\partial}{\partial t} + \frac{\partial}{\partial r_i} \cdot \frac{\partial r_i}{\partial t} = \frac{\partial}{\partial t} + \vec{v} \cdot \nabla. \quad (2.114)$$

2.6.1 Continuity equation

System boundaries can always be defined for a fluid dynamic system, such that the system can be regarded as closed in the sense that mass conservation is valid for the system:

$$\frac{dM}{dt} = \frac{d(\rho V)}{dt} = 0. \quad (2.115)$$

From this assumption, the continuity equation can be derived, which in the general case takes the following form:

$$\frac{\partial \rho}{\partial t} + \nabla \cdot (\rho \vec{v}) = 0. \quad (2.116)$$

In the special case of incompressible fluids (i.e. ρ is constant), it follows that

$$\nabla \cdot \vec{v} = 0. \quad (2.117)$$

2.6.2 Navier-Stokes equation

The application of NEWTON'S second law to a fluid element can be generally formulated as

$$\frac{d\vec{p}}{dt} = \sum \vec{F}_{surface} + \frac{d}{dt} (\vec{p}_{molecular}) + \sum \vec{F}_{external}. \quad (2.118)$$

Here, the left side represents the total temporal change in momentum \vec{p} . The right side contains pressure-induced surface forces, temporal changes in momentum due to molecular motion, and external forces such as gravitational or electromagnetic. Assuming that the external forces can be expressed as acceleration \vec{g} acting per unit mass and that

the pressure-induced surface forces result from the difference between the forces acting perpendicularly on the surface, the following momentum equation is obtained:

$$\rho \left(\frac{\partial v_j}{\partial t} + v_i \frac{\partial v_j}{\partial r_i} \right) = -\frac{\partial P}{\partial r_j} - \frac{\partial \tau_{ij}}{\partial r_i} + \rho g_j. \quad (2.119)$$

Here, P is the pressure and τ_{ij} a tensor that accounts for change in momentum due to molecular motion, which satisfies the condition $|\tau_{ij}| = |\tau_{ji}|$.

The three components of the velocity vector \vec{v} , the pressure P , and the six components of the symmetric τ tensor represent ten unknown variables. With only four equations (continuity equation and three momentum equations), this system cannot be solved and additional assumptions are needed. For NEWTONIAN fluids, these assumptions lead to

$$\tau_{ij} = -\mu \left(\frac{\partial v_j}{\partial r_i} + \frac{\partial v_i}{\partial r_j} \right), \quad (2.120)$$

in which μ is the dynamic viscosity of the fluid.

For $\rho = \text{const.}$ and $\mu = \text{const.}$, this leads to the NAVIER-STOKES equation

$$\rho \left[\frac{\partial v_j}{\partial t} + v_i \frac{\partial v_j}{\partial r_i} \right] = -\frac{\partial P}{\partial r_j} + \mu \frac{\partial^2 v_j}{\partial r_i^2} + \rho g_j. \quad (2.121)$$

This system of partial differential equations can be solved, if suitable initial and boundary conditions are given.

2.6.3 Wall shear stress

When considering flow within a vessel lumen, the velocity of the fluid is zero at the vessel wall (no-slip condition), but has a finite value at some height from the boundary. Therefore, the fluid exerts a tangential force on the wall. This force per unit surface area is the so-called wall shear stress. For NEWTONIAN fluids, the shear stress is the strain rate multiplied by the viscosity. Therefore, in its full expansion, the WSS $\vec{\chi}$ at a certain point on the vessel lumen is given by

$$\vec{\chi} = 2\mu \cdot \begin{pmatrix} \frac{\partial v_x}{\partial x} & \frac{1}{2} \left(\frac{\partial v_y}{\partial x} + \frac{\partial v_x}{\partial y} \right) & \frac{1}{2} \left(\frac{\partial v_z}{\partial x} + \frac{\partial v_x}{\partial z} \right) \\ \frac{1}{2} \left(\frac{\partial v_x}{\partial y} + \frac{\partial v_y}{\partial x} \right) & \frac{\partial v_y}{\partial y} & \frac{1}{2} \left(\frac{\partial v_z}{\partial y} + \frac{\partial v_y}{\partial z} \right) \\ \frac{1}{2} \left(\frac{\partial v_x}{\partial z} + \frac{\partial v_z}{\partial x} \right) & \frac{1}{2} \left(\frac{\partial v_y}{\partial z} + \frac{\partial v_z}{\partial y} \right) & \frac{\partial v_z}{\partial z} \end{pmatrix} \cdot \vec{n}, \quad (2.122)$$

in which \vec{n} is the inward normal vector with respect to the surface of the pipe.

2.6.4 Turbulent flow

The REYNOLDS number is a dimensionless quantity in fluid dynamics that can be used to characterize flow and is defined as

$$Re = \frac{v_c l_c}{\nu} = \frac{\rho v_c l_c}{\mu}. \quad (2.123)$$

Here, v_c is a characteristic velocity, l_c a characteristic length, and $\nu = \frac{\mu}{\rho}$ the kinematic viscosity of the fluid. Considerations about the meaning of the REYNOLDS number can be expressed via the times typical for diffusion and convection processes

$$Re = \frac{v_c l_c}{\nu} = \frac{(l_c^2/\nu)}{(l_c/v_c)} = \frac{\text{diffusion time}}{\text{convection time}} \quad (2.124)$$

or via the typical velocity of these different processes

$$Re = \frac{v_c l_c}{\nu} = \frac{v_c}{(\nu/l_c)} = \frac{\text{convection velocity}}{\text{diffusion velocity}}. \quad (2.125)$$

As long as the flow has and maintains its own high degree of order, it is laminar, i.e. the viscosity of the fluid in stable laminar flows is able to sufficiently dampen fluctuations of the flow variables that disturb the order of the flow. This damping of disturbances usually occurs at low REYNOLDS numbers.

In the case of high REYNOLDS numbers, the flow loses its regularity, i.e. stochastic fluctuations of the flow properties are observed, which superimpose the mean flow properties. The instantaneous velocity vector field (denoted by \hat{v}) of turbulent flow can, therefore, be split into a mean $\overline{v_i}$ and fluctuating part v'_i . This is called REYNOLDS decomposition and leads to

$$\hat{v}_i = \overline{v_i} + v'_i. \quad (2.126)$$

Here, the temporal mean is defined as

$$\overline{v_i} = \lim_{T \rightarrow \infty} \frac{1}{T} \int_0^T \hat{v}_i dt. \quad (2.127)$$

By definition, the time average of the fluctuating part disappears ($\overline{v'_i} = 0$), but in general higher order (n th order) moments can also be defined by

$$\overline{(v'_i)^n} = \lim_{T \rightarrow \infty} \frac{1}{T} \int_0^T (v'_i)^n dt, \quad (2.128)$$

which can have values other than zero.

By applying the REYNOLDS decomposition to the continuity equation (c.f. equation 2.117), the following relations for incompressible fluids can be derived:

$$\frac{\partial \bar{v}_i}{\partial r_i} = 0 \quad (2.129)$$

$$\frac{\partial v'_i}{\partial r_i} = 0. \quad (2.130)$$

Furthermore, the NAVIER-STOKES equation derived above (c.f. equation 2.121) can now be applied to turbulent flow, whereby the instantaneous quantities are represented in the terms of the REYNOLDS decomposition ($\hat{v}_i = \bar{v}_i + v'_i$, $\hat{\rho} = \bar{\rho} + \rho'$ and $\hat{P} = \bar{P} + P'$). For incompressible fluids ($\hat{\rho} = \bar{\rho}$), the so-called REYNOLDS averaged NAVIER-STOKES equation is obtained:

$$\bar{\rho} \left[\frac{\partial \bar{v}_j}{\partial t} + \bar{v}_i \frac{\partial \bar{v}_j}{\partial r_i} \right] = - \frac{\partial \bar{P}}{\partial r_j} + \frac{\partial}{\partial r_i} \left[\mu \frac{\partial \bar{v}_j}{\partial r_i} - \overline{\rho v'_i v'_j} \right] + \bar{\rho} g_j. \quad (2.131)$$

Equation 2.131 shows that by applying REYNOLDS averaging to the NAVIER-STOKES equation, additional terms are introduced that can be interpreted as

$$(\tau_{ij})_{total} = -\mu \frac{\partial \bar{v}_j}{\partial r_i} + \overline{\rho v'_i v'_j} = (\tau_{ij})_{lam} + (\tau_{ij})_{turb}. \quad (2.132)$$

These additional terms represent a tensor quantity that is typically referred to as the REYNOLDS stress tensor

$$\overline{\rho v'_i v'_j} = \bar{\rho} \begin{pmatrix} \overline{v'_1{}^2} & \overline{v'_1 v'_2} & \overline{v'_1 v'_3} \\ \overline{v'_2 v'_1} & \overline{v'_2{}^2} & \overline{v'_2 v'_3} \\ \overline{v'_3 v'_1} & \overline{v'_3 v'_2} & \overline{v'_3{}^2} \end{pmatrix}, \quad (2.133)$$

which is a symmetric tensor, i.e. $|\overline{v'_i v'_j}| = |\overline{v'_j v'_i}|$, and represents the covariance matrix of the velocity fluctuations.

The diagonal terms appearing in the RST can be interpreted as normal stresses, whereas the non-diagonal terms represent shear stresses. Furthermore, the turbulent kinetic energy (TKE), the mean kinetic energy per unit mass associated with turbulent flow, equals the trace of the RST:

$$TKE = \frac{1}{2} \sum_{i=1}^3 \overline{v'_i{}^2}. \quad (2.134)$$

3 Methods

3.1 Hardware

3.1.1 MR systems

The measurements performed within this work were performed on three different MR systems manufactured by Siemens (Siemens, Erlangen, Germany). Two systems with a static magnetic field strength of 3 T (MAGNETOM Trio and MAGNETOM Verio) and a 7 T whole body system (MAGNETOM 7T) were used. While the MAGNETOM Verio was equipped with an AS097 gradient coil, the MAGNETOM Trio and MAGNETOM 7T were equipped with an AS095DS gradient coil.

The MAGNETOM Trio was used for the phantom study of turbulent flow and the rotation phantom was scanned in the MAGNETOM Verio. All other experiments were conducted at 7 T.

3.1.2 RF coils

The study of turbulent flow used two matrix body coils (see figure 3.1) from the manufacturer Siemens that were strapped around the flow channel. These coils are receive-only coils with six receive channels in each matrix body coil. The dedicated transmit coil of the 3 T system was used for excitation.



Figure 3.1: Matrix body coil as used at the 3 T Trio system. The shown matrix body coil consists of six individual receive coils.

When investigating the rotation phantom, a head coil from Siemens (see figure 3.2) with twelve dedicated receive channels was used in combination with the transmit coil integrated into the 3 T system. This coil was primarily chosen for the fact that its use allowed

optical access to the rotation phantom, which was necessary for a laser-based feedback system to work properly.



Figure 3.2: Head coil with twelve dedicated receive channels. This coil was exclusively used in combination with the rotation phantom.

At 7 T two different RF coils were used that were both used for RF transmission as well as RF reception. The first coil was a dedicated knee coil from Quality Electrodynamics (Mayfield Village, OH, USA) that had a birdcage design for the transmit part and additional 28 dedicated receive coils (see figure 3.3). This coil was used for all phantom studies performed at the 7 T system, since it allows the flow phantoms to be completely inserted into the coil. When targeting the femoral artery in the in vivo experiments, the same knee coil was used. Furthermore, the in vivo experiments targeting the human aorta were performed with an in-house-built 8-channel transceiver coil [46, 47] as shown in figure 3.4.



Figure 3.3: Knee coil from the 7 T system with an integrated birdcage coil for transmission and 28 dedicated receive elements.



Figure 3.4: 8-channel transceiver body coil from the 7 T system.

3.1.3 Flow Pump

All phantom experiments at the 7 T system were performed by using a programmable physiological flow pump (CardioFlow 5000 MR, Shelly Medical Imaging, London, Ontario, Canada). As shown in figure 3.5, the pump system consisted of a control unit and a separate pump unit, which housed a gear pump. The programmable pump was used to generate a constant as well as pulsatile flow with a peak volume flow of up to 140 mL/s. For safety reasons, the flow pump was positioned outside of the RF cabin of the 7 T system. Therefore, relatively long tubing (16 m) was necessary to connect the flow pump to the flow phantoms.



Figure 3.5: CardioFlow 5000 MR programmable physiological flow pump.

For the measurement of flow over periodic hills, a custom pump system capable of a flow rate of 300 L/min and with a tank capacity of 1000 L was used. In this case, the water

was mixed with 1 g/L copper(II) sulfate as contrast agent. For supervision of the flow rate, an ultrasonic flow meter (deltawaveC-F, systec controls, Puchheim, Germany) with a sensor tolerance of 1.5% was utilized. In addition, the temperature was controlled with a Pt100 sensor.

3.1.4 Phantoms

Since a wide variety of flow conditions were investigated in this work, a number of different flow phantoms were used, which can be classified into three categories. In the following, these are described and photos as well as MR images of the phantoms are shown.

The first category is a rotation phantom consisting of a cylindrical body with a diameter of 128 mm, filled with a tissue-simulating liquid (water, polyvinylpyrrolidone (PVP), sodium chloride) and surrounded by an additional container as displayed in figure 3.6. The top of the inner cylinder was designed as an impeller with twelve blades. Compressed air was pressed against the impeller via a nozzle in the outer container to set the inner cylinder in rotation. The rotational frequency was controlled by the air flow and monitored externally by a laser-based counter.

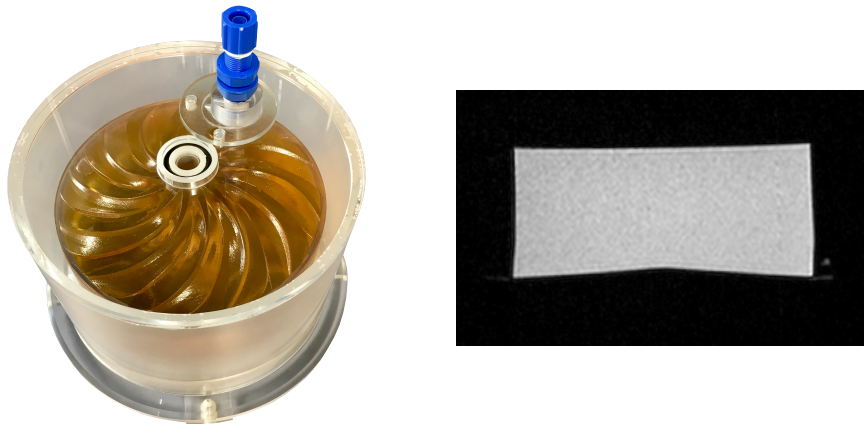


Figure 3.6: Rotation phantom.

The second category consists of three flow phantoms (see figure 3.7-3.9), all of which contain artificial vessels (3D printed or made of acrylic glass) embedded in agarose gel of 0.9% saline solution.

The first flow phantom, shown in figure 3.7, consists of four straight pipes of acrylic glass with diameters of 4, 8, 12 and 16 mm embedded in a cylindrical body with a total length of 450 mm and a radius of 130 mm. In this study, only the two large pipes were used,

which are connected at the back of the phantom.



Figure 3.7: Flow phantom with four straight pipes of acrylic glass with different diameters.

The second flow phantom (see figure 3.8) is 3D printed and mimics a stenosis with a diameter reduction from 15 mm to 5 mm. The stenosis follows no strict geometry, but was designed to allow a smooth transition from the full to the reduced diameter. This phantom allows measurements of constant, but accelerated flow in a simple geometry.



Figure 3.8: Straight 3D printed stenosis phantom.

The third flow phantom is a simplified 3D printed model of a stenotic aorta. The stenosis geometry is modeled as a VENTURI nozzle, the dimensions of which are shown in figure 3.9. This phantom was used exclusively for the evaluation of the WSS, as it generates a high-velocity jet that collides with the outer vessel wall.

The third category consists of a flow channel with a square cross-section with 74 mm edge length and an additional insert consisting of 13 identical periodic hills (figure 3.10). Measurements were performed between the 10th and 11th hill to assure that the steady-state was reached. The distance between consecutive hills was 219.4 mm and each hill had a height of 24.4 mm.

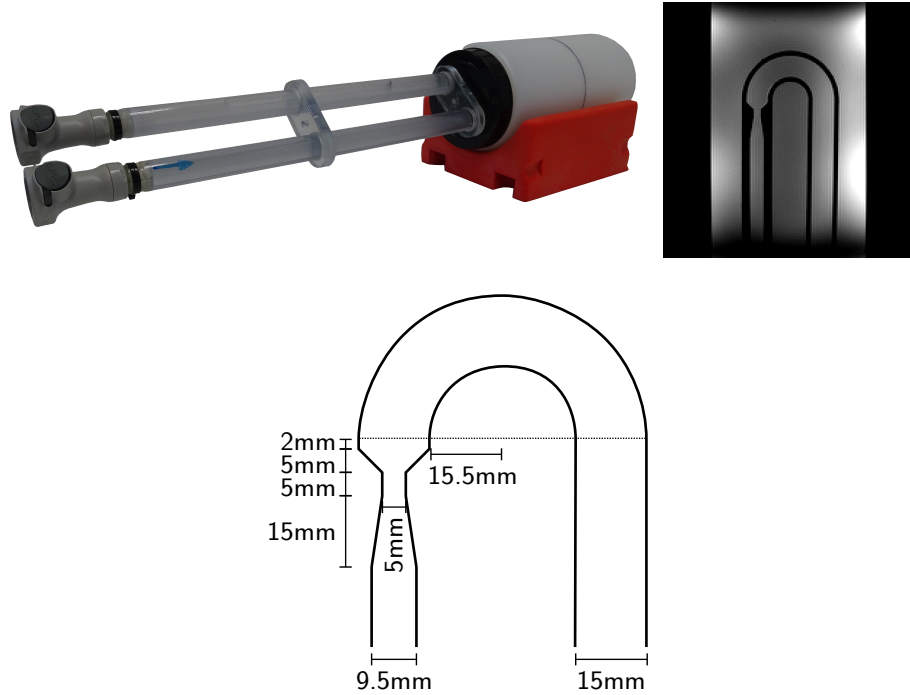


Figure 3.9: Simplified 3D printed model of a stenotic aorta with a stenosis modeled as a VENTURI nozzle.



Figure 3.10: Phantom to generate flow over periodic hills.

3.2 Pulse sequences

This section describes the modifications made to various pulse sequences. These were each programmed in Siemens' integrated development environment for applications (IDEA). Thus, the pulse sequences can be used directly on the MR machines without any further aids.

3.2.1 Velocity mapping

For velocity quantification, a PC sequence, as described by MARKL et al. [8] with two-sided velocity encoding (see subsection 2.5.3), was modified.

First, three different encoding schemes were implemented that differ in their respective spatial encoding time points in PE direction and, therefore, in their respective displacement artifacts. If a 3D image is acquired, the same considerations hold true for the SS direction. Higher orders of motion (e.g. acceleration) were neglected in the design of these encoding schemes. These artifacts can be characterized by a spatial displacement $\Delta\vec{r}$, which leads to non-stationary magnetization to be visualized rather at $\vec{r}_0 = \vec{r}_0^{ISO} + \Delta\vec{r}$ than at its position of excitation \vec{r}_0^{ISO} in the reconstructed image. In the following, the isophase point of the RF pulse is assumed to be the temporal origin. An the integral in equation 2.69 is evaluated at the center of the echo.

Encoding scheme FAST

For the first encoding scheme, the encoding gradients were calculated according to the method given by BERNSTEIN et al. [48], which leads to a minimum duration of the encoding gradients and is termed encoding scheme FAST here. Since this encoding scheme does not explicitly control the spatial encoding time point in PE direction, t_0^{PE} lies somewhere between the end of the RF pulse and the beginning of the data acquisition and the exact time point depends on the sequence parameters. In general, scheme FAST leads to a spatial shift $\Delta\vec{r}$ in the image domain relative to a static reference that is given by

$$\Delta\vec{r} = \begin{pmatrix} \Delta r_{RO} \\ \Delta r_{PE} \\ \Delta r_{SS} \end{pmatrix} = \begin{pmatrix} v_{RO} \cdot TE \\ v_{PE} \cdot t_0^{PE} \\ v_{SS} \cdot t_0^{SS} \end{pmatrix}. \quad (3.1)$$

Here, the echo time TE was defined as the time period between the isophase point and the center of the echo. As can be seen from equation 3.1, the spatial shift is oblique with respect to the velocity vector for encoding scheme FAST, which leads to the well-known displacement artifact.

Encoding scheme ECHO

The second encoding scheme, termed scheme ECHO here, explicitly synchronizes the spatial encoding time point of the PE axis with the spatial encoding time point of the RO axis (center of the echo) and thereby aims to minimize displacement artifacts [15, 16, 37, 39, 40]. The resulting spatial shift of this encoding scheme is along the velocity vector and, therefore, independent of the orientation of the imaging axes with respect to the velocity vector field. For scheme ECHO the spatial shift is given by

$$\Delta\vec{r} = \begin{pmatrix} \Delta r_{RO} \\ \Delta r_{PE} \\ \Delta r_{SS} \end{pmatrix} = \begin{pmatrix} v_{RO} \cdot TE \\ v_{PE} \cdot TE \\ v_{SS} \cdot TE \end{pmatrix} = \vec{v} \cdot TE. \quad (3.2)$$

Encoding scheme ISO

Additionally, a third encoding scheme was investigated that synchronizes the spatial encoding time point of the PE axis with the isophase point of the RF pulse. This scheme was termed scheme ISO and leads to the following spatial shift:

$$\Delta\vec{r} = \begin{pmatrix} \Delta r_{RO} \\ \Delta r_{PE} \\ \Delta r_{SS} \end{pmatrix} = \begin{pmatrix} v_{RO} \cdot TE \\ 0 \\ 0 \end{pmatrix} \quad (3.3)$$

In general, scheme ISO can lead to displacement artifacts, but for the special case of a vanishing velocity component in the RO direction (i.e. $v_{RO} = 0$), scheme ISO produces images free of velocity-related shifts.

The encoding gradients of scheme ECHO and ISO were calculated according to the following general design principle, which was developed within the scope of this thesis. In order to simultaneously control the zeroth and first gradient moment for all k-space lines, bipolar gradients must be used. Assuming two adjacent trapezoidal gradient lobes, a linear system of equations can be formulated for the zeroth and first gradient moment generated by these gradients (see subsection 2.5.1 and figure 2.5):

$$\begin{aligned} m_0 &= A_1 (T_1 - t_r) + A_2 (T_2 - t_r) \\ m_1 &= A_1 (T_1 - t_r) \left(T_0 + \frac{T_1}{2} \right) + A_2 (T_2 - t_r) \left(T_0 + T_1 + \frac{T_2}{2} \right). \end{aligned} \quad (3.4)$$

Here, T_0 denotes the onset of the first gradient lobe with respect to the isophase point of the excitation RF pulse. For given timings this system of linear equations can be solved for the amplitudes of the two gradient lobes:

$$\begin{aligned} A_1 &= -\frac{2m_1 - (2T_0 + 2T_1 + T_2) m_0}{(T_1 - t_r) (T_1 + T_2)} \\ A_2 &= +\frac{2m_1 - (2T_0 + T_1) m_0}{(T_2 - t_r) (T_1 + T_2)}. \end{aligned} \quad (3.5)$$

Equation 3.5 can in principle be solved for any given timings, however, the gradients have to fulfill the system limitations, i.e. the maximum gradient amplitude \hat{A} and the maximum gradient slew rate \hat{s} . First, a fixed ramp time $t_r = \hat{A}/\hat{s}$ is assumed, ensuring that the calculated gradients are within these limits. Furthermore, it can be seen from equation 3.5 that for fixed timings and a fixed first gradient moment m_1 , the amplitudes

of the two gradient lobes are linearly dependent on m_0 . This means that the amplitudes will be maximal at the extreme k-space lines ($\pm\hat{m}_0$). It follows that the minimal possible timings are achieved, if the amplitudes A_1 and A_2 are equal to $\pm\hat{A}$ for the extreme zeroth gradient moments $\pm\hat{m}_0$. Under these assumptions, the linear system of equations can be solved for the timings (neglecting physically non-meaningful solutions):

$$T_1 = \frac{\hat{A} \left(t_r \hat{A} + 2\hat{m}_0 \right) + \sqrt{\hat{A}^2 \left(t_r^2 \hat{A}^2 + 2\hat{m}_0^2 + 2\hat{A} \left(-2m_1 + (t_r + 2T_0) \hat{m}_0 \right) \right)}}{2\hat{A}^2} \quad (3.6)$$

$$T_2 = \frac{\hat{A} \left(t_r \hat{A} \right) + \sqrt{\hat{A}^2 \left(t_r^2 \hat{A}^2 + 2\hat{m}_0^2 + 2\hat{A} \left(-2m_1 + (t_r + 2T_0) \hat{m}_0 \right) \right)}}{2\hat{A}^2}.$$

This solution gives the minimal timings T_1 and T_2 for the bipolar gradient waveform that produces the zeroth gradient moment $\pm\hat{m}_0$ and the first gradient moment m_1 , without exceeding the system limitations. In order to differentiate between the two encoding schemes ECHO and ISO, different substitutions must be used in this general solution, which are given in table 3.1.

	scheme ECHO	scheme ISO
\hat{m}_0	$\hat{m}_0^{enc} - m_0^G$	$\hat{m}_0^{enc} - m_0^G$
m_1	$m_1^{enc} - m_1^G + TE \cdot \hat{m}_0^{enc}$	$m_1^{enc} - m_1^G$

Table 3.1: Necessary substitutions for equation 3.6.

Here, \hat{m}_0^{enc} denotes the maximal zeroth gradient moment needed for spatial encoding and m_1^{enc} the first gradient moment associated with velocity encoding. Furthermore, gradient moments that already exist on the gradient axis (e.g. from the slice-selection gradient) need to be considered. These are denoted by the terms m_0^G and m_1^G . For scheme ECHO the term $TE \cdot \hat{m}_0^{enc}$ is added in order to create a linear variation of m_1 along PE (SS) direction. The slope of this linear variation, given by TE , leads to a displacement along the PE (SS) axis given by equation 3.2 and linearly interpolates the reconstructed position of the magnetization in PE direction to its position at the center of the echo. Because higher orders of motion (e.g. acceleration) were neglected in the design of the encoding schemes, these lead to a bias in this interpolation.

The bipolar gradients on the RO axis are typically followed by the readout gradient, while

the bipolar gradients on the SS axis follow the slice-selection gradients. Therefore, the RO axis can be conveniently treated as a time-reversed SS axis when calculating the bipolar gradients. This symmetry simplifies the calculation, since the inversion of the time axis leaves even gradient moments unaffected, while all odd gradient moments only change their sign.

Equation 3.6 provides analytic solutions for minimal timings of the bipolar gradient, however, the finite gradient raster time (GRT, here 10 μs) and the minimum total duration of $2 \cdot t_r$ of the trapezoidal waveforms pose constraints. This means that the solutions for the timings have to be a multiple of the GRT. Furthermore, the given equations only hold true for timings above $2 \cdot t_r$, because they assume trapezoidal gradient lobes. For practical implementation, T_1 and T_2 were varied in discrete steps of GRT starting from $2 \cdot t_r$, and the respective amplitudes A_1 and A_2 were calculated according to equation 3.5. The pair of timings T_1 and T_2 that minimized the total duration $T_1 + T_2$, while the amplitudes A_1 and A_2 did not exceed \hat{A} , was then chosen as the optimal solution. In general, equation 3.4 can be formulated for triangular gradients ($T_1 < 2 \cdot t_r$ and/or $T_2 < 2 \cdot t_r$) and the optimal solution can be searched on the GRT grid starting from $2 \cdot GRT$. However, in practice, such short timings are rarely possible (mainly due to the spatial resolution and the corresponding large \hat{m}_0).

In the next step, these three different encoding schemes were extended to employ monopolar as well as bipolar multi-spoke excitation. According to the small-tip-angle approximation, the transverse magnetizations generated by a multi-spoke excitation equals the sum of the transverse magnetization generated by the different RF pulses and the gradient blips. If this superposition principle holds true, the magnetization generated by each individual pulse can be treated independently. This implies that for multi-spoke RF pulses multiple isophase points exist and, therefore, the gradient moments experienced by each magnetization subset, excited by each RF pulse, can be treated independently.

It then follows that each magnetization subset is acquired at a different echo time TE_i , where the index i counts through the number of RF pulses, since the RF pulses are played out after each other, but the signal is acquired in a single echo. Therefore, spatial displacements of different magnitudes $v_{RO} \cdot TE_i$ are induced in RO direction. In the reconstructed image, the overall effect is the sum of the effects on the individual magnetization subsets, which are each shifted according to their respective echo times. Since the difference between these individual shifts is on the order of the image resolution ($\approx 0.5\text{-}1.5\text{ mm}$) and each voxel contains a velocity distribution with a finite width, the result in the final image is expected to be a visual blurring rather than a distinct ghosting.

As explained in subsection 2.4.5, gradient blips with a nonzero m_0 have to be applied

after each RF pulse in order to distribute the spoke pulses in the k_x - k_y -plane. Typically, these gradient blips are trapezoidal gradients, which, however, have a finite first gradient moment. Therefore, a velocity-dependent phase is introduced between the RF pulses, resulting in a velocity-dependent magnitude modulation in the image. By applying bipolar gradient blips, their first gradient moment can be controlled.

Since the slice-selection gradients can be applied in a monopolar or bipolar fashion, both variants are investigated in this work. In the simplest form, monopolar excitation is achieved by using so-called flyback gradients between consecutive slice-selection gradients. These gradients have the same zeroth gradient moment as the slice-selection gradients, but are applied in the shortest possible way, i.e. with maximal gradient amplitude. For bipolar excitation the fastest approach is to switch from one slice-selection gradient to the next one with opposed polarity, without any additional gradients in between them. Since these two approaches (see figure 3.11) are the most time-effective, encoding scheme FAST was combined with them in order to achieve the fastest velocity-encoded multi-spoke excitation.

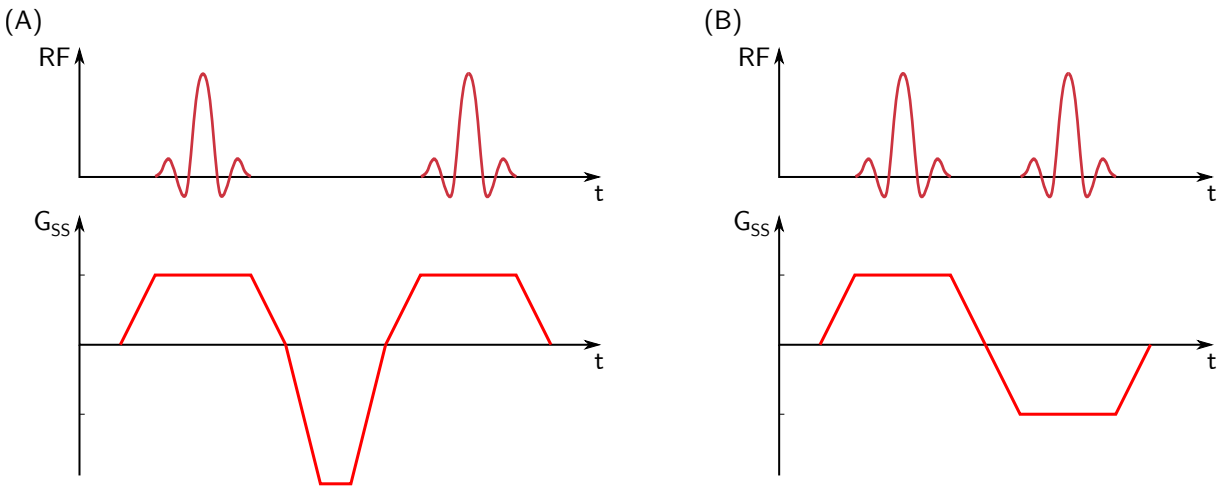


Figure 3.11: Conventional monopolar (A) and bipolar (B) multi-spoke RF excitation.

An important feature of this basic bipolar design is that it generates a non-zero first gradient moment $\Delta\vec{m}_1^*$ between consecutive spoke pulses along the SS direction for the central k-space line. Therefore, it introduces a phase difference between two excitations. As a result, even if two RF pulses are applied with identical shim settings in the center of the excitation k-space ($k_x=k_y=0$), the excitation profiles do not necessarily add up constructively, but rather yield a velocity-modulated signal

$$|s(\vec{v})| = |s(\vec{v} = 0)| \cdot |\cos(\gamma\Delta\vec{m}_1^* \cdot \vec{v})|. \quad (3.7)$$

For scheme ECHO and ISO, bipolar gradients were played out between consecutive slice-selection gradients and the nonzero first gradient moment of the slice-selection gradients is considered to achieve $\Delta\vec{m}_1^* = 0$ for the central k-space line. These gradients can be obtained from the same calculations as described above, but with different substitutions to equation 3.6 according to table 3.2

	scheme ECHO	scheme ISO
after the last spoke pulse		
\hat{m}_0	$\hat{m}_0^{enc} + m_0^{blip,N} - m_0^G$	$\hat{m}_0^{enc} + m_0^{blip,N} - m_0^G$
m_1	$m_1^{enc} - m_1^G + TE \cdot \hat{m}_0^{enc}$	$m_1^{enc} - m_1^G$
between spoke n & n+1		
\hat{m}_0	$m_0^{blip,n} - m_0^G$	$m_0^{blip,n} - m_0^G$
m_1	$-\Delta TE \left(\sum_{i=n+1}^N m_0^{blip,i} + m_0^{enc} \right) - m_1^G$	$-\Delta TE \left(\sum_{i=n+1}^N m_0^{blip,i} \right) - m_1^G$

Table 3.2: Necessary substitutions for equation 3.6 for multi-spoke excitation. ΔTE denotes the time between the isophase points of spoke n and $n + 1$.

The aim of scheme ECHO and ISO is to apply the same first gradient moment to all spoke pulses for the central k-space line in order to avoid a velocity-modulated signal. The central k-space line ($m_0^{enc} = 0$), however, does not necessarily correspond to $m_0 = 0$, calculated for each spoke pulse, because of the applications of gradient blips with finite zeroth gradient moments. This finite zeroth gradient moment as seen by the $(n + 1)^{th}$ spoke pulse leads to a finite first gradient moment as seen by the n^{th} spoke pulse (c.f. the properties of the gradient moments under temporal translation, e.g. equation 2.76). Thus, this first gradient moment has to be compensated by the gradients between the n^{th} and $(n + 1)^{th}$ spoke pulse, which is reflected by the term $\sum_{i=n+1}^N m_0^{blip,i}$.

3.2.2 Acceleration mapping

Similar to velocity quantification, a two-sided PC sequence was developed for acceleration mapping. In order to simultaneously control the zeroth, first and second gradient moment, tripolar encoding gradients were implemented into the sequence. Analogous to subsection 3.2.1, the following system of equations can be formulated.

$$\begin{aligned}
m_0 &= A_1 (T_1 - t_r) + A_2 (T_2 - t_r) + A_3 (T_3 - t_r) \\
m_1 &= A_1 (T_1 - t_r) \left(T_0 + \frac{T_1}{2} \right) + A_2 (T_2 - t_r) \left(T_0 + T_1 + \frac{T_2}{2} \right) \\
&\quad + A_3 (T_3 - t_r) \left(T_0 + T_1 + T_2 + \frac{T_3}{2} \right) \\
m_2 &= A_1 (T_1 - t_r) \left(\frac{T_1^2}{12} - \frac{T_1 t_r}{6} + \frac{t_r^2}{6} + \left(T_0 + \frac{T_1}{2} \right)^2 \right) \\
&\quad + A_2 (T_2 - t_r) \left(\frac{T_2^2}{12} - \frac{T_2 t_r}{6} + \frac{t_r^2}{6} + \left(T_0 + T_1 + \frac{T_2}{2} \right)^2 \right) \\
&\quad + A_3 (T_3 - t_r) \left(\frac{T_3^2}{12} - \frac{T_3 t_r}{6} + \frac{t_r^2}{6} + \left(T_0 + T_1 + T_2 + \frac{T_3}{2} \right)^2 \right)
\end{aligned} \tag{3.8}$$

Note that m_1 is always nulled for the central k-space line in order to eliminate any velocity-dependent phase. Here, again the same considerations apply as to velocity mapping. The ramp time is fixed by the maximal gradient amplitude and maximal slew rate of the gradient system, and minimal timings are achieved if the amplitudes A_1 , A_2 and A_3 equal the maximal possible gradient amplitude \hat{A} for the extreme k-space lines ($\pm\hat{m}_0$). Equation 3.8 can be solved for the amplitudes of the gradient lobes and the minimal timings are obtained by varying T_1 , T_2 and T_3 in steps of the GRT starting from $2 \cdot t_r$. The combination of gradient timings that minimize the sum $T_1 + T_2 + T_3$ without the amplitudes exceeding \hat{A} is then chosen as the optimal solution. Similar to velocity mapping, substitutions for \hat{m}_0 , m_1 , and m_2 have to be inserted into these solutions according to table 3.3. For acceleration mapping only encoding scheme ECHO was used in this work.

scheme ECHO	
\hat{m}_0	$\hat{m}_0^{enc} - m_0^G$
m_1	$-m_1^G + TE \cdot \hat{m}_0^{enc}$
m_2	$m_2^{enc} - m_2^G + \frac{1}{2}TE^2 \cdot \hat{m}_0^{enc}$

Table 3.3: Necessary substitutions for acceleration mapping.

Since the necessity of tripolar gradients leads to comparatively long encoding times, acceleration mapping was not combined with multi-spoke RF pulses in this work, however, this combination is generally feasible.

3.2.3 SYNC SPI

In order to acquire velocity data free of any bias due to non-synchronous spatial or velocity encoding time points, all encoding time points have to be synchronized. This can only be achieved by moving away from frequency encoding and applying a purely phase encoded method, known as single-point imaging (SPI). Based on this concept, Bruschi et al. [49] proposed a new PC MRI sequence, termed SYNC SPI (c.f. figure 3.12) that allows for highly accurate velocity measurements. Due its nature as a SPI sequence, the total acquisition time renders the sequence unfeasible for in vivo applications. However, since this method synchronizes all encoding time points and, therefore, minimized errors, it can provide gold standard velocity quantification for in-vitro studies, which in turn can be used to validate other methods.

In the context of this work, the sequence concept of the SYNC SPI was further developed to allow acceleration quantification with synchronized encoding time points. For this purpose, the bipolar gradients of the original SYNC SPI (c.f. figure 3.12) were replaced by tripolar gradients. In order to maintain the synchronization of the encoding time points, symmetrical tripolar gradients were used, whose central lobe is played out simultaneously with the spatial encoding gradients.

3.2.4 Reynolds stress tensor mapping

As described in the theory subsection 2.5.7, the RST can be obtained from the magnitude data of seven measurements acquired according to the encoding matrix given by equation 2.111. The encoding gradients of the applied sequence were calculated according to scheme ECHO as described in subsection 3.2.1.

3.2.5 B_1 mapping

For B_1 phase shimming and multi-spoke optimization, B_1 maps of all transmit channels are needed. Therefore, B_1 maps of the 8-channel transceiver body coil were acquired using a fast estimation technique as proposed by VAN DE MOORTELE et al. [50]. For this purpose, ten images were acquired in end-diastole of ten consecutive heartbeats. For the first image, all eight channels were in transmit mode, for the second no element was transmitting. For the remaining eight images one channel was in transmit mode each, while all elements were always used for reception. Thus, a matrix of ten times eight

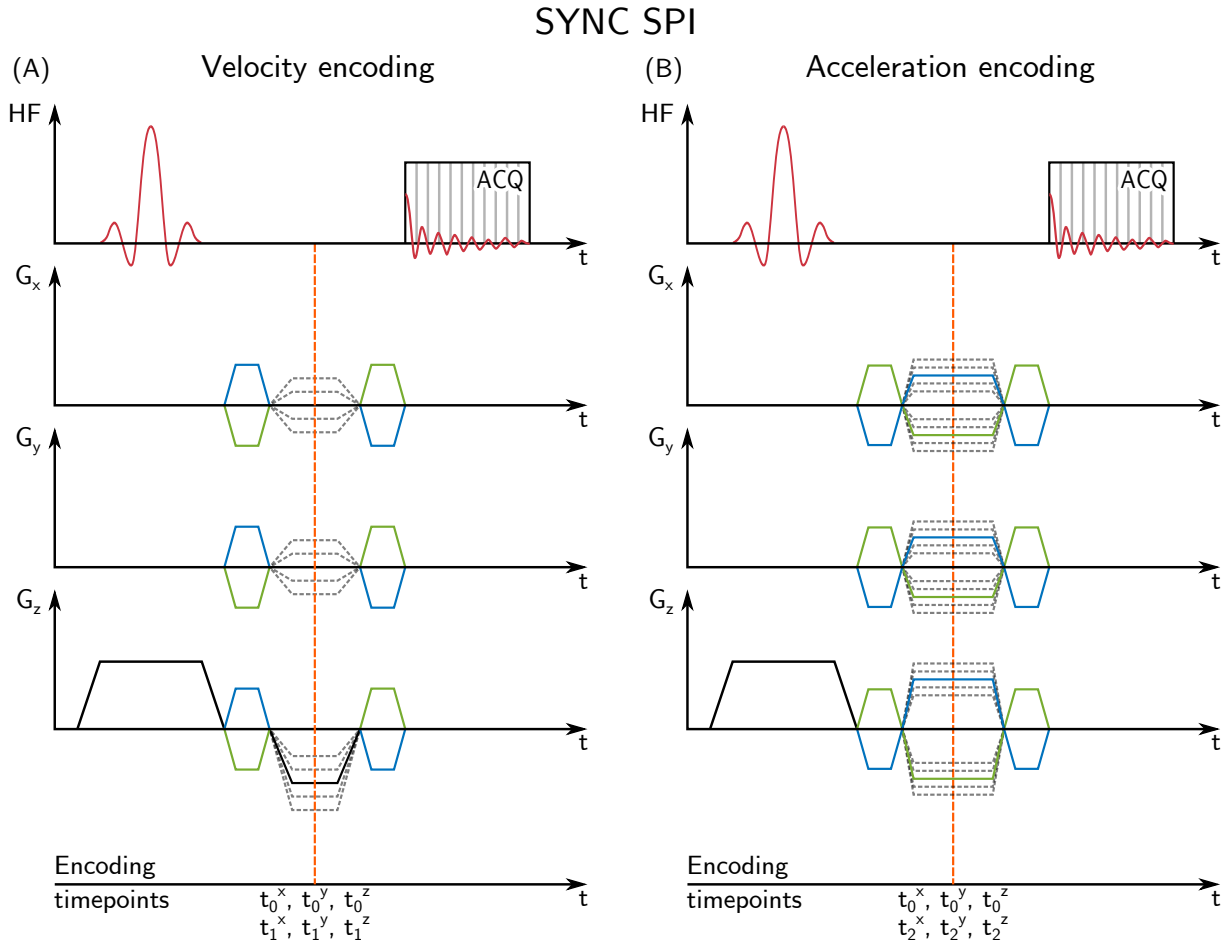


Figure 3.12: SYNC SPI sequence with synchronized encoding time points for velocity quantification (A) as proposed by Bruschewski et al. [49] and, as newly developed, for acceleration quantification (B). The blue and green gradients correspond to two measurements of a symmetric encoding along each axis.

images can be generated that can be used to estimate the transmit B_1 fields of all eight elements.

3.2.6 B_0 mapping

For multi-spoke optimization, knowledge of the off-resonance distribution ΔB_0 is necessary. Two gradient recalled echo acquisitions in end-diastole were acquired in two consecutive heartbeats with TE of 2.52 ms and 3.52 ms. The phase difference of these images is proportional to the off-resonance ΔB_0 (see equation 2.61).

3.3 Measurements

In the following section, measurements performed within the scope of this work are summarized.

3.3.1 Velocity encoded and compensated multi-spoke RF pulses

First, encoding scheme FAST was applied in a monopolar and bipolar 2-spoke fashion (measurement parameters can be found in table 3.4) in a rotation phantom study. The velocity-dependent signal modulation was investigated, which is predicted by equation 3.7.

Second, all three encoding schemes were applied in a 2-spoke fashion in phantom studies to investigate their influence on the reconstructed images and to quantify their associated displacement artifacts under controlled conditions. These experiments employed the straight flow phantom as well as the straight stenosis phantom (measurement parameters can be found in table 3.5).

Then, all three encoding schemes were applied in a 2-spoke fashion, targeting the femoral artery of a healthy volunteer. Finally, scheme ECHO was applied in vivo, targeting the human aorta in a transversal as well as in a sagittal-oblique slice. A non-optimized single-spoke excitation as well as optimized B_1 phase shimming and 2-spoke excitation were examined. Measurement parameters can be found in table 3.6.

3.3.2 Velocity encoded and compensated asymmetric multi-spoke RF pulses

In order to systematically investigate the performance of asymmetric multi-spoke RF pulses, these pulses were first applied in a phantom study using the straight flow phantom. Conventional symmetric pulses were compared to asymmetric pulses in a single- as well as a 2-spoke fashion with respect to the resulting excitation slice profiles and the quantified velocity.

Subsequently, 2-spoke excitation with both symmetric and asymmetric RF pulses was applied in vivo to quantify the blood velocity in the ascending and descending aorta of a healthy volunteer in a transverse slice.

Measurement parameters of all measurement using asymmetric RF pulses can be found in table 3.7.

3.3.3 Impact of the displacement artifact on WSS quantification

The influence of different encoding schemes on the estimation of WSS was evaluated in a phantom study with the basic model of a stenotic aorta. Scheme FAST and ECHO were applied in single-spoke fashion with two different orientations of the imaging axes with respect to the phantom. Additionally, the SYNC SPI sequence was applied. Due to the long scan time and the expectation that the quantified velocity is invariant with respect to the orientation of the imaging axis for the SYNC SPI, only a single measurement was performed. Corresponding measurement parameters can be found in table 3.8.

3.3.4 VENC optimization

Since under real conditions, the velocity distribution within each voxel can cover a broad spectrum, the effect of such distributions on the noise of PC velocity measurements was evaluated. First, velocity spectra were acquired in the straight flow phantom for different pump settings with constant flow rates by the use of a FOURIER velocity encoding sequence. The same measurements were repeated with a pump setting, which created pulsatile flow. Additionally, conventional PC velocity measurements were performed. The measurement parameters of the phantom study can be found in table 3.9. Finally, in vivo velocity spectra targeting the femoral artery of a healthy volunteer were acquired with the measurement parameters given in table 3.10.

3.3.5 Acceleration quantification

To evaluate the performance of the newly proposed acceleration-encoded SYNC SPI, the rotation phantom was used. In addition, an acceleration mapping sequence with encoding scheme ECHO was applied. 2D images were acquired with the slice selection axis parallel to the rotation axis. An overview of the complete acquisition parameters can be found in table 3.11.

With regard to in vivo measurements, acceleration maps targeting the human aorta at 7 T were acquired in combination with B_1 phase shimming to address spatial heterogeneous flip angles. To evaluate the differences between direct acceleration mapping and acceleration maps calculated from velocity data, additional measurements of the velocity vector field were performed. Corresponding measurement parameters can be found in table 3.12.

3.3.6 Reynolds stress tensor quantification

The velocity-encoding-related signal loss used to quantify the RST was acquired in a well-known fluid dynamic test case: the flow over periodic hills. Measurements were performed at a REYNOLDS number of $RE \approx 60,000$ at a constant flow rate of 255 mL/min at 22 °C. For background phase correction during the post-processing, additional measurement without flow, but otherwise identical settings, were performed. The ICOSA6 encoding was acquired with twelve different values of the first gradient moment (c.f. equation 2.111) ranging from 2.5 mT ms/m to 60 mT ms/m. See table 3.13 for further measurement parameters.

3.3.7 Measurement parameters

The following tables 3.5-3.10 summarize the acquisition parameters and pump settings of measurements performed within the scope of this work. If for example monopolar and bipolar multi-spoke excitation was used, which lead to different timings, corresponding minimal and maximal values are given. The same applies to the acquisition of individual components of the velocity or acceleration vector field in separate measurements. Furthermore, lines per cardiac phase define the number of phase encoding lines that are acquired during each cardiac cycle (R-R-interval). The temporal resolution of such an acquisition is then given by the product of TR, lines per cardiac phase and the number of the flow encodings (e.g. 2 if only one velocity component is quantified).

All in vivo experiments targeting the human heart and aorta were performed during breath-hold.

rotation phantom	
Encoding scheme	FAST
Number of spokes	2
2D / 3D	2D
Spatial resolution (mm ³)	1.0 x 1.0 x 4.0
FOV (mm ³)	144 x 144 x 4
TE[1] (ms)	5.4 - 6.6
TE[2] (ms)	4.2
TR (ms)	8.4 - 9.6
RO bandwidth (Hz/pixel)	340
Pulse duration (ms)	800
Pulse BWT	2.7
VENC (cm/s)	450
Flow encoding	3D
Averages	-
Acq. time (s)	4.8 - 5.5

Table 3.4: Acquisition parameters of the experiment using the rotation phantom for investigation of encoding scheme FAST in monopolar and bipolar 2-spoke fashion.

	straight flow phantom			stenosis flow phantom		
Encoding scheme	FAST	ECHO	ISO	FAST	ECHO	ISO
Number of spokes		2			2	
2D / 3D		3D			3D	
Spatial resolution (mm ³)		1.0 x 1.0 x 1.0			1.0 x 1.0 x 1.0	
FOV (mm ³)		160 x 160 x 120			192 x 192 x 96	
TE[1] (ms)	5.1 - 5.4	5.9 - 6.1	8.7 - 8.8	5.0 - 5.3	5.8 - 6.1	8.7 - 9.0
TE[2] (ms)	4.4	4.6	4.4	4.3	4.6	4.3
TR (ms)	7.8 - 8.1	8.6 - 8.8	11.4 - 11.5	7.7 - 8.0	8.5 - 8.8	11.4 - 11.5
RO bandwidth (Hz/pixel)		450			450	
Pulse duration (ms)		500			500	
Pulse BWT		6			6	
VENC (cm/s)		150			200	
Flow encoding		3D			3D	
Pump setting (mL/s)		150			30	
Acq. time (s)	598 - 619	657 - 672	877 - 885	568 - 591	627 - 645	838 - 847

Table 3.5: Acquisition parameters of the experiments used to examine the performance of the three different encoding schemes.

	heart / aorta				femoral artery		
	transversal		sagittal-oblique		FAST	ECHO	ISO
Encoding scheme			ECHO		FAST	ECHO	ISO
Number of spokes	1	2	1	2	2		
2D / 3D			2D		3D		
Spatial resolution (mm ³)			2.0 x 2.0 x 5.0		1.0 x 1.0 x 1.0		
FOV (mm ³)			192 x 84 x 5		144 x 144 x 40		
TE[1] (ms)	3.4	5.4	3.1 - 3.4	5.1 - 5.4	6.4	7.7	11.2
TE[2] (ms)	-	3.4	-	3.1 - 3.4	4.1	5.4	5.4
TR (ms)	5.7	7.7	5.4 - 5.7	7.4 - 7.7	9.3	10.6	14.2
Temporal resolution (ms)	34.2	30.8	32.4 - 34.2	29.6 - 30.8	55.9	42.5	56.7
RO bandwidth (Hz/pixel)			600		450		
Pulse duration (ms)			500		1000		
Pulse BWT			2.7		10		
VENC (cm/s)			150		150		
Flow encoding	through-plane		$v_x/v_y/v_z$ measured individually		through-plane		
Parallel imaging			GRAPPA		GRAPPA		
Acceleration factor			2		2		
Lines per phase	3	2	3	2	3	2	2
Cardiac phases	23	26	26-28	26-27	11	16	11
Acq. window (ms)	787	801	889-907	799-801	614	680	623
Acq. time (second)	16	21	16	22	689	1144	1048

Table 3.6: Acquisition parameters of the in vivo velocity mapping with multi-spoke RF pulses.

	phantom slice profile	phantom velocity mapping	heart / aorta
Encoding scheme	ECHO	ECHO	ECHO
Number of spokes	1 - 2	1 - 2	2
2D / 3D	3D	2D	2D
Spatial resolution (mm ³)	1.0 x 1.0 x 1.0	1.0 x 1.0 x 8.0	2.0 x 2.0 x 8.0
FOV (mm ³)	128 x 128 x 120	128 x 128 x 8	192 x 84 x 8
TE[1] (ms)	4.2 - 5.1	4.3 - 5.2	4.3 - 4.4
TE[2] (ms)	6.1 - 6.5	6.7 - 7.5	5.7 - 7.1
TR (ms)	50	7.5 - 10.8	8.5 - 9.8
Temporal resolution (ms)	-	-	33.9 - 39.1
RO bandwidth (Hz/pixel)	450	450	600
Pulse duration (ms)	800	800	800
Pulse BWT	7	7	7
VENC (cm/s)	-	120	170
Flow encoding	-	through- plane	through- plane
Parallel imaging	-	-	GRAPPA
Acceleration factor	-	-	2
Lines per phase	-	-	2
Cardiac phases	-	-	19 - 22
Acq. window (ms)	-	-	750
Pump setting (mL/s)	100	100	-
Averages	-	50	-
Acq. time (second)	768	48 - 69	14 - 17

Table 3.7: Acquisition parameters of the experiments using asymmetric spoke pulses.

stenotic aorta phantom			
Encoding scheme	FAST	ECHO	SYNC SPI
Number of spokes	1	1	1
2D / 3D	3D	3D	3D
Spatial resolution (mm ³)	1.0 x 1.0 x 1.0	1.0 x 1.0 x 1.0	1.0 x 1.0 x 1.0
FOV (mm ³)	224 x 224 x 32	224 x 224 x 32	96 x 72 x 80
TE (ms)	4.2	5.2	1.8
TR (ms)	7.0	7.9	15.0
RO bandwidth (Hz/pixel)	450	450	450
Pulse duration (ms)	400	400	400
Pulse BWT	10	10	10
VENC (cm/s)	250	250	250
Flow encoding	3D	3D	3D
Pump setting (mL/s)	40	40	40
Parallel imaging	-	-	GRAPPA
Acceleration factor	-	-	2
Averages	4	4	-
Acq. time (s)	803	906	17971

Table 3.8: Acquisition parameters of the sequences used to acquire velocity data in the stenotic aorta phantom. WSS estimation was based on this data.

VENC optimization phantom				
	constant flow		pulsatile flow	
Encoding scheme	ECHO	ECHO	ECHO	ECHO
Number of spokes	1	1	1	1
2D / 3D	2D	2D	2D	2D
Spatial resolution (mm ³)	1.0 x 1.0 x 5	1.0 x 1.0 x 5	1.0 x 1.0 x 5	1.0 x 1.0 x 5
FOV (mm ³)	128 x 128 x 5	128 x 128 x 5	128 x 128 x 5	128 x 128 x 5
TE (ms)	3.9	14.2	3.9	14.2
TR (ms)	6.8	17	6.8	17
Temporal resolution (ms)	-	-	13.6	17.0
RO bandwidth (Hz/pixel)	450	450	450	450
Pulse duration (ms)	800	800	800	800
Pulse BWT	2.7	2.7	2.7	2.7
VENC (cm/s)	85	-	100	-
Flow encoding	through-plane	FOURIER	through-plane	FOURIER
Parallel imaging	GRAPPA	GRAPPA	GRAPPA	GRAPPA
Acceleration factor	2	2	2	2
Lines per phase	-	-	1	1
Cardiac phases	-	-	56	43
Acq. window (ms)	-	-	730	730
Pump setting (mL/s)	20-80	20-80	pulsatile	pulsatile
Averages	10	5	10	3
Acq. time (second)	10	724	555	18641

Table 3.9: Acquisition parameters for the phantom experiments of the VENC optimization. The FOURIER velocity encoded sequences used a velocity FOV of 168 cm/s in combination with a velocity resolution of 1.5 cm/s.

VENC optimization in vivo		
Encoding scheme	ECHO	ECHO
Number of spokes	1	1
2D / 3D	2D	2D
Spatial resolution (mm ³)	1.0 x 1.0 x 5.0	1.0 x 1.0 x 5.0
FOV (mm ³)	128 x 128 x 5	128 x 128 x 5
TE (ms)	3.8	14.2
TR (ms)	6.6	17
Temporal resolution (ms)	13.2	17
RO bandwidth (Hz/pixel)	450	450
Pulse duration (ms)	800	800
Pulse BWT	2.7	2.7
VENC (cm/s)	100	-
Flow encoding	through-plane	FOURIER
Parallel imaging	GRAPPA	GRAPPA
Acceleration factor	2	2
Lines per phase	1	1
Cardiac phases	50	36
Acq. window (ms)	660	626
Acq. time (second)	50	5329

Table 3.10: Acquisition parameters of the in vivo VENC optimization. The FOURIER velocity encoded sequences used a velocity FOV of 168 cm/s in combination with a velocity resolution of 1.5 cm/s.

acceleration mapping rotation phantom		
Encoding scheme	ECHO	SYNC SPI
Number of spokes	1	1
2D / 3D	2D	2D
Spatial resolution (mm ³)	1.0 x 1.0 x 20.0	1.0 x 1.0 x 20.0
FOV (mm ³)	144 x 144 x 20	144 x 144 x 20
TE (ms)	8.0	3.4
TR (ms)	10.8	10.0
RO bandwidth (Hz/pixel)	450	450
Pulse duration (ms)	800	800
Pulse BWT	2.7	2.7
AENC (m/s)	500	1000
Flow encoding	3D	3D
Parallel imaging	-	-
Acceleration factor	-	-
Acq. time (second)	6	829

Table 3.11: Acquisition parameters of the acceleration mapping using the rotation phantom.

acceleration mapping in vivo		
	acceleration	velocity
Encoding scheme	ECHO	ECHO
Number of spokes	1	1
2D / 3D	2D	2D
Spatial resolution (mm ³)	2.0 x 2.0 x 5.0	2.0 x 2.0 x 5.0
FOV (mm ³)	380 x 166 x 5	380 x 166 x 5
TE (ms)	7.5 - 7.9	5.3 - 6.0
TR (ms)	10.3 - 10.7	8.2 - 8.8
Temporal resolution (ms)	41.0 - 42.6	32.6 - 35.2
RO bandwidth (Hz/pixel)	450	450
Pulse duration (ms)	800	800
Pulse BWT	2.7	2.7
VENC (cm/s)	-	150
AENC (m/s)	70	-
Flow encoding	$a_x/a_y/a_z$ measured individually	$v_x/v_y/v_z$ measured individually
Parallel imaging	GRAPPA	GRAPPA
Acceleration factor	2	2
Lines per phase	2	2
Cardiac phases	19	22 - 24
Acq. window (ms)	800	800
Acq. time (second)	22	22

Table 3.12: Acquisition parameters of the in vivo acceleration mapping.

periodic hills phantom	
Encoding scheme	ECHO
Number of spokes	1
2D / 3D	2D
Spatial resolution (mm ³)	1.0 x 1.0 x 6.0
FOV (mm ³)	496 x 120 x 6
TE (ms)	6.3
TR (ms)	10.0
RO bandwidth (Hz/pixel)	450
Pulse duration (ms)	1210
Pulse BWT	8
VENC (cm/s)	20 - 470
Flow encoding	ICOSA6
Averages	256
Acq. time (s)	2150

Table 3.13: Acquisition parameters of the experiments with flow over periodic hills.

3.4 Data analysis

Data analysis and post-processing was performed in MATLAB (The MathWorks Inc, Natick, Massachusetts, USA).

3.4.1 Background phase removal

Phase contrast measurements typically show a non-zero background phase that originates from induced eddy currents and concomitant fields (c.f. subsection 2.5.5). This background phase leads to non-zero velocity values in static tissue as well as to a bias in the flow regions. However, these effects can be removed from the reconstructed images.

After the phase difference between the flow encoded measurements was calculated, a 3rd order polynomial was fitted to the spatially varying background phase in a manually defined ROI. This ROI was defined based on the knowledge of the location of static tissue. The polynomial thus determined was then evaluated over the entire image and the resulting phase was subtracted from the image.

3.4.2 VENC optimization

Assuming a velocity distribution $p(\vec{v})$ within a voxel, the measured complex signal $s(\vec{m}_1)$ can be calculated as

$$s(\vec{m}_1) = \int_{-\infty}^{\infty} p(\vec{v}) \cdot e^{i\gamma\vec{v}\cdot\vec{m}_1} d\vec{v}, \quad (3.9)$$

if a first gradient moment \vec{m}_1 is applied for velocity encoding ($\vec{m}_i = 0$ for $i \neq 1$). Assuming white GAUSSIAN noise in the real and imaginary part of the signal with the same variance σ , error propagation can be applied to calculate the corresponding noise in the magnitude ($\sigma_{|s|}$) and phase data (σ_φ) of the image.

$$|s| = \sqrt{\text{real}(s)^2 + \text{imag}(s)^2} \quad \Rightarrow \quad \sigma_{|s|} = \sigma \quad (3.10)$$

$$\varphi = \tan^{-1} \left(\frac{\text{imag}(s)}{\text{real}(s)} \right) \quad \Rightarrow \quad \sigma_\varphi = \frac{\sigma}{|s|} \quad (3.11)$$

Furthermore, the noise in the phase difference image is given by

$$\sigma_{(\varphi_1 - \varphi_2)} = \sqrt{\frac{\sigma^2}{|s_1|^2} + \frac{\sigma^2}{|s_2|^2}}. \quad (3.12)$$

Finally, it follows for the velocity noise:

$$\sigma_v = \sqrt{\frac{\sigma^2}{\left| \int_{-\infty}^{\infty} p(\vec{v}) \cdot e^{i\gamma\vec{v}\cdot\vec{m}_{1,1}} d\vec{v} \right|^2} + \frac{\sigma^2}{\left| \int_{-\infty}^{\infty} p(\vec{v}) \cdot e^{i\gamma\vec{v}\cdot\vec{m}_{1,2}} d\vec{v} \right|^2}} \cdot \frac{1}{\gamma |\vec{m}_{1,1} - \vec{m}_{1,2}|} \quad (3.13)$$

In the special case of a symmetric encoding (i.e. $\vec{m}_{1,2} = -\vec{m}_{1,1}$), equation 3.13 simplifies to

$$\sigma_v = \frac{\sqrt{2}\sigma}{\gamma |2\vec{m}_{1,1}| \cdot \left| \int_{-\infty}^{\infty} p(\vec{v}) \cdot e^{i\gamma\vec{v}\cdot\frac{\vec{m}_{1,1}}{2}} d\vec{v} \right|}. \quad (3.14)$$

Often an increase of $\vec{m}_{1,1}$ is desired to reduce the velocity noise σ_v , but in fact equation 3.14 shows that in the case of a intravoxel velocity distribution with a finite width, there are two competing mechanisms. First, it decreases the velocity noise by $\frac{1}{|2\vec{m}_{1,1}|}$, but at the same time, also increases the velocity noise by $\frac{1}{\left| \int_{-\infty}^{\infty} p(\vec{v}) \cdot e^{i\gamma\vec{v}\cdot\frac{\vec{m}_{1,1}}{2}} d\vec{v} \right|}$. Here, the latter term represents the signal loss due to intravoxel dephasing. Therefore, there exists an optimal $\vec{m}_{1,1}$, corresponding to an optimal $VENC_{opt}$ that minimizes the velocity noise σ_v .

3.4.3 Wall shear stress estimation

WSS estimation performed within the scope of this work is based on the method proposed by POTTERS et al. [51]. In general, the WSS can be obtained from the measured velocity vector field as stated by equation 2.122. For this, however, the vessel lumen must first be segmented and then points on its surface have to be defined, at which the WSS is then evaluated. This is done by smoothing the surface using a LAPLACIAN filter. In principle, the general expression of the WSS can be evaluated at these points, but in practice, the following steps are applied to simplify the calculation:

- Transformation into a local coordinate system $[x', y', z'] = R \cdot [x, y, z]$ that aligns the z' -axis with the inward normal vector by applying an appropriate rotation R .
- Assumption of no flow through the vessel wall ($\vec{v}' \cdot \vec{n}' = 0$), which reduces equation 2.122 to $\vec{\chi}' = \mu \left[\frac{\partial v_{x'}}{\partial z'}, \frac{\partial v_{y'}}{\partial z'}, 0 \right]$.
- Calculation of the spatial derivatives $\frac{\partial v_{x'}}{\partial z'}$ and $\frac{\partial v_{y'}}{\partial z'}$ in the rotated coordinate system.
- Transformation back into the original coordinate system by the inverse rotation R^{-1} .

In the third step, a smoothing spline is fitted to the transformed velocity \vec{v}' in order to determine the derivative at the vessel wall. Additionally, a velocity value of zero is manually imposed at the vessel wall (zero forcing), but the weight of this point is ten times lower than for the velocity values on the inward normal vector. In this way, the WSS was determined at any point on the vessel surface.

3.4.4 Reynolds stress tensor quantification

The RST was obtained from the measured data by two different methods, which both calculate the RST according to equation 2.113. For this purpose, the magnitude of the twelve ICOSA6-encoded measurements was first normalized with the respective velocity-compensated measurements. Afterwards, a 3D GAUSSIAN was fitted to this data.

For the first method, the RST was calculated by fitting the GAUSSIAN individually for every encoding value $|\vec{m}_1|$ as proposed by HARALDSSON et al. [20].

For the second method, the GAUSSIAN was fitted to the magnitude data of all twelve measurements. To avoid magnitude offsets due to the RICIAN nature of the magnitude noise, data points with less than 10% of the normalized magnitude were excluded from the fit.

Additionally to the quantification of the RST, the velocity vector field was estimated from the data corresponding to the five lowest $|\vec{m}_1|$ values. This was done by solving the following optimization problem to obtain the estimate \hat{v} :

$$\{\hat{v}\} = \arg \min_v \left[- \left\| e^{i\gamma v \vec{m}_1} \cdot e^{-i\vec{\phi}} \right\| \right]. \quad (3.15)$$

Here, $\vec{\phi}$ is the phase of the measured data and \vec{m}_1 a vector that contains the first gradient moments of the measurements.

4 Results

In the results chapter the quantification of different fluid mechanical properties is presented. First, different encoding schemes for velocity quantification are investigated, which are consecutively expanded towards multi-spoke excitation. Additionally, asymmetric RF pulses are applied in a single-spoke and 2-spoke fashion for the quantification of the velocity vector field. Then, the influence of different encoding schemes on the estimated wall shear stress is evaluated, before the optimization of the VENC value, under consideration of intravoxel velocity distributions, is presented. Furthermore, results of direct quantification of the acceleration vector field are shown. Last, the REYNOLDS stress tensor is quantified in flow over periodic hills.

The results presented in this chapter are adapted from several publications by SCHMIDT et al. [52–58].

4.1 Velocity encoded and compensated multi spoke RF pulses

4.1.1 Gradient waveform design

As discussed in subsection 3.2.1, three different encoding schemes were investigated within the scope of this work and extended towards multi-spoke excitation. However, single-spoke excitations are considered first.

Single-spoke excitation

Figure 4.1-4.3 show the corresponding sequence diagrams of a 3D imaging experiment with single-spoke excitation, as well as the zeroth and first gradient moment along all axes. Note that the gradient moments are calculated starting from the isophase point of the RF pulse (c.f. equation 2.73). For PE and SS direction, three different k-space lines are illustrated and color-coded. Furthermore, the corresponding spatial encoding time points are marked by dashed orange lines. Along the RO direction, all three encoding schemes are equivalent. m_0^{RO} varies linearly during the data acquisition, corresponding to the sampling of a complete line in k-space. Additionally, there is a quadratic change of m_1^{RO} during that period. Because of this, the spatial encoding time point along the RO

direction is at the center of the echo for all encoding schemes (c.f. Wedeen et al. [38]). The three encoding schemes, however, differ in their respective PE and SS axes.

For scheme FAST (figure 4.1), the encoding gradients lead to linear variations of the first gradient moments m_1^{PE} and m_1^{SS} with variable slopes. These correspond to different spatial encoding time points along these axes. In contrast, scheme ECHO (figure 4.2) linearly approximates the variation of m_1^{RO} along the PE and SS direction by varying m_1^{PE} and m_1^{SS} accordingly. This leads to a synchronization of the spatial encoding time points, located at the center of the echo. The third encoding scheme, scheme ISO (figure 4.3), however, applies constant first gradient moments m_1^{PE} and m_1^{SS} for all k-space lines, corresponding to spatial encoding time points at the isophase point of the RF pulse.

Multi-spoke excitation

For multi-spoke excitation, multiple isophase points exist and, therefore, the gradient moments for each magnetization subset can be calculated independently. Figure 4.4-4.9 illustrate the sequence diagrams of a 3D imaging experiment with 2-spoke excitation for all three encoding schemes. Here, the same color-coding applies as for the single-spoke case, but the additional gradient moments corresponding to the second RF pulse are shown in dashed lines. In the given examples, gradient blips of $m_0^{RO}=m_0^{PE}=-1000/500$ mT μ s/m were applied between/after the spoke pulses. These become apparent as symmetrical offsets of the zeroth gradient moments of the two pulses in the magnified parts in figure 4.4-4.9. These gradient moments are used to control the in-plane excitation pattern and, thereby, to achieve a homogeneous excitation. Furthermore, the variation of m_1^{RO} during the data acquisition differs for the two RF pulses due to the difference in their respective TE values. This leads to displacements of different magnitudes of the magnetizations excited by each RF pulse.

The monopolar case of encoding scheme FAST (figure 4.4) leads, similar to the single-spoke case, to linear variations of m_1^{PE} and m_1^{SS} with variable slopes, but here not only between the PE and SS axes, but also between the 1st and 2nd spoke pulse. This corresponds to differences of the magnitude of the displacements, not only for the magnetizations excited by the individual RF pulses, but also along the PE and SS axes.

Encoding scheme FAST with bipolar spoke pulses (figure 4.5), in contrast, additionally leads to a finite first gradient moment Δm_1^* between the two spoke pulses in SS direction for the central k-space line. This Δm_1^* generates a velocity-dependent phase between the magnetizations excited by each spoke RF pulse. As a result, a velocity-dependent signal modulation, as described by equation 3.7, is expected.

A flyback gradient between two consecutive slice-selection gradients does not produce a

finite first gradient moment along the SS axis between these pulses. Therefore, a flyback gradient was also used in the monopolar 2-spoke case of encoding scheme ECHO (figure 4.6). This results in shorter inter-spoke periods ΔTE . Scheme ECHO produces linear variations of m_1^{PE} and m_1^{SS} along PE and SS k-space lines with identical slopes for the two axes, but different slopes for the two spoke pulses. The different slopes between the two spoke pulses account for the different slopes of the m_1^{RO} variation during the data acquisition period. Therefore, the magnitude of the displacement differs between the two spoke pulses, but not between the different encoding axes.

The bipolar case of scheme ECHO (figure 4.7) produces equivalent gradient moments, however, it requires a bipolar gradient between the two consecutive slice-selection gradients and, therefore, leads to an increased minimal TR value. Furthermore, encoding scheme ECHO synchronizes the spatial encoding time points of all spoke pulses and encoding axes at the center of the echo. Therefore, the corresponding displacement artifact is given by equation 3.2 and points along the velocity vector.

Unlike the two previously mentioned encoding schemes, scheme ISO (figure 4.8 and 4.9) keeps the first gradient moments m_1^{PE} and m_1^{SS} constant for all k-space lines and all RF pulses. This requires bipolar gradients between consecutive slice selection gradients in both, the monopolar and bipolar case. Furthermore, these bipolar gradients have to be adapted for every k-space line and lead to an increased inter-spoke period ΔTE . Due to the prolonged ΔTE , the slopes of the m_1^{RO} variations differ the most for scheme ISO.

4.1.2 Phantom measurements

Rotation phantom

Experiments in the rotation phantom were performed, to verify the effect of a finite first gradient moment Δm_1^* between two spoke pulses in the bipolar case of encoding scheme FAST (c.f. subsection 3.2.1 and figure 4.5). The corresponding results are illustrated in figure 4.10. The figure shows a 2D imaging experiment with the slice-selection direction oriented parallel to the rotation axis of the phantom with both, monopolar and bipolar, 2-spoke excitation. The velocity in figure 4.10A+B increases linearly from left to right from -4 m/s to 4 m/s. As predicted by the theory, the bipolar case of scheme FAST (figure 4.10A) leads to a velocity dependent signal cancellation, which is absent in the monopolar case. The corresponding velocity map, shown in figure 4.10B, shows increased velocity noise in the regions of reduced signal around $v = \pm 1.8$ m/s. Outside these regions, monopolar and bipolar excitation lead to identical velocity quantification (figure 4.10D). The finite first gradient moment Δm_1^* solely arises from the slice-selection gradi-

ents and can, therefore, be calculated for given sequence parameters. Δm_1^* decreases with increasing slice thickness, if the pulse duration and bandwidth time product are fixed and the resulting signal modulation can be well described by equation 3.7, as demonstrated by the fit to the magnitude data in figure 4.10C.

It was experimentally verified, that this effect does only occur in the bipolar case of encoding scheme FAST and that such artifacts are not observed when the other encoding schemes are applied.

Straight phantom

In the next step, the effect of the different encoding schemes on the reconstructed images were investigated with regard to geometrical distortions in the magnitude images as well as differences in the quantified velocities. First, all three encoding schemes were applied with monopolar and bipolar two-spoke excitation in a phantom experiment employing the phantom with straight pipes (only the pipe with largest diameter was investigated, c.f. figure 3.7) with a mean velocity of 120 cm/s. The corresponding magnitude images and velocity maps are displayed in figure 4.11-4.14. The effect of the orientation of the imaging axes with respect to the flow direction was studied by performing each acquisition twice, first with the RO direction through-plane, i.e. orthogonal to the velocity, and second with RO along the left-right direction, thus approximately 45° oblique with respect the velocity direction.

As described in subsection 3.2.1, encoding scheme FAST leads to spatial shifts oblique to the velocity vector that are dependent on the orientation of the imaging axes with respect to the velocity vector. As a consequence, in all cases in which encoding scheme FAST was applied, the content of the pipe appears displaced by up to 2 mm relative to the static surrounding tissue. Thus, moving spins are spatially shifted into the wall of the tube, which results in an asymmetric shape of the symmetric tube boundary (green arrows in figure 4.11 and 4.13). Since encoding scheme ECHO produces a shift parallel to the velocity vector, the symmetry of the tube boundary is maintained in the corresponding images, even if the orientation of the imaging axes is swapped. The shift along the velocity vector, however, can be clearly seen by the distorted tagging pattern that was imposed on the images. In the special case of encoding scheme ISO in combination with the RO direction orthogonal to the flow (figure 4.11C and 4.13C), perfect encoding, i.e. no displacement and no distortion of the tagging pattern, can be observed. If, however, scheme ISO is applied with a finite velocity component along the RO direction, substantial displacements along the RO direction are observed, leading to signal from flowing magnetization aliasing into surrounding static tissue (yellow arrows in figure 4.11F and 4.13F). At this point, it is important to note that the distortions of the tagging

patterns shown in figure 4.11 and 4.13 are not given by the equations 3.1-3.3, since the tagging pattern originates from opposing linear phases of the magnetizations excited by each spoke pulse, that are imposed by the gradient blips. As described in subsection 3.2.1, these gradient blips are incorporated into the bipolar encoding gradients and are applied subsequent to the RF pulses. This leads to a displacement of the tagging pattern that depends on the timing of these gradients, which themselves depend on the applied imaging parameters and the applied encoding scheme. One can summarize that the tagging pattern is a suitable tool to visualize the displacement artifacts of the various encoding schemes, but the absolute shift distances of the signal voids do not correspond to the overall shift of the individual magnetizations given by the equations 3.1-3.3.

The impact of the different encoding schemes on the quantified velocity vector field are shown in figure 4.12 and 4.14. The magnitude of the velocity is shown for all three encoding schemes and again two different orientations of the imaging axes with respect to the flow. The velocity profiles perpendicular to the tube clearly show the differences between the encoding schemes. In the case of vanishing flow in RO direction (figure 4.12D and 4.14D), encoding schemes ECHO and ISO give similar results. However, while encoding scheme ECHO produces consistent results also for the RO direction oblique to the flow, encoding scheme ISO leads to shifts of the maximum velocity of up to 4 mm in this case (figure 4.12H and 4.14H). Independent of the orientation of the imaging axes, encoding scheme FAST always leads to shifts of the maximum velocity of up to 2 mm. The quantified peak velocity, however, is independent on the encoding scheme and orientation of the imaging axes.

Stenosis phantom

The stenosis phantom illustrates that the different encoding schemes do not only lead to a displacement of the vessel, but can also substantially influence the quantified velocities within the vessel (figure 4.15 and 4.16). Although a pump setting with constant volume flow rate over time has been selected, the stenosis leads to significant acceleration terms. In accordance with the explanations in subsection 2.5.3, the velocity encoding time points thus become relevant here. While encoding scheme ECHO (figure 4.15B+E and 4.16B+E) and encoding scheme ISO with RO perpendicular to the flow (figure 4.15C and 4.16C) do not lead to distortions of the geometry of the stenosis, encoding scheme FAST yields distortions that depend on the orientation of the imaging axes of up to 3 mm (figure 4.15A+D and 4.16A+D). Additionally, scheme ISO yields a small region (green arrow in figure 4.15C and 4.16C) with altered signal intensity due to higher orders of motion (acceleration). Furthermore, encoding scheme ISO with RO oblique to the flow (figure 4.15F and 4.16F) renders the reconstructed image useless due to substantial displacement

artifacts.

Concerning the quantified velocity, encoding scheme FAST leads to a displacement of up to 5 mm of the maximum velocity downstream along the velocity direction if the RO direction is oblique to the flow (figure 4.15D and 4.16D). In contrast, the maximum velocity in the case of the RO perpendicular to the flow (figure 4.15A and 4.16A) is obtained at the correct position, the middle of the stenosis. Independent of the orientation of the imaging axes, the maximum velocity appears 8 mm downstream from the stenosis for encoding scheme ECHO (figure 4.15B+E and 4.16B+E). Encoding scheme FAST yields the maximum velocity in the center of the stenosis, if the RO direction is orthogonal to the flow (figure 4.15C and 4.16C), but leads to heavily distorted velocity maps if the RO direction is switched.

4.1.3 In vivo measurements

Femoral artery

A comparison of the three different encoding schemes in vivo is shown in figure 4.17. The femoral artery was selected as the target and the imaging axes were chosen such that the flow is strictly in the through-plane direction. Two-spoke excitation was applied, but without any gradient blips. The images shown are from mid-systole, as this phase of the cardiac cycle shows the greatest velocities and, thus, the greatest displacement artifacts occur. The red line in each image marks the center of mass of the signal intensity along the SS direction. Since the RO direction is orthogonal to the flow, encoding scheme ISO leads to no visible flow-induced displacement artifacts. Encoding scheme FAST and ECHO, however, lead to displacements of the center of mass of up to 2.6 mm and 4.6 mm, respectively.

Aorta transversal

After examining the three different encoding schemes for the displacement artifacts associated with them, encoding scheme ECHO was applied in vivo, targeting the ascending and descending aorta of a healthy volunteer with the explicit aim of flip angle homogenization. Resulting magnitude images and through-plane velocity maps during mid-systole using two-spoke excitation in comparison to the CP^+ mode¹ and B_1^+ phase shimming are illustrated in figure 4.18. The two-spoke excitation as well as the B_1^+ phase shim were optimized for the same ROI, marked in red. The non-optimized CP^+ mode leads

¹The CP^+ mode (circular polarized) is characterized by the fact that each of the eight transmitter elements is driven with the same amplitude, but with a 45° phase shift in succession. This results in a 360° phase cycle

to a local signal loss in the ascending aorta (red arrow in figure 4.18A) and an associated increased velocity noise at this location. Two-spoke excitation and B_1^+ phase shimming, in contrast, yield increased excitation homogeneity within the ROI. The corresponding mean volume flow in the ascending and descending aorta is shown in figure 4.18B for all three excitation schemes. A quantitative comparison between B_1^+ phase shimming and two-spoke excitation, as illustrated by the Bland-Altman plot in figure 4.18C, yields a mean difference throughout the cardiac cycle of 0.8 mL/s with a standard deviation of 16.2 mL/s.

Aorta sagittal-oblique

In addition, three directional velocity maps in mid-systole were acquired in a sagittal-oblique view of the aorta of the same volunteer, as shown in figure 4.19. Here, only B_1^+ phase shimming and two-spoke excitation was applied and the RO direction was oriented in head-feet direction. Similar to the transverse slice, both excitations yield a good flip angle homogeneity within the ROI. The mean velocity over the cardiac cycle was evaluated in the aortic arch and the corresponding data is illustrated in figure 4.19B as well as the corresponding Bland-Altman plot in figure 4.19C. The mean difference, averaged over the cardiac cycle between B_1^+ phase shimming and two-spoke excitation, was found to be 0.0 cm/s with a standard deviation of 3.8 cm/s.

No significant differences in mean volume flow and mean velocities were found between B_1^+ phase shimming and two-spoke excitation using a one-sample t -test ($p > 0.7$)

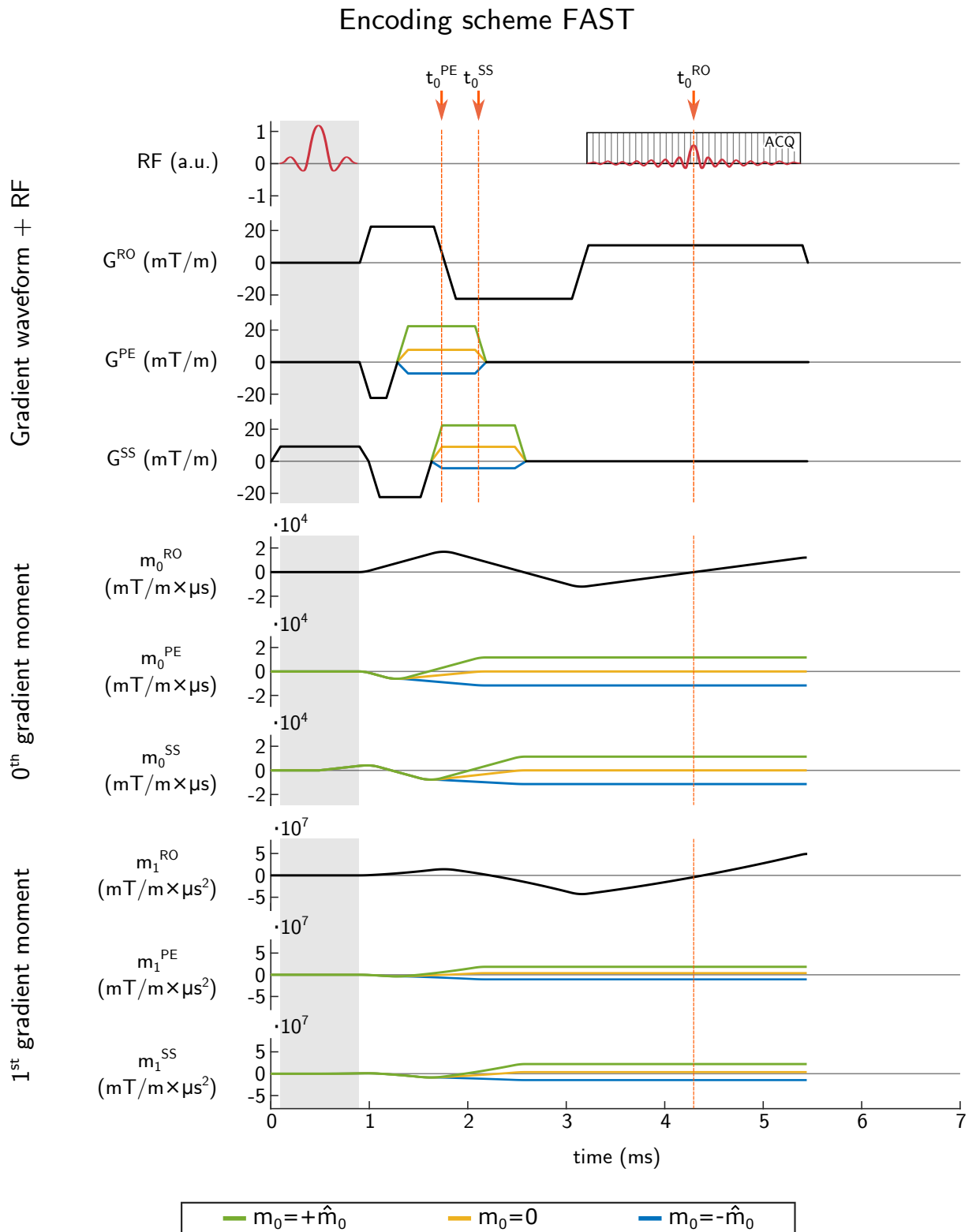


Figure 4.1: Calculated gradient waveforms and corresponding gradient moments for a single-spoke excitation using encoding scheme FAST.

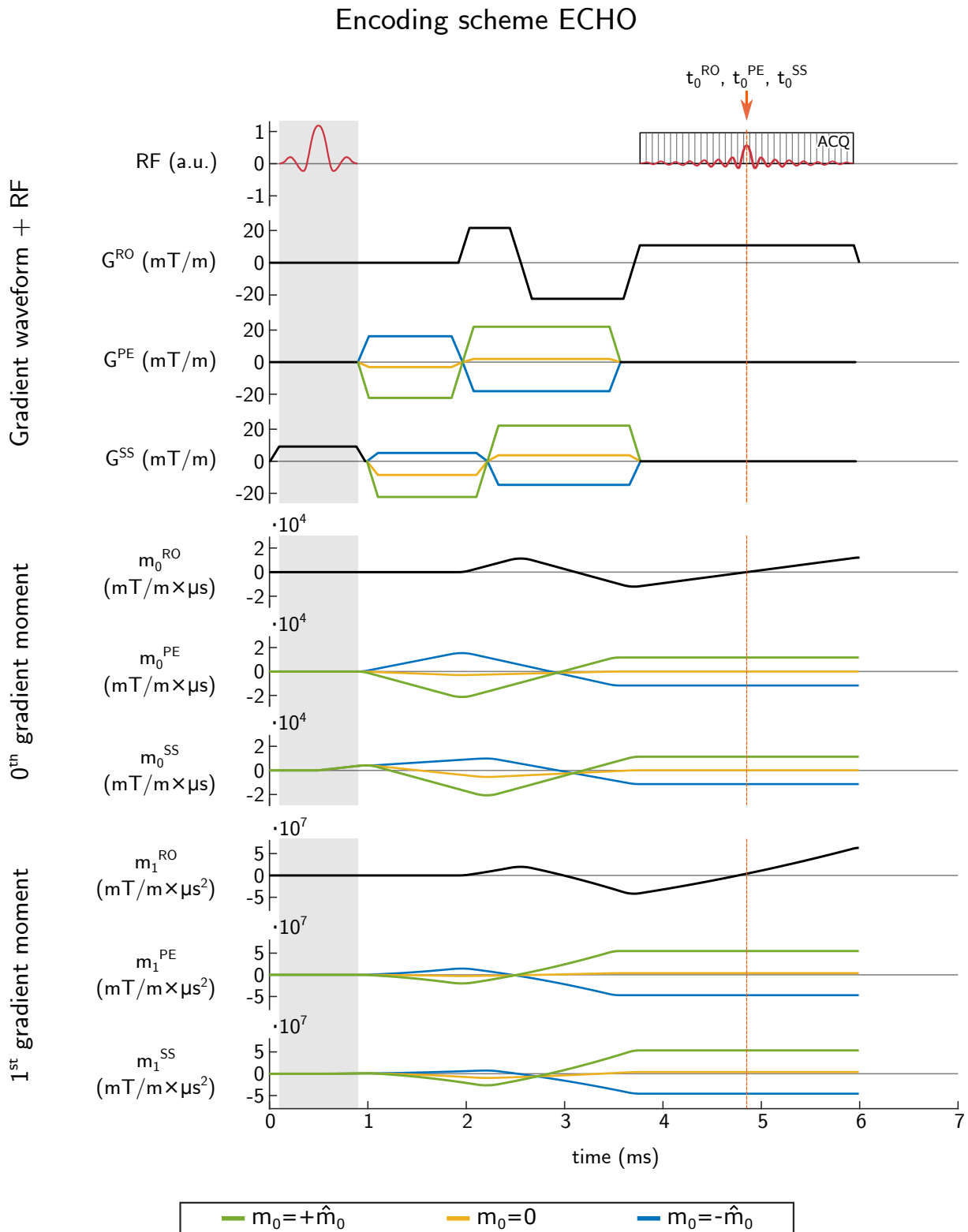


Figure 4.2: Calculated gradient waveforms and corresponding gradient moments for a single-spoke excitation using encoding scheme ECHO.

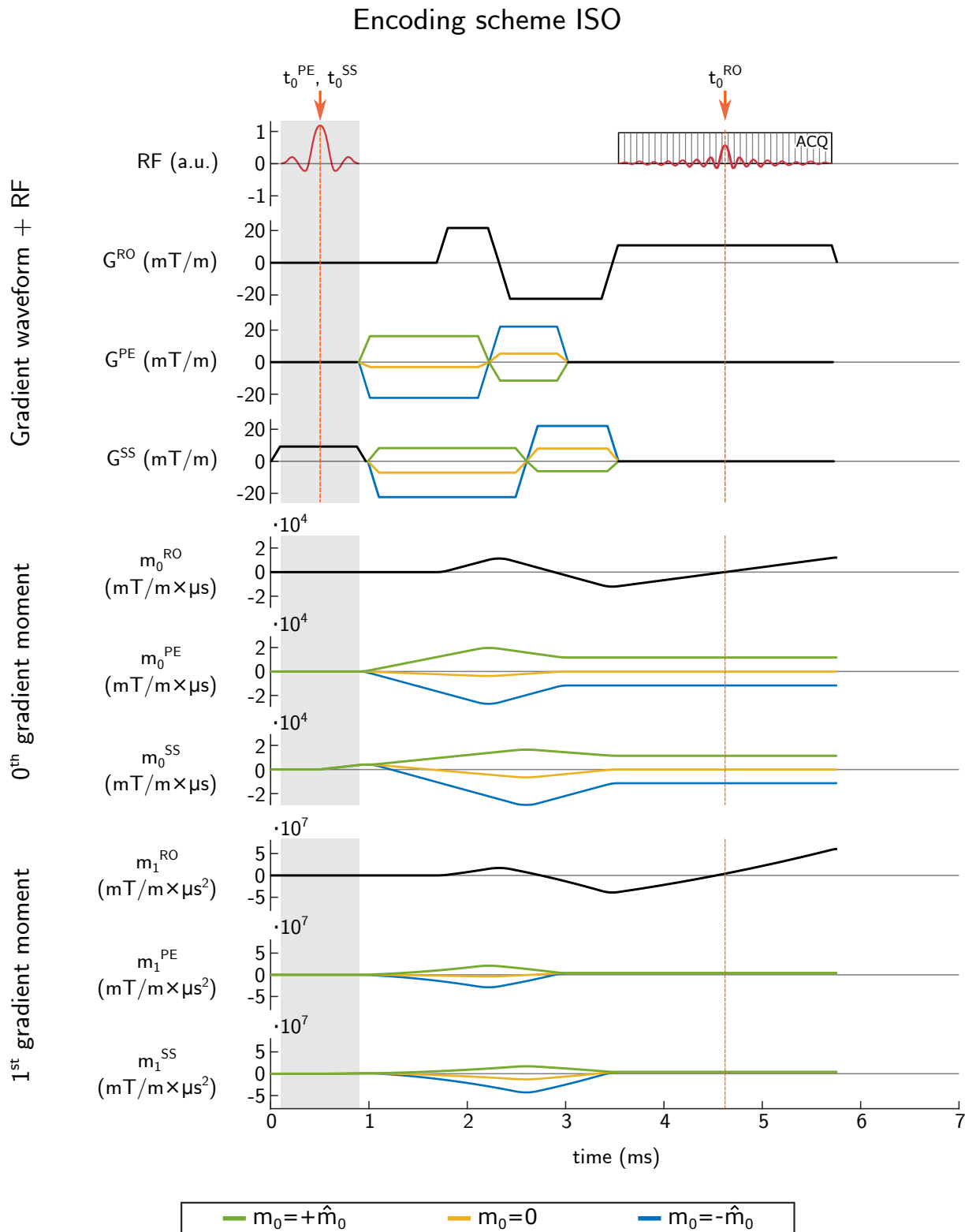


Figure 4.3: Calculated gradient waveforms and corresponding gradient moments for a single-spoke excitation using encoding scheme ISO.

Encoding scheme FAST 2-spoke monopolar

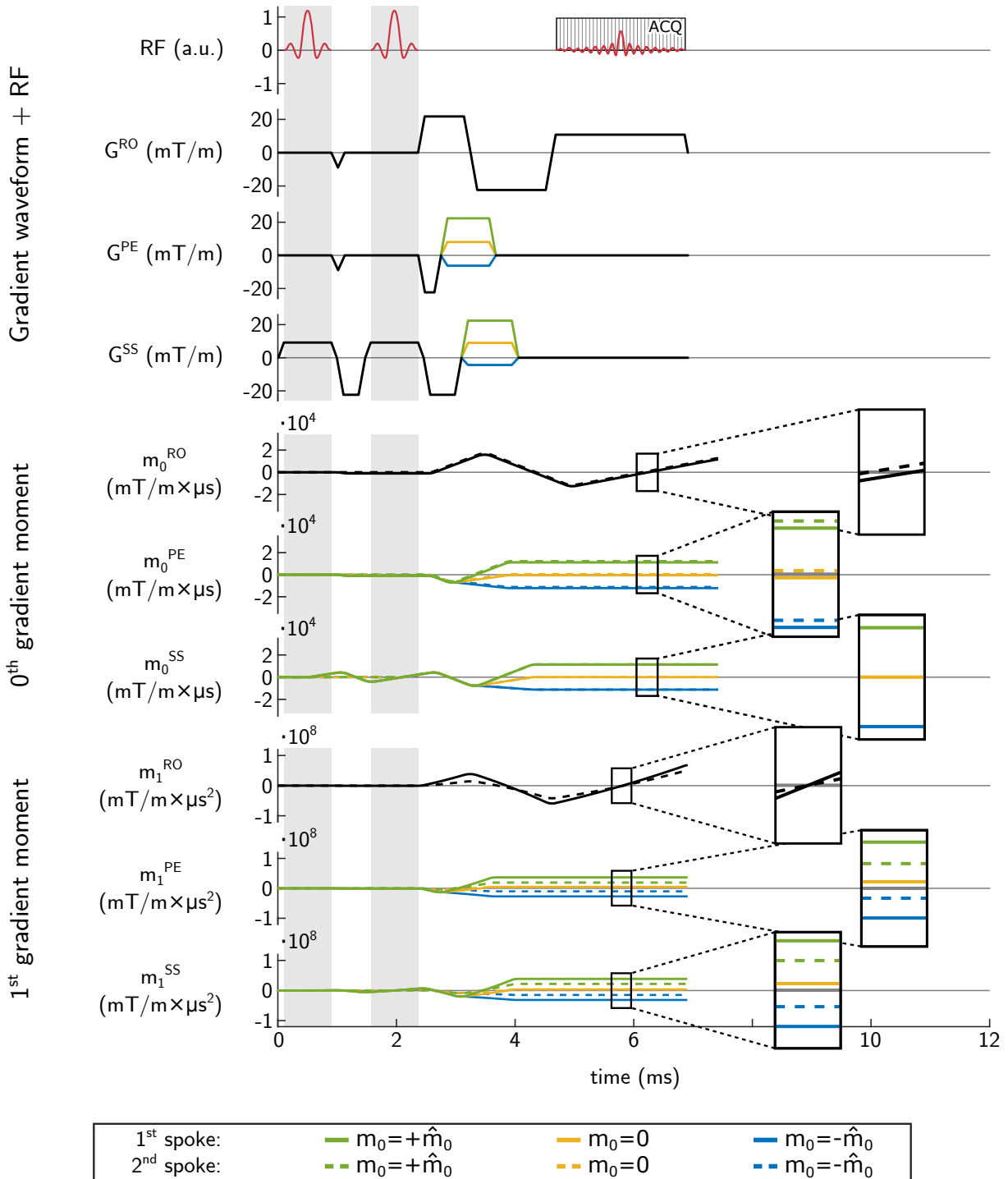


Figure 4.4: Calculated gradient waveforms and corresponding gradient moments for monopolar two-spoke excitation using encoding scheme FAST.

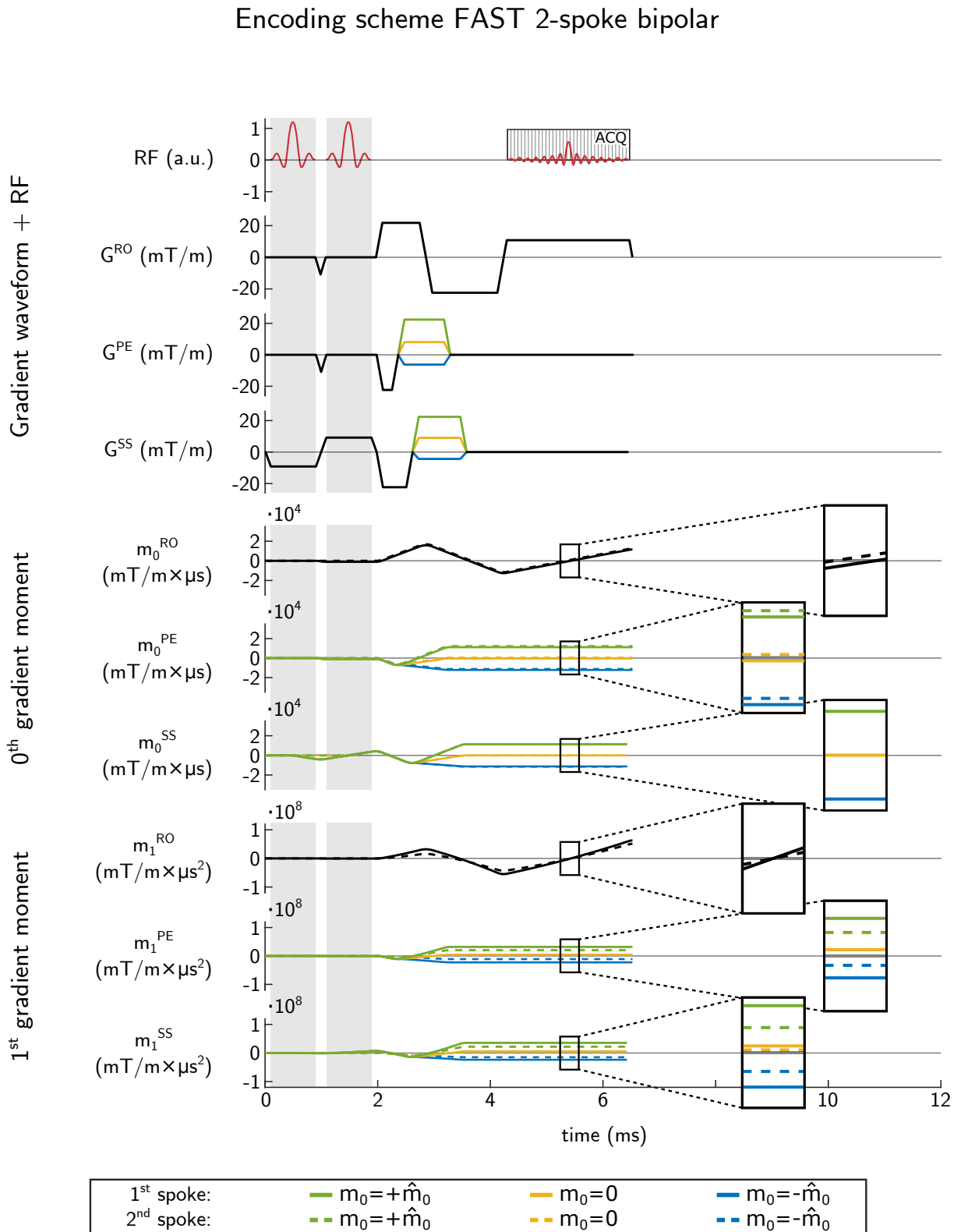


Figure 4.5: Calculated gradient waveforms and corresponding gradient moments for bipolar two-spoke excitation using encoding scheme FAST.

Encoding scheme ECHO 2-spoke monopolar

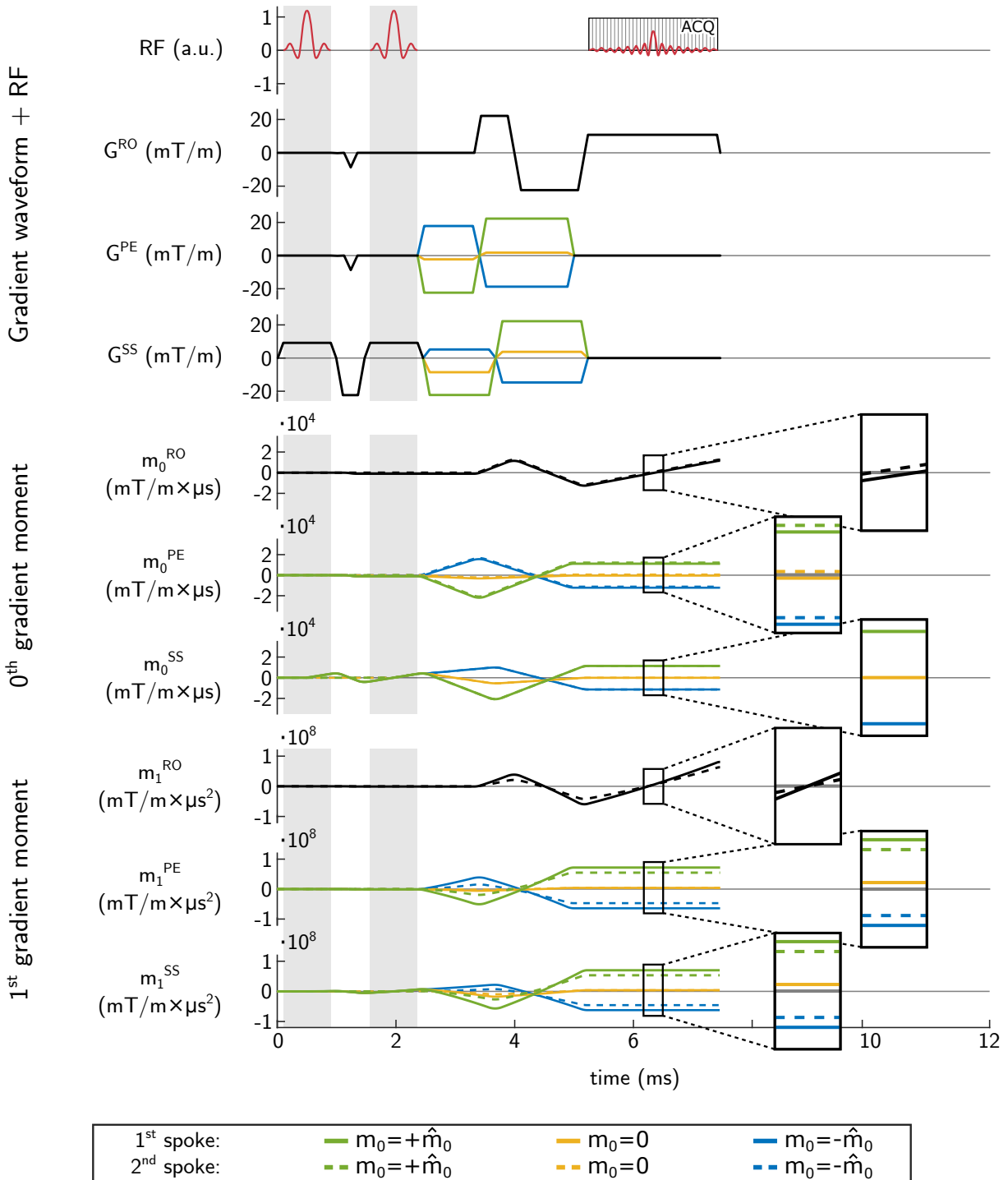


Figure 4.6: Calculated gradient waveforms and corresponding gradient moments for monopolar two-spoke excitation using encoding scheme ECHO.

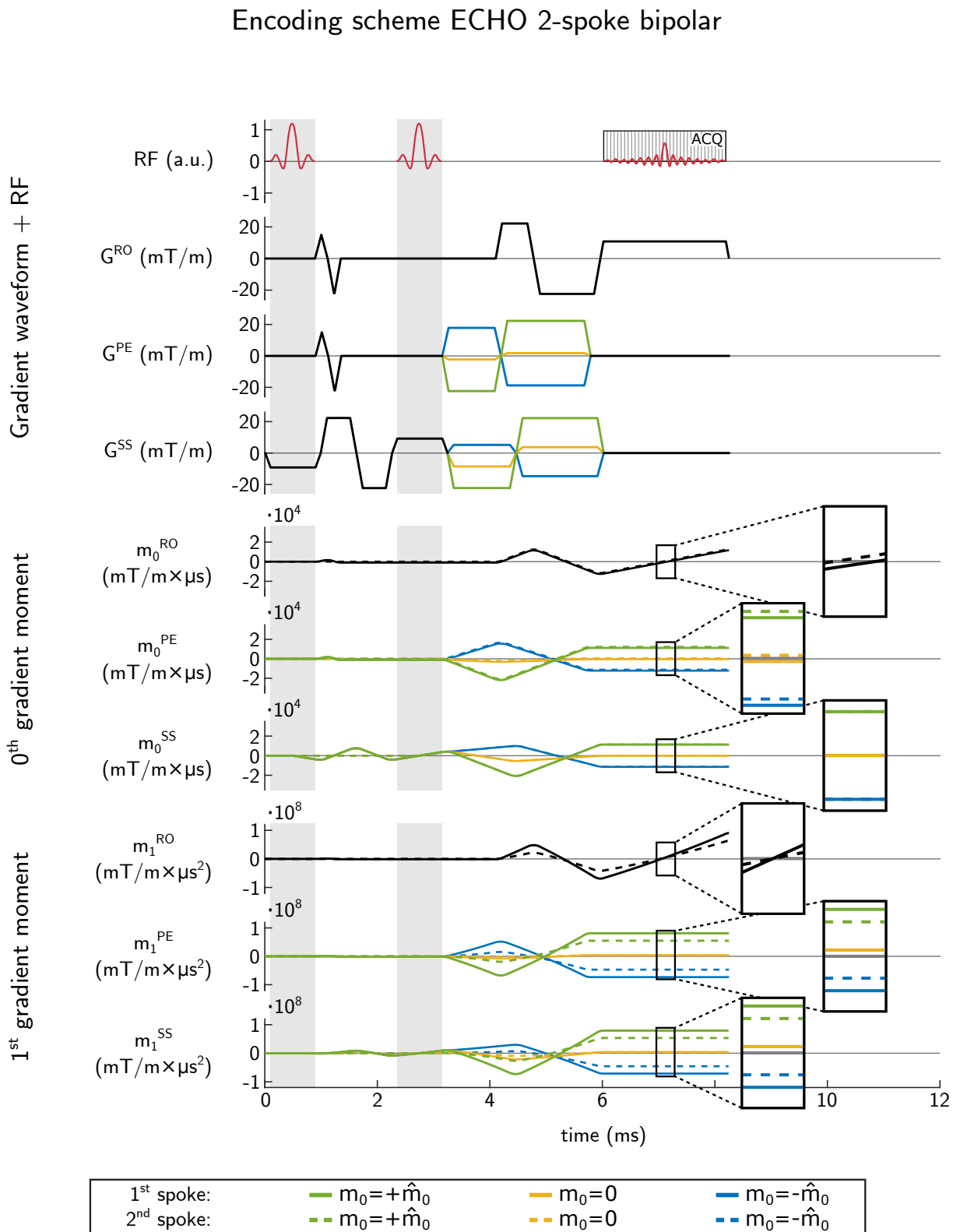


Figure 4.7: Calculated gradient waveforms and corresponding gradient moments for bipolar two-spoke excitation using encoding scheme ECHO.

Encoding scheme ISO 2-spoke monopolar

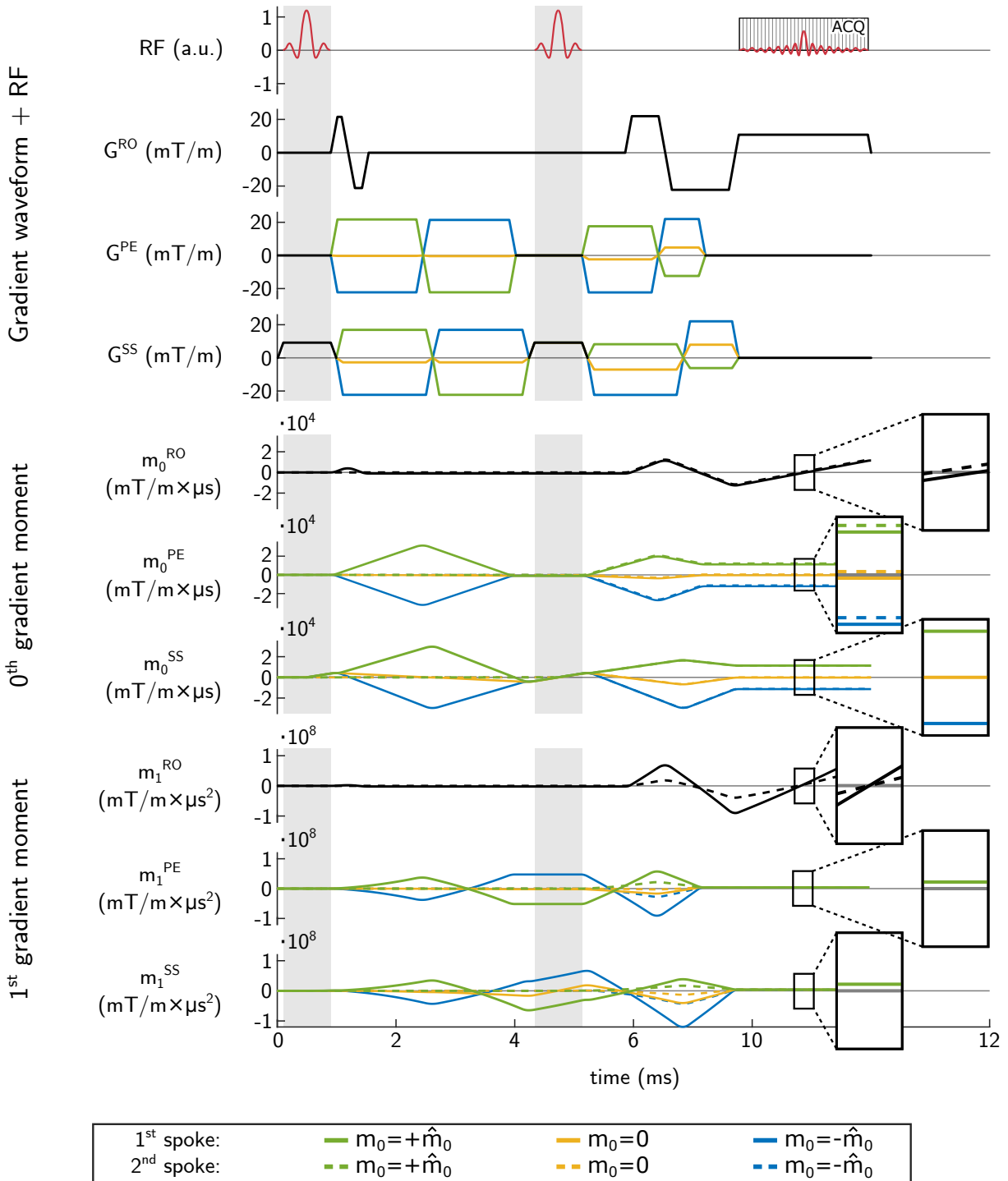


Figure 4.8: Calculated gradient waveforms and corresponding gradient moments for monopolar two-spoke excitation using encoding scheme ISO.

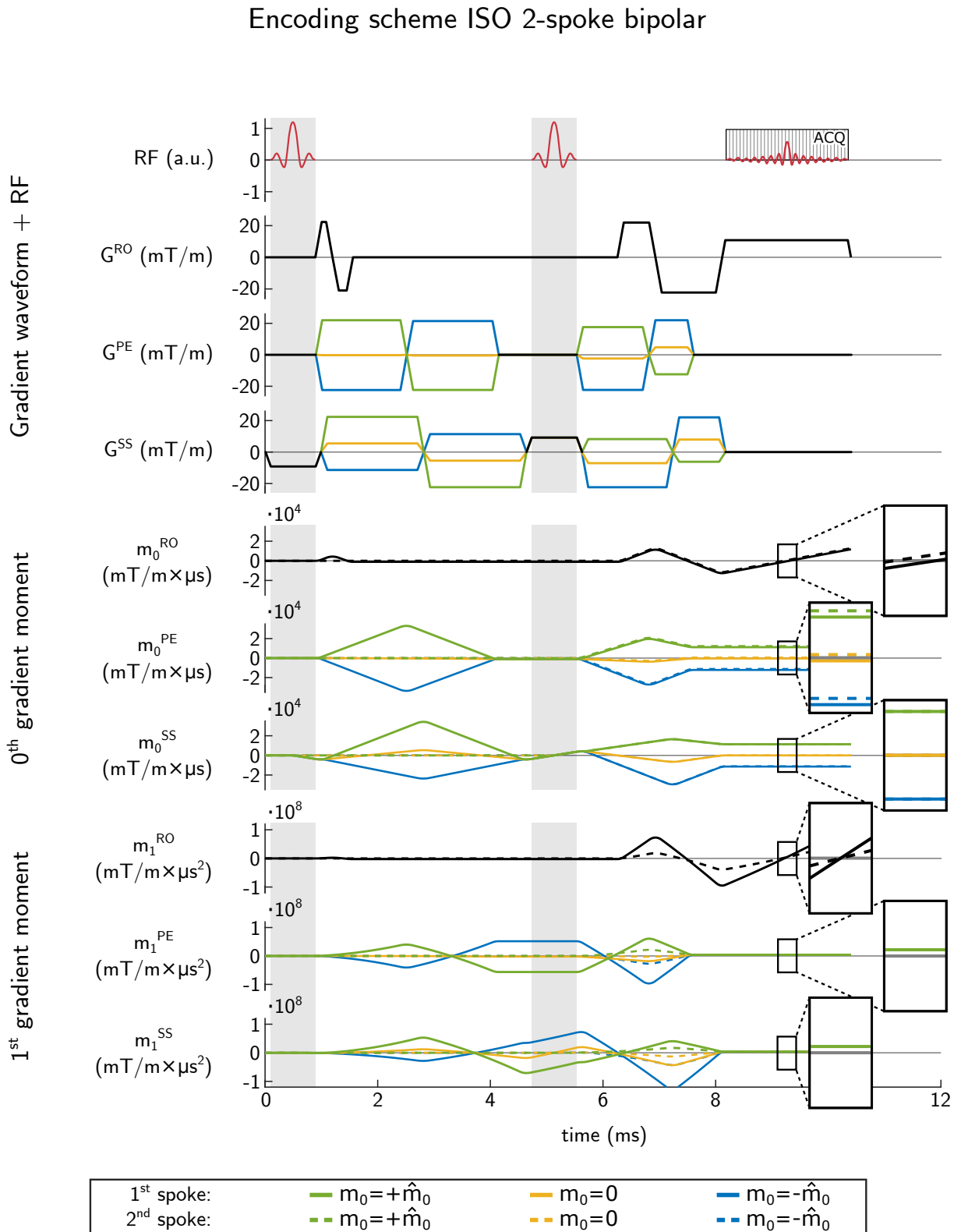


Figure 4.9: Calculated gradient waveforms and corresponding gradient moments for bipolar two-spoke excitation using encoding scheme ISO.

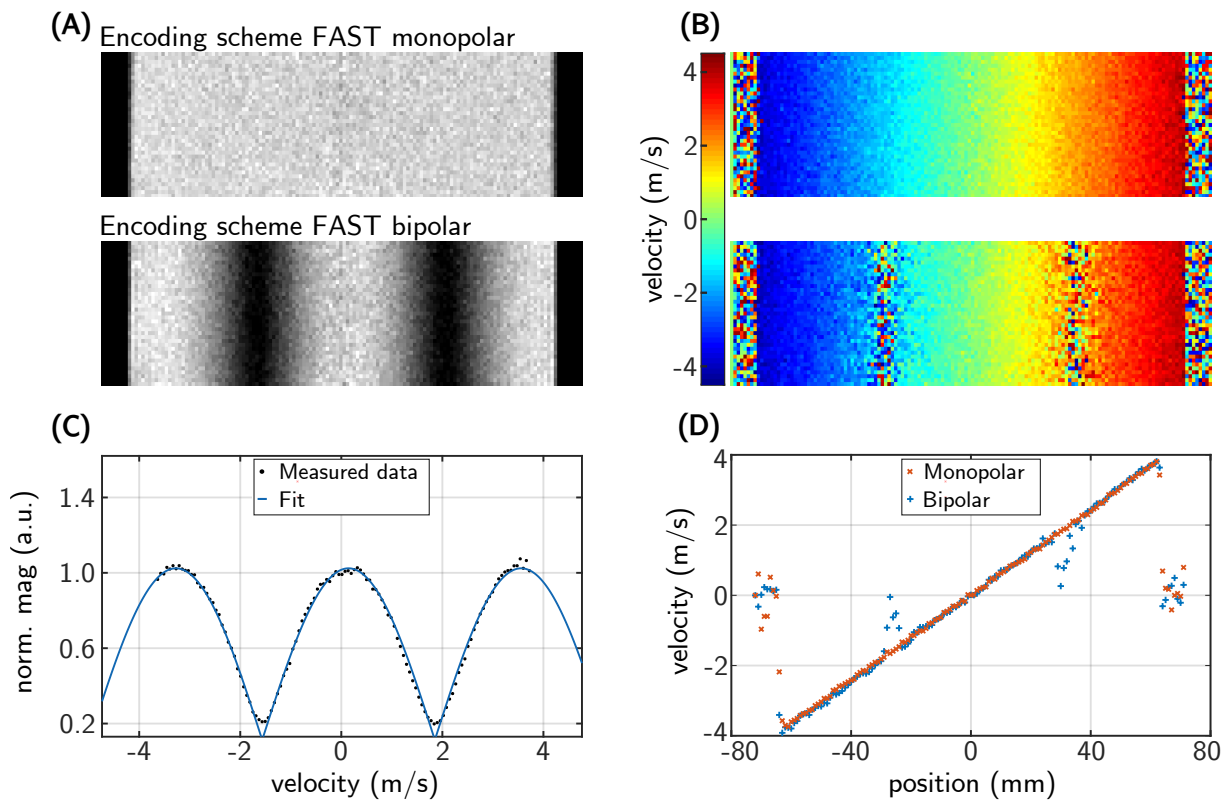


Figure 4.10: Reconstructed magnitude images (A) and velocity maps (B) of the rotation phantom for a two-spoke excitation using encoding scheme FAST in monopolar (top) and bipolar (bottom) fashion. The motion for the displayed central slice through the rotating cylinder is through-plane. (C) and (D) show corresponding line plots along the radial direction.

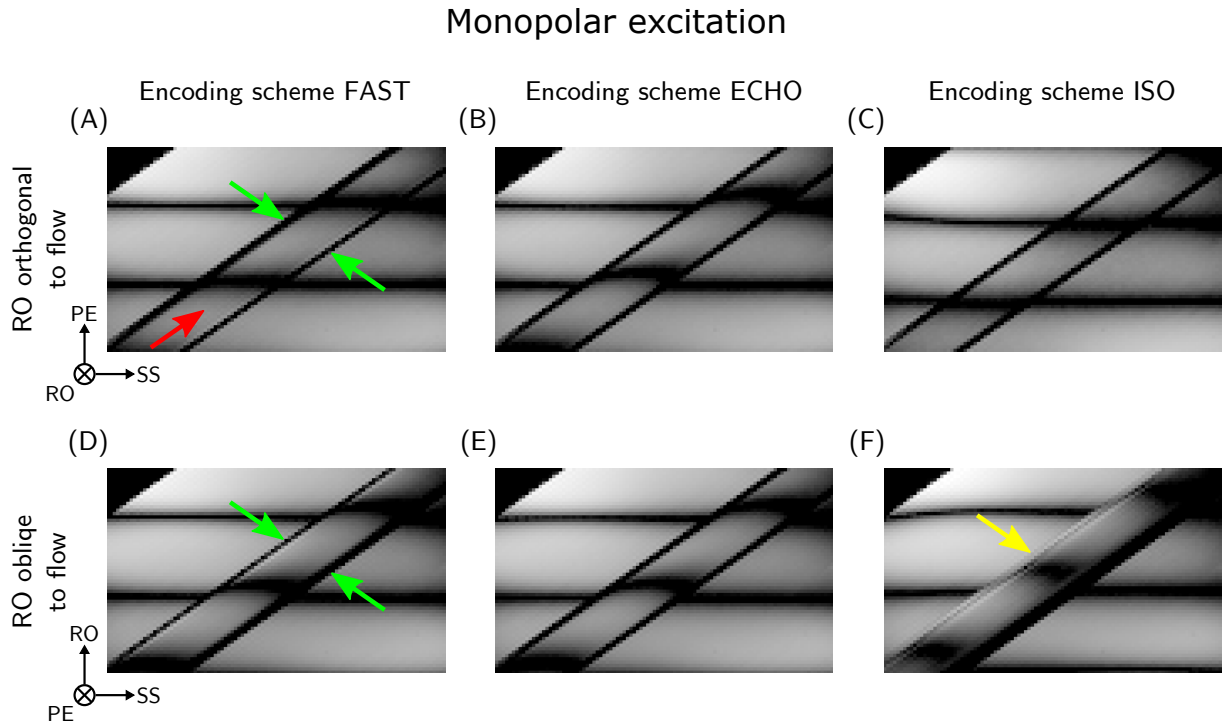


Figure 4.11: Magnitude images of the different encoding schemes using monopolar two-spoke excitation. The top and bottom row differ in their respective orientation of the imaging axes. Appropriate gradient blips were applied to create a sinusoidal tagging pattern. The direction of the flow for all measurements is indicated by the red arrow (A). Encoding scheme FAST leads to an asymmetric shape of the tube boundary (green arrows), while scheme ISO leads to signal from flowing magnetization aliasing into surrounding static tissue (yellow arrow).

Monopolar excitation

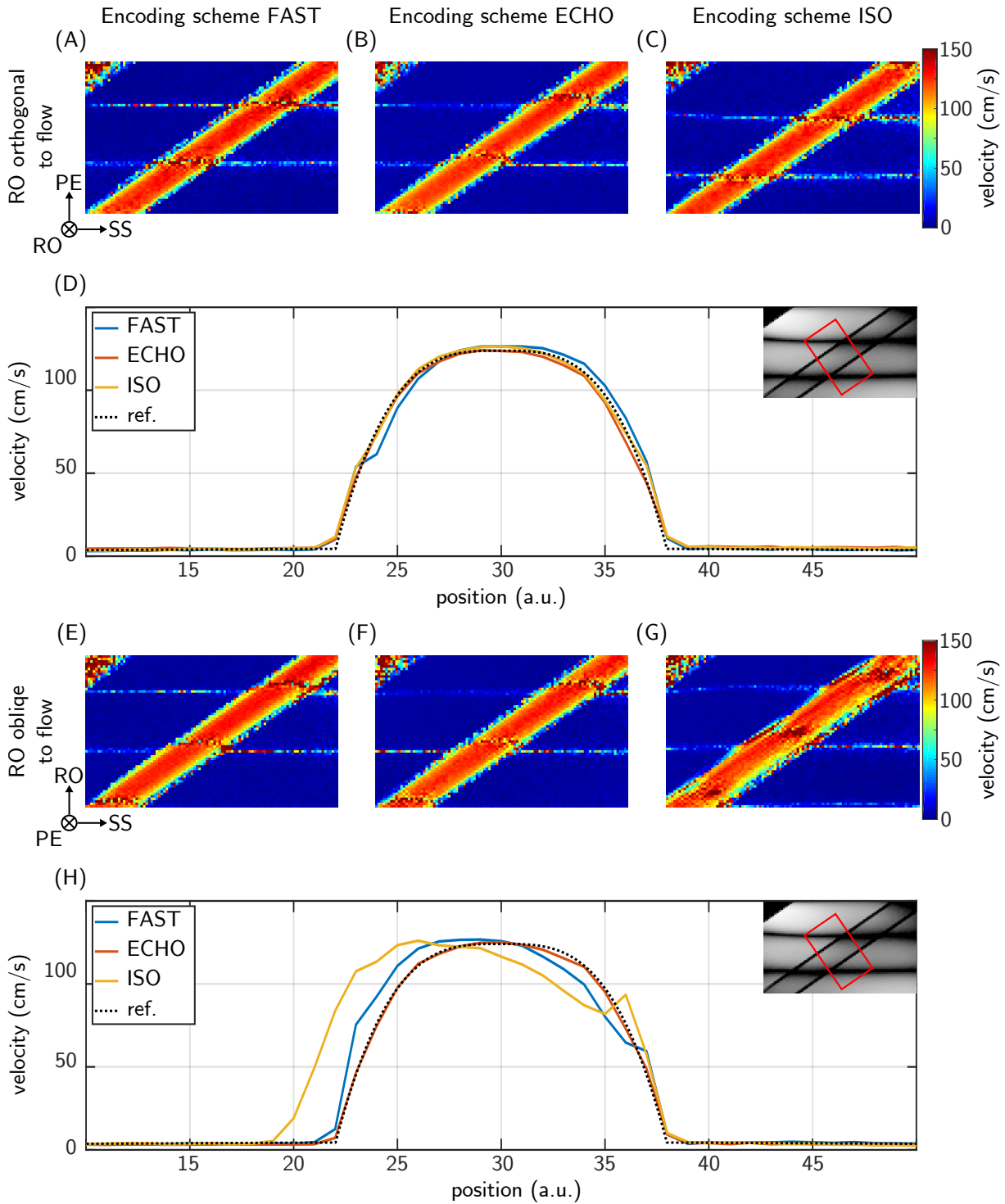


Figure 4.12: Velocity maps corresponding to the magnitude images shown in figure 4.11. For better visual comparison, a common reference profile (black dotted line) was added to the velocity profiles (D+H). The shown velocity profiles are averaged over the indicated red rectangle in D and H.

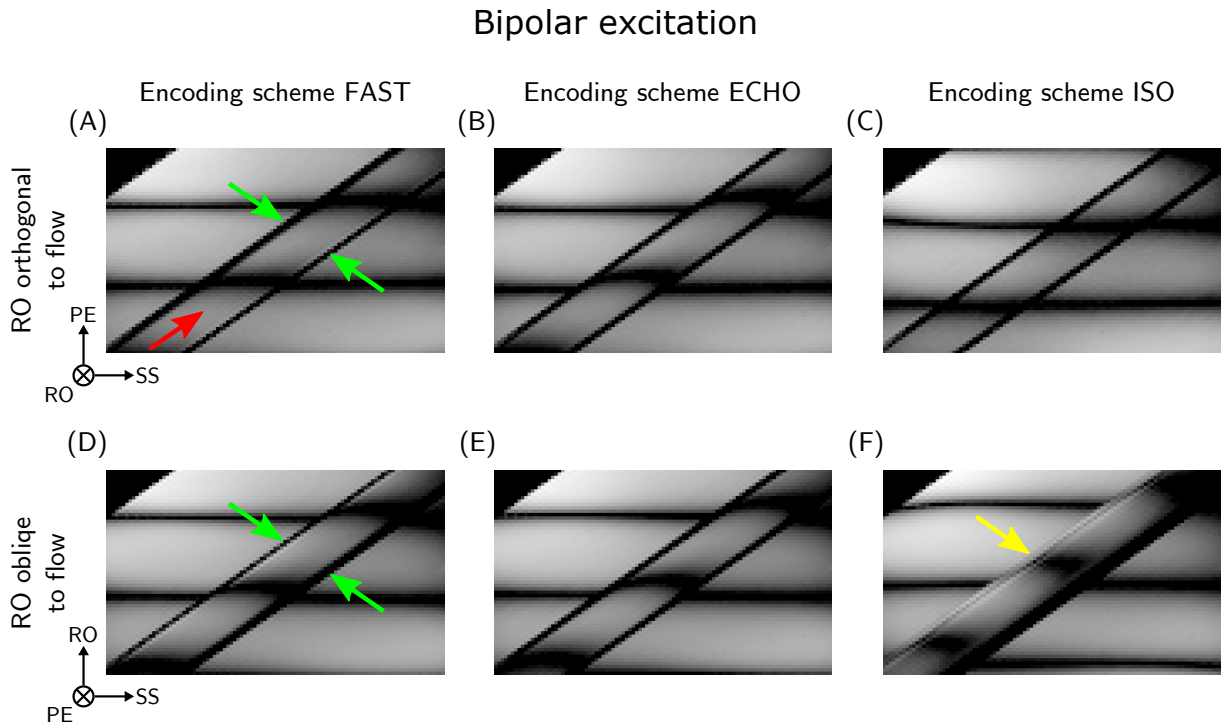


Figure 4.13: Magnitude images of the different encoding schemes using bipolar two-spoke excitation. The top and bottom row differ in their respective orientation of the imaging axes. Appropriate gradient blips were applied to create a sinusoidal tagging pattern. The direction of the flow for all measurements is indicated by the red arrow (A). Encoding scheme FAST leads to an asymmetric shape of the tube boundary (green arrows), while scheme ISO leads to signal from flowing magnetization aliasing into surrounding static tissue (yellow arrow).

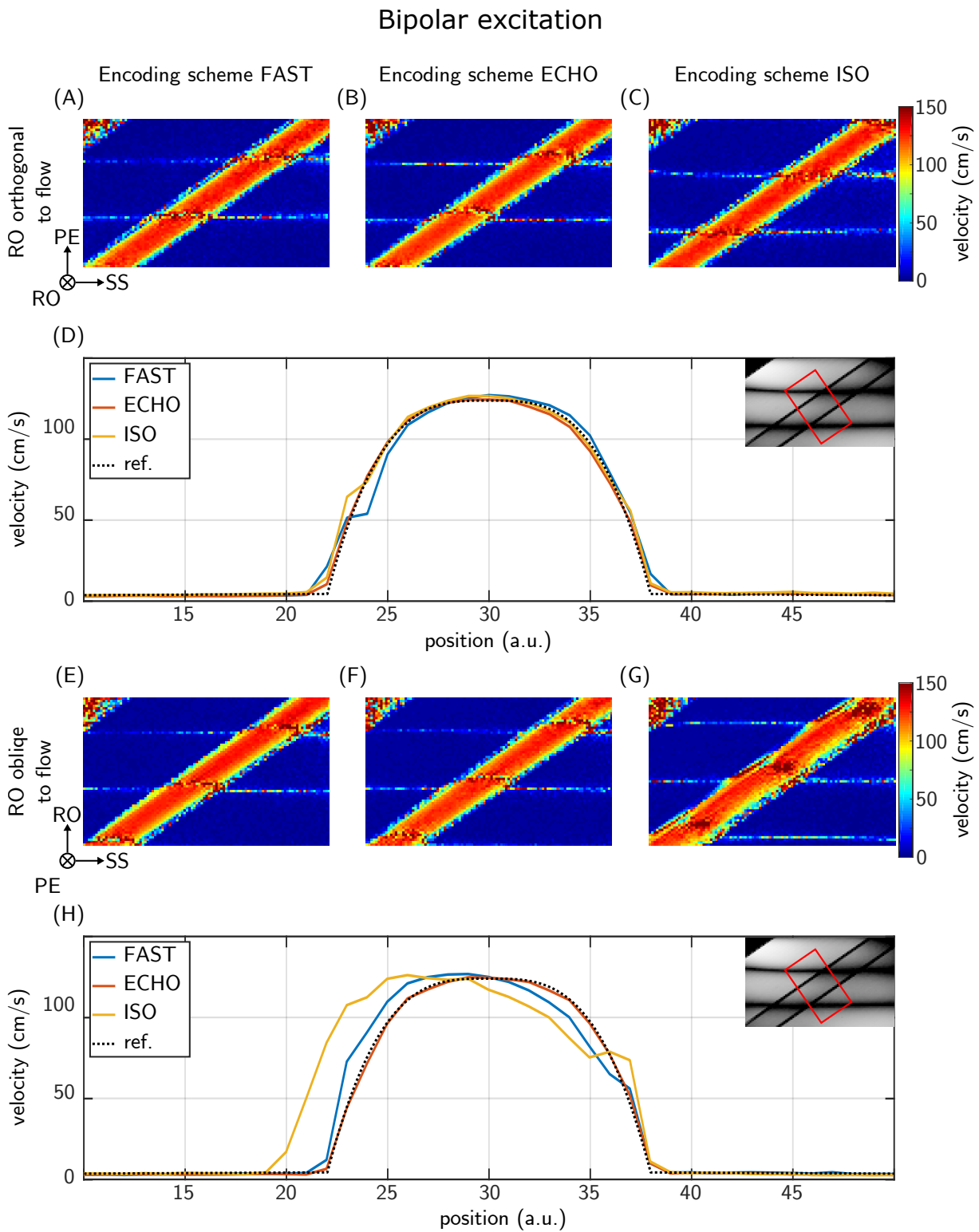


Figure 4.14: Velocity maps corresponding to the magnitude images shown in figure 4.13. For better visual comparison, a common reference profile (black dotted line) was added to the velocity profiles (D+H). The shown velocity profiles are averaged over the indicated red rectangle in D and H.

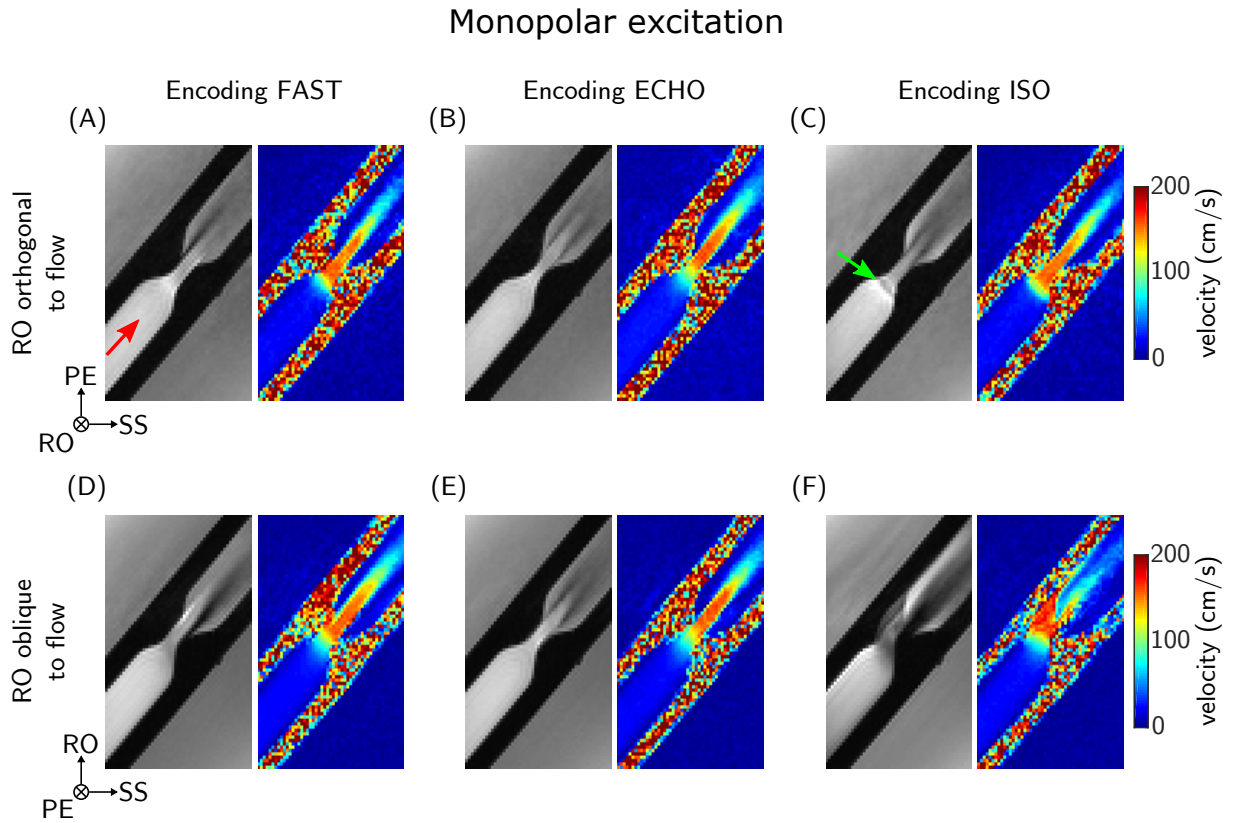


Figure 4.15: Illustration of the displacement artifact in a stenosis phantom using the three different encoding schemes and monopolar two-spoke excitation. The direction of the flow for all measurements is indicated by the red arrow (A). Scheme ISO yields a small region with altered signal intensity due to higher order of motion (green arrow).

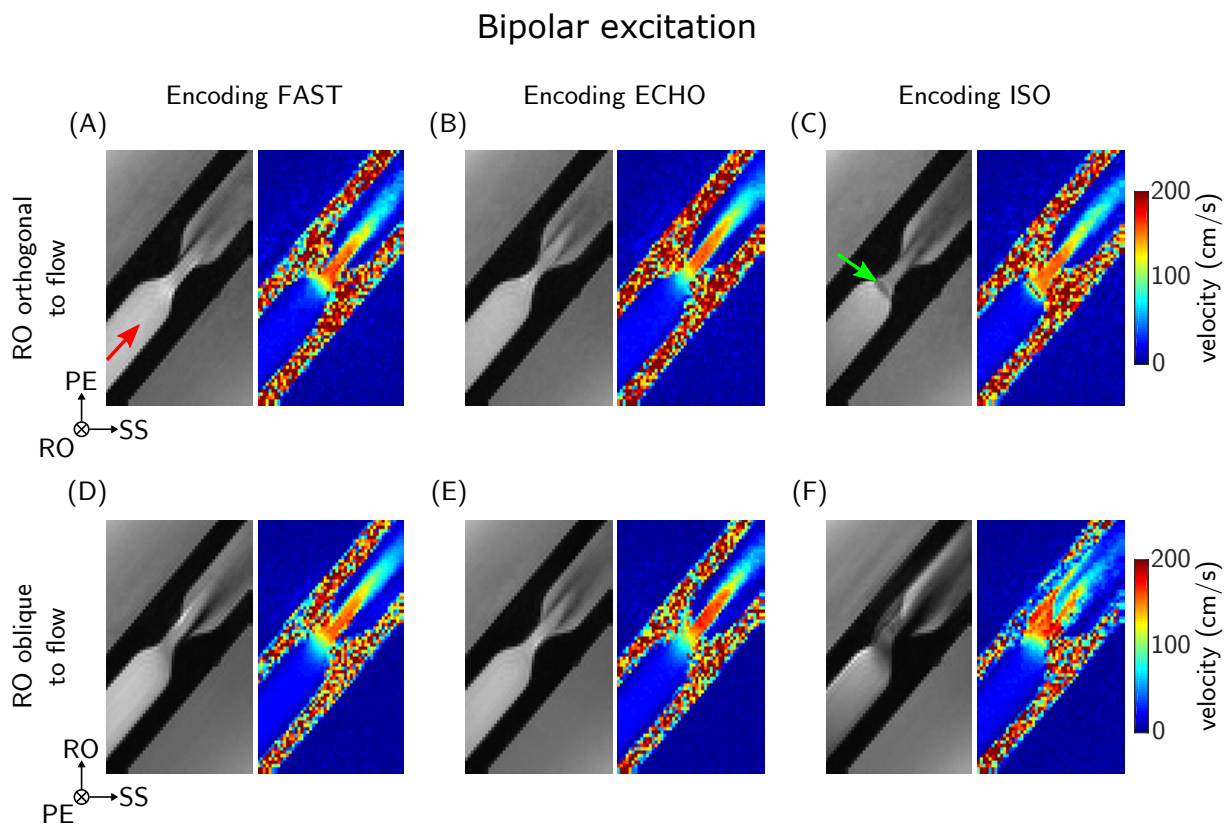


Figure 4.16: Illustration of the displacement artifact in a stenosis phantom using the three different encoding schemes and bipolar two-spoke excitation. The direction of the flow for all measurements is indicated by the red arrow (A). Scheme ISO yields a small region with altered signal intensity due to higher order of motion (green arrow).

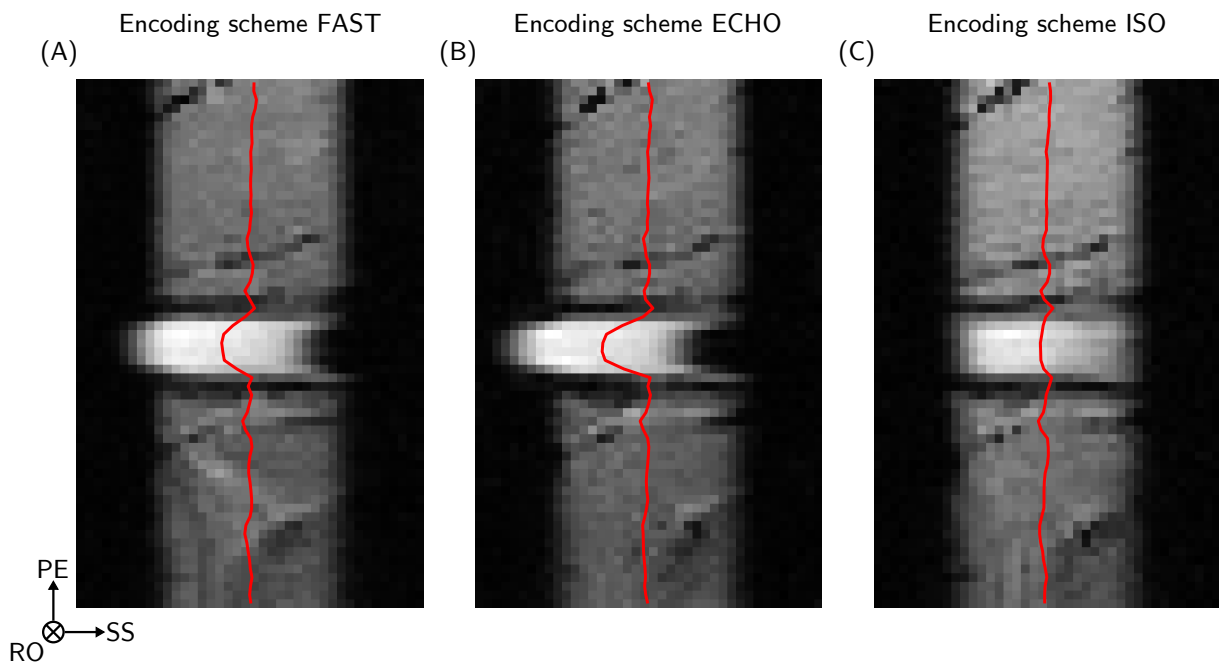


Figure 4.17: Application of the three encoding schemes to strict through-plane flow in the femoral artery of a female healthy volunteer. The center of mass along the SS direction is indicated by the red line. To resolve the displacement artifacts along the SS direction, 2-fold oversampling was applied in this direction. Otherwise the displacement artifacts would result in fold-over artifacts.

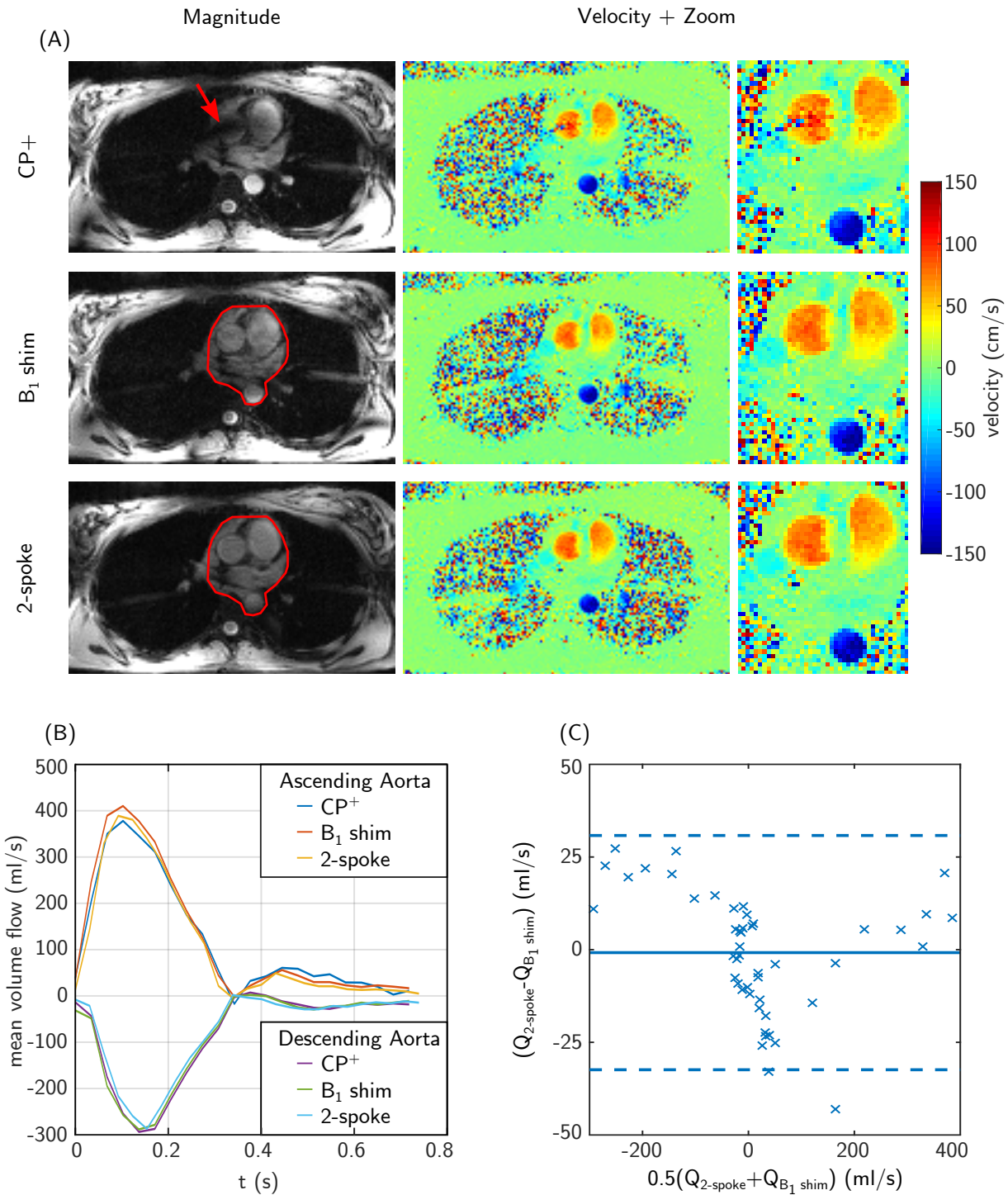


Figure 4.18: Magnitude images and velocity maps (A) in mid-systole targeting the human heart of a female healthy volunteer. Here, encoding scheme ECHO was used in combination with three different excitation methods. The ROIs used for optimization of the B_1 phase shim and the two-spoke excitation are marked in red. For quantitative comparison between B_1 phase shimming and the two-spoke excitation, mean volume flow of the ascending and descending aorta over the cardiac cycle (B) and a corresponding BLAND-ATMAN plot (C) are shown. The solid line of the latter indicates the mean value of 0.8 mL/s and the dashed lines mark the 95% confidence interval.

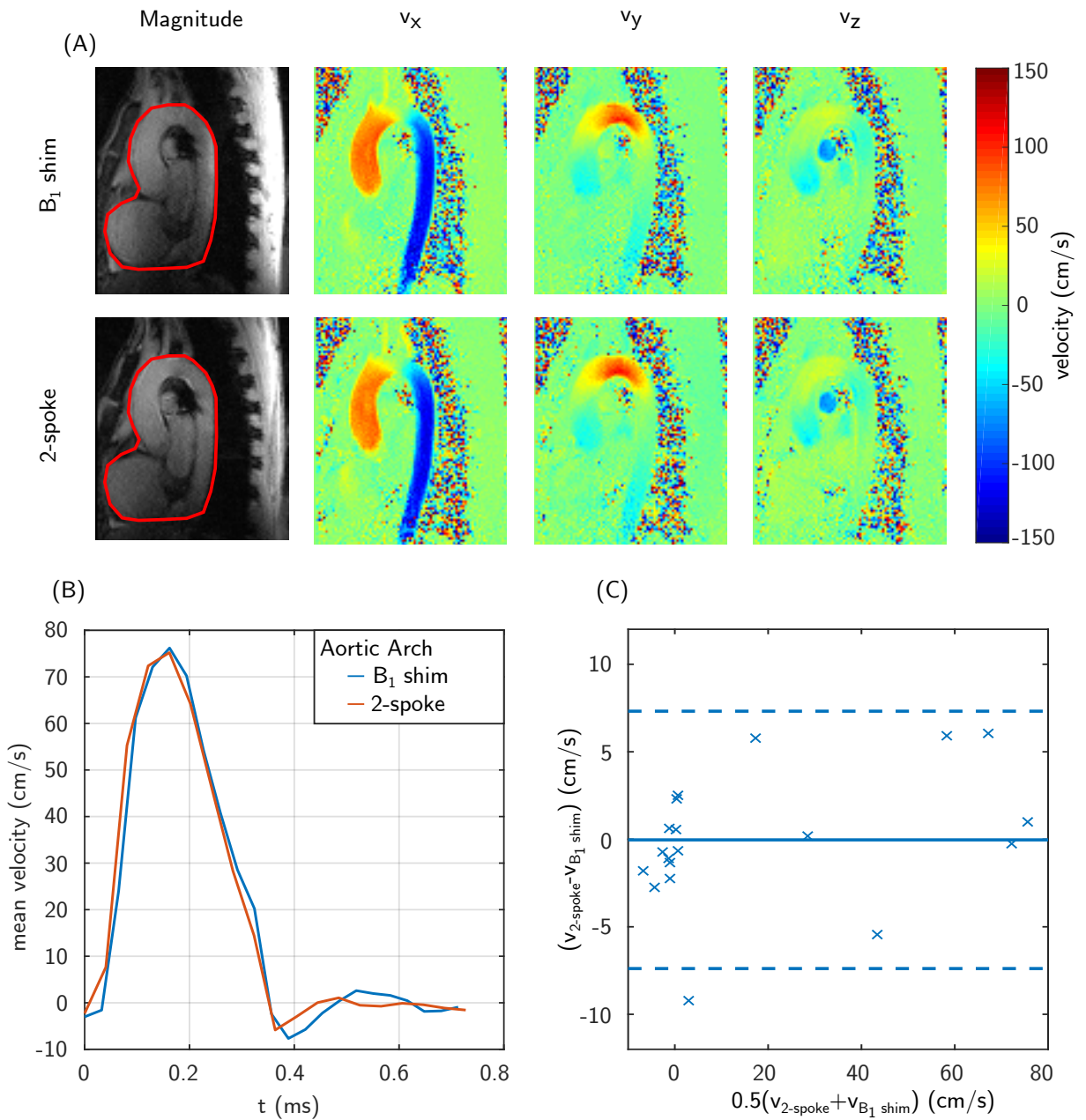


Figure 4.19: Three directional velocity quantification, targeting the human aorta. Magnitude images and maps of the three velocity vector components (A) are shown for encoding scheme ECHO in combination with two different excitation methods. The ROIs used for optimization of the B_1 phase shim and the two-spoke excitation are marked in red. Mean velocities in the aortic arch over the cardiac cycle (B) with corresponding BLAND-ALTMAN plot (C) illustrate differences between the different excitation methods. The solid line of the latter indicates the mean value of 0.0 cm/s and the dashed lines mark the 95% confidence interval.

4.2 Velocity encoded and compensated asymmetric multi-spoke RF pulses

4.2.1 Simulations

Prior to the phantom and in vivo measurements employing asymmetric multi-spoke RF pulses, simulations were performed to characterize their performance. The waveforms of the symmetric sinc-shaped and the asymmetric pulse are illustrated in figure 4.20A. The corresponding slice profiles of a single-spoke excitation are shown in figure 4.20B for the case of static magnetization. The asymmetric pulse leads to a non-zero imaginary part of the slice profile, which leads to a signal reduction of 6% due to through-slice dephasing for a 2D acquisition. The magnitude of the slice profiles match between the symmetric and asymmetric RF pulse. If applied in a two-spoke fashion, with the second asymmetric pulse being reflected (figure 4.24A), the imaginary part in the slice profile is eliminated in the absence of flow (figure 4.20C). In reality, however, the two RF pulses do not necessarily have the same amplitude, which leads to a residual imaginary part (figure 4.20D) that depends on the relative scaling of the two asymmetric pulses' amplitudes.

Figure 4.21-4.24 show the results of the simulated slice profiles for single- and two-spoke excitation for both symmetric and asymmetric RF pulses. The investigated velocities in slice select direction cover a range of -5.0 m/s to 5.0 m/s. For physiologically relevant velocities (approximately -2.0 m/s to 2.0 m/s), the slice profiles resulting from the single-spoke excitations appear unaffected for both, symmetric and asymmetric, RF pulses (figure 4.21 and 4.22). The same holds true for the two-spoke case with symmetric RF pulses (figure 4.23). For the asymmetric two-spoke excitation, however, the non-stationary magnetization leads to a non-zero imaginary part of the slice profile, even if both asymmetric RF pulses are scaled identically of up to 6% of the real part (figure 4.24). By using asymmetric RF pulses, the inter-spoke duration ΔTE could be reduced from 1.3 ms to 0.6 ms.

4.2.2 Phantom measurements

To validate the simulated slice profiles, the straight flow phantom was used in a phantom experiment. The slice profiles of single and two-spoke excitation with both, symmetric and asymmetric, RF pulses were evaluated in three different ROIs (figure 4.26A). These covered static tissue, one tube with a mean velocity of 95 cm/s, and a second tube with a mean velocity of -55 cm/s. All measured slice profiles (figure 4.25) support the simulation results. Here, the inter-spoke duration could be decreased from 1.4 ms to 1.0 ms.

Furthermore, the through-plane velocity was quantified in the three ROIs for all four excitation schemes and corresponding results are displayed in figure 4.26. The maximum deviations between the mean velocities obtained with the four different excitation schemes for the three ROIs are 0.1 cm/s, 0.7 cm/s, and 0.3 cm/s for the static ROI (figure 4.26B), the small tube (figure 4.26C), and the big tube (figure 4.26D), respectively.

4.2.3 In vivo measurements

In vivo results of two-spoke excitation with symmetric as well as asymmetric RF pulses are shown in figure 4.27, acquired in a healthy female volunteer with encoding scheme ECHO. Both excitations were optimized for flip angle homogeneity within an ROI covering the whole heart. Through-plane velocity maps in mid-systole, displayed in figure 4.27B+C, agree qualitatively, as well as time-resolved mean velocities in the ascending and descending aorta (figure 4.28A). A quantitative comparison (BLAND-ALTMAN plot in figure 4.28B) yields a mean difference of the mean velocities throughout the cardiac cycle of -1.4 cm/s with a standard deviation of 5.5 cm/s. Furthermore, the relative differences in peak velocity in the ascending and descending aorta were 9% and 2%, respectively. The use of asymmetric RF pulses reduced the inter-spoke duration from 2.8 ms to 1.4 ms, while improving the temporal resolution from 39.1 ms to 33.9 ms (13.3% reduction).

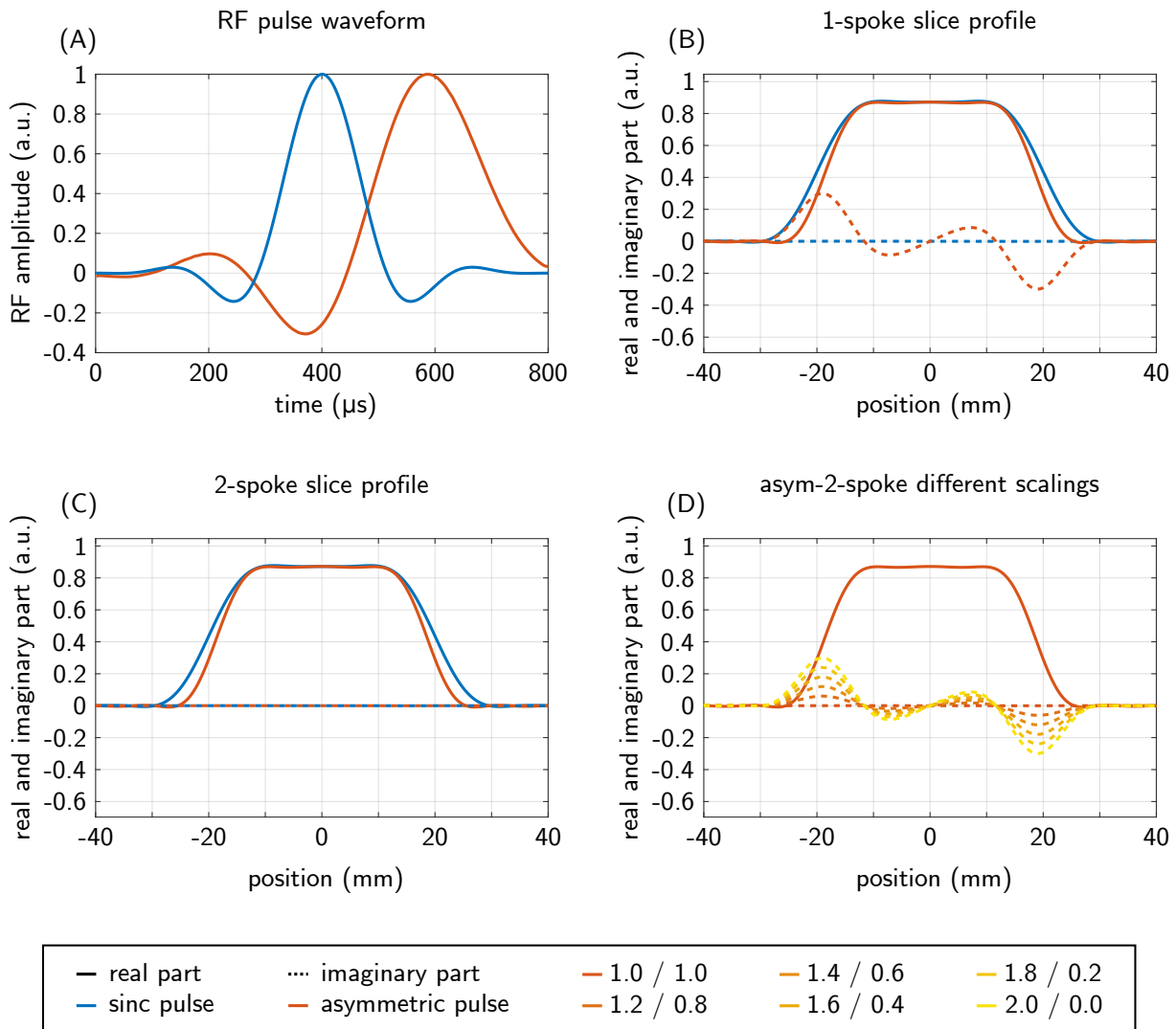


Figure 4.20: RF waveform (A) of the sinc and the asymmetric RF pulse with corresponding slice profiles of a single-spoke (B) and two-spoke (C) excitation. If the amplitudes of the two asymmetric RF pulses are not equal, the resulting slice profile shows a non-zero imaginary part (D).

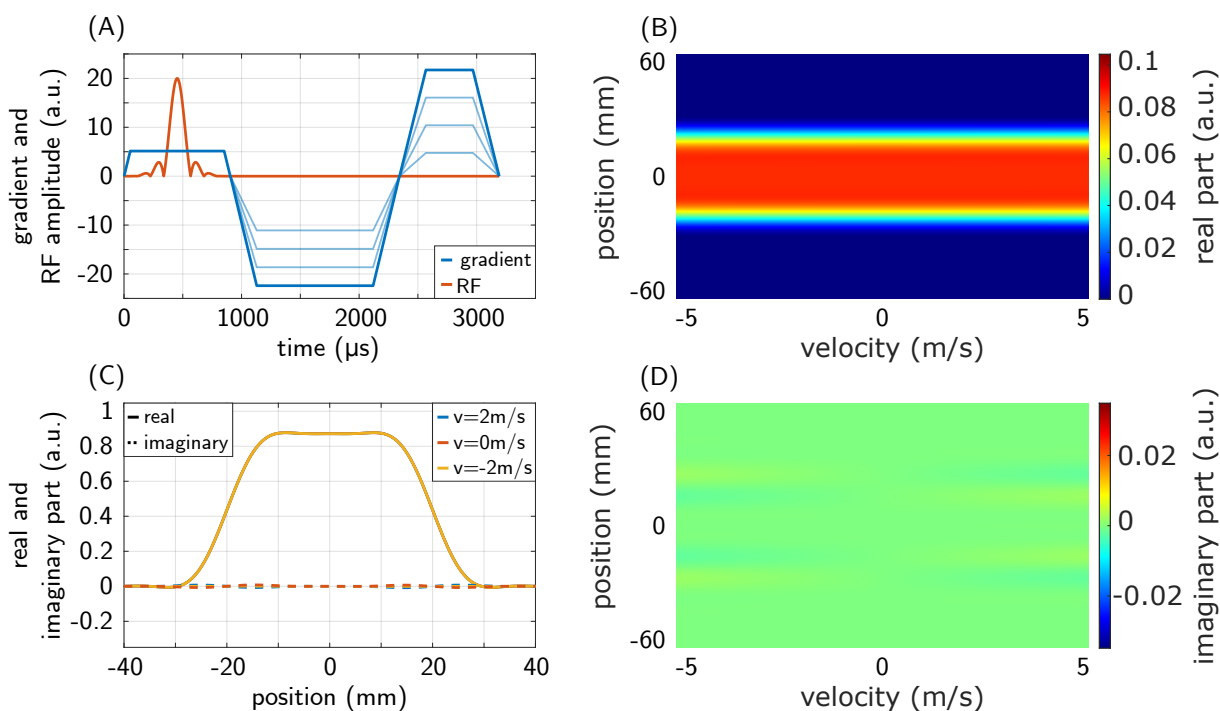


Figure 4.21: RF and gradient waveform (A) of a single-spoke excitation using a sinc-shaped RF pulse. Simulations of the slice profile were performed for a velocity range of -5 m/s to 5 m/s (B+D). Example slice profiles are shown in (C).

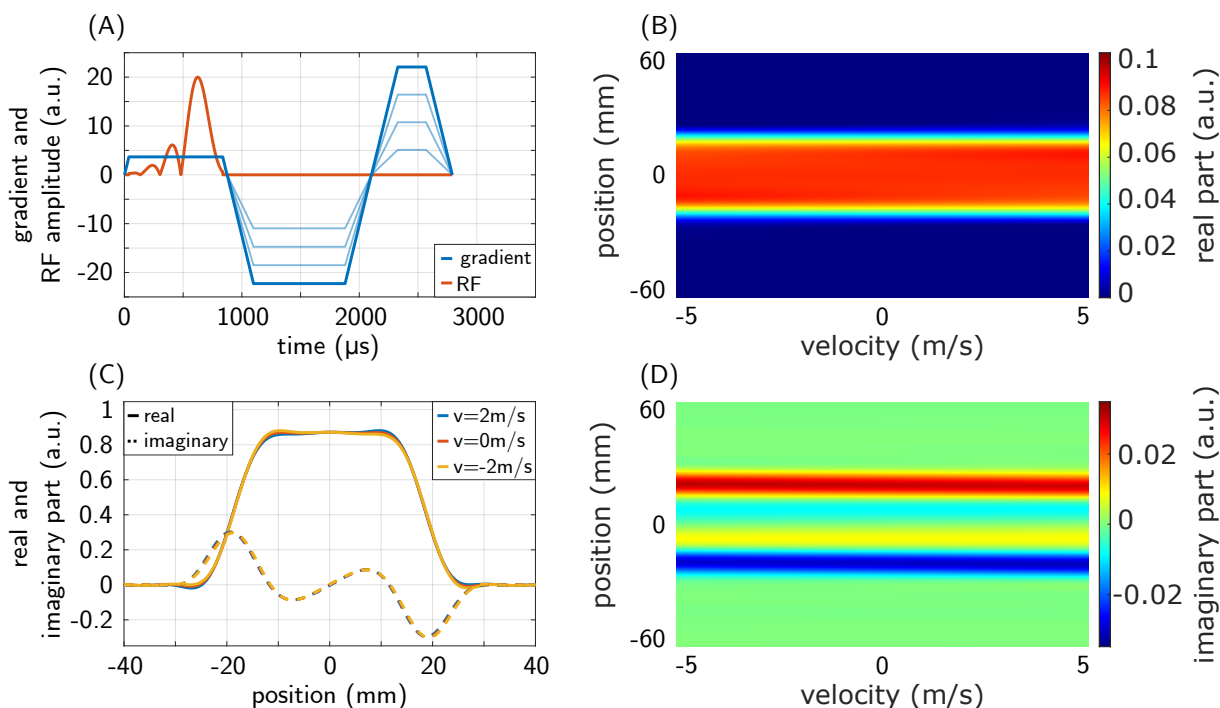


Figure 4.22: RF and gradient waveform (A) of a single-spoke excitation using an asymmetric RF pulse. Simulations of the slice profile were performed for a velocity range of -5 m/s to 5 m/s (B+D). Example slice profiles are shown in (C).

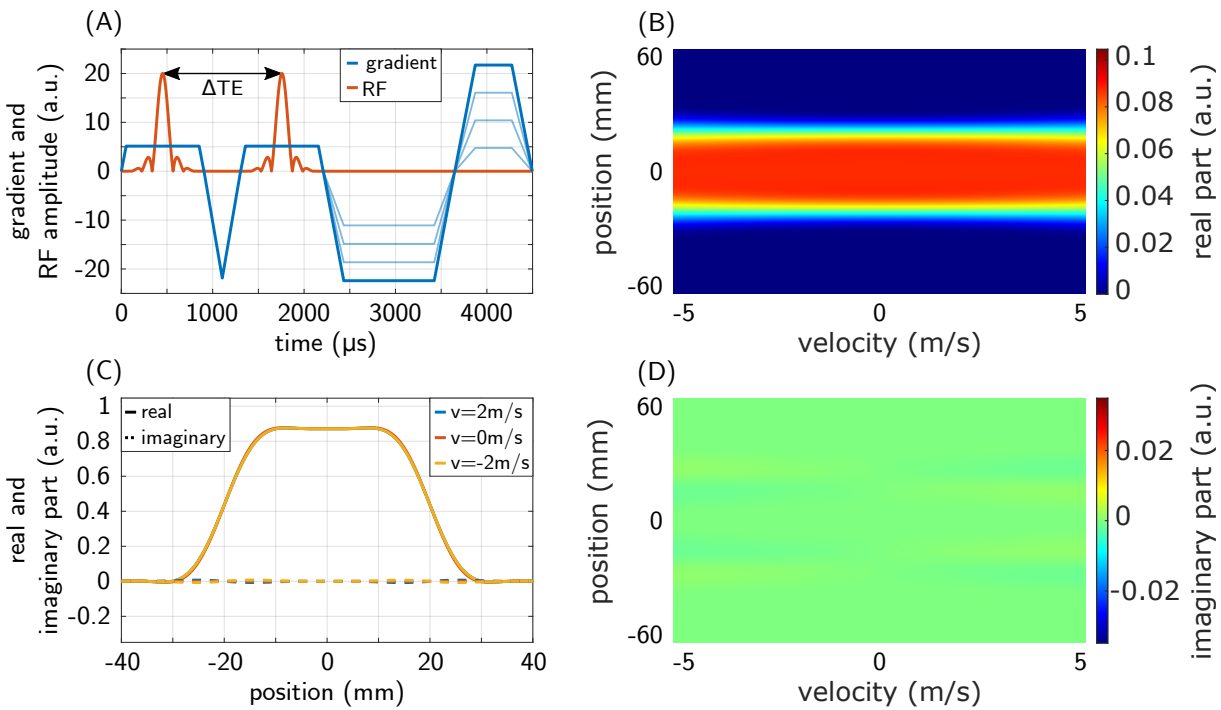


Figure 4.23: RF and gradient waveform (A) of a two-spoke excitation using sinc-shaped RF pulses. Simulations of the slice profile were performed for a velocity range of -5 m/s to 5 m/s (B+D). Example slice profiles are shown in (C).

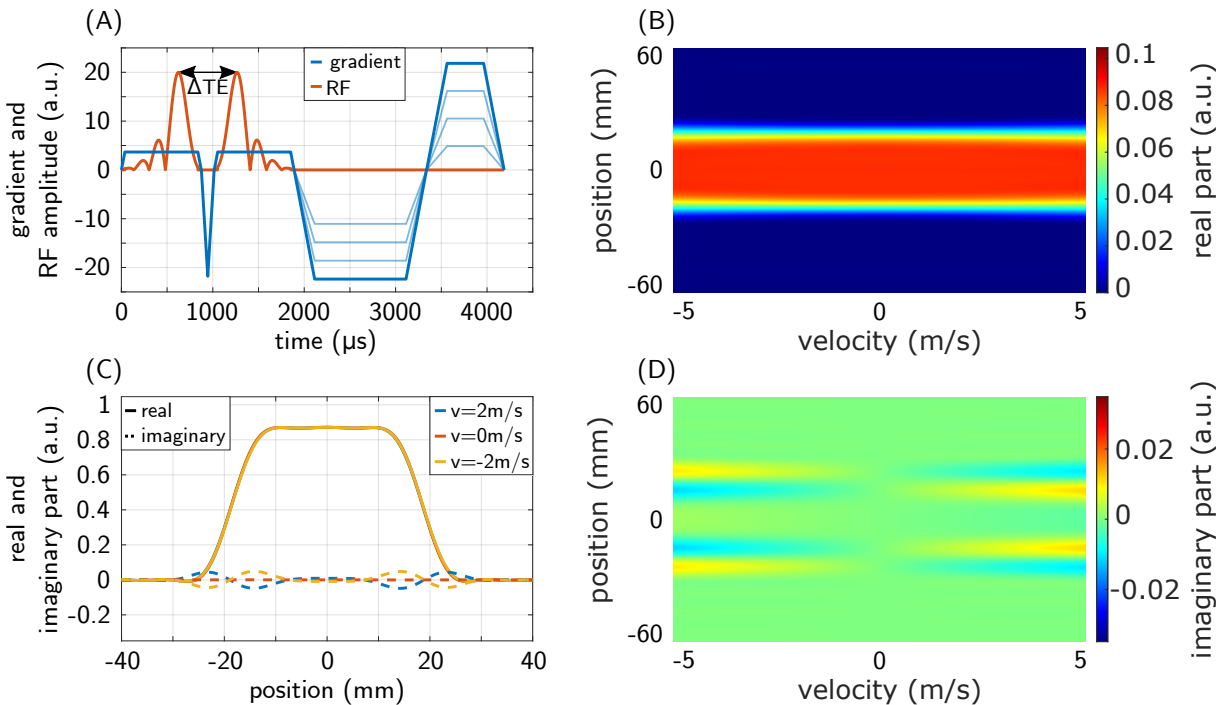


Figure 4.24: RF and gradient waveform (A) of a two-spoke excitation using asymmetric RF pulses. Simulations of the slice profile were performed for a velocity range of -5 m/s to 5 m/s (B+D). Example slice profiles are shown in (C).

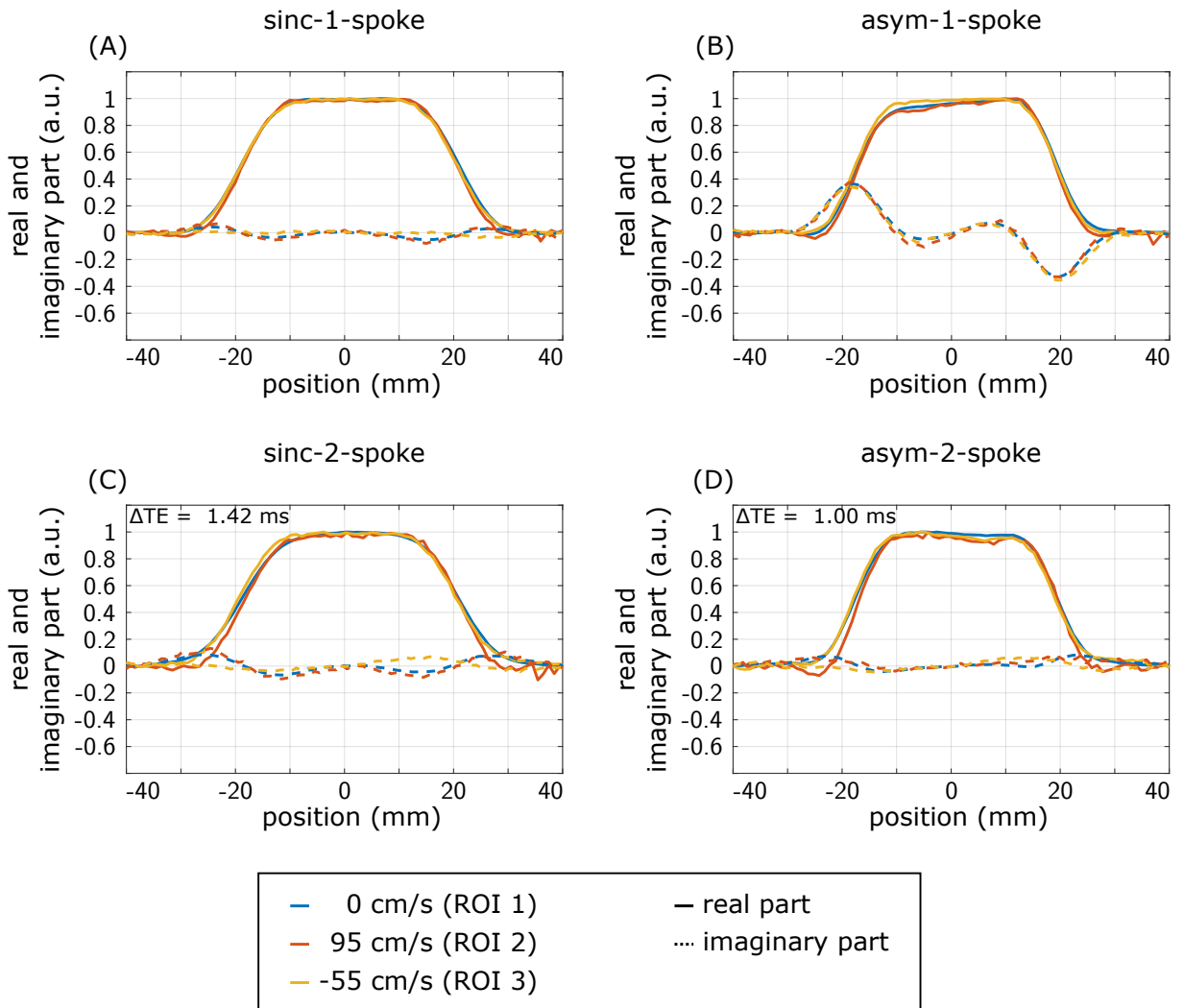


Figure 4.25: Measured slice profiles, which correspond to the simulation results of the different excitations shown in figure 4.21-4.24.

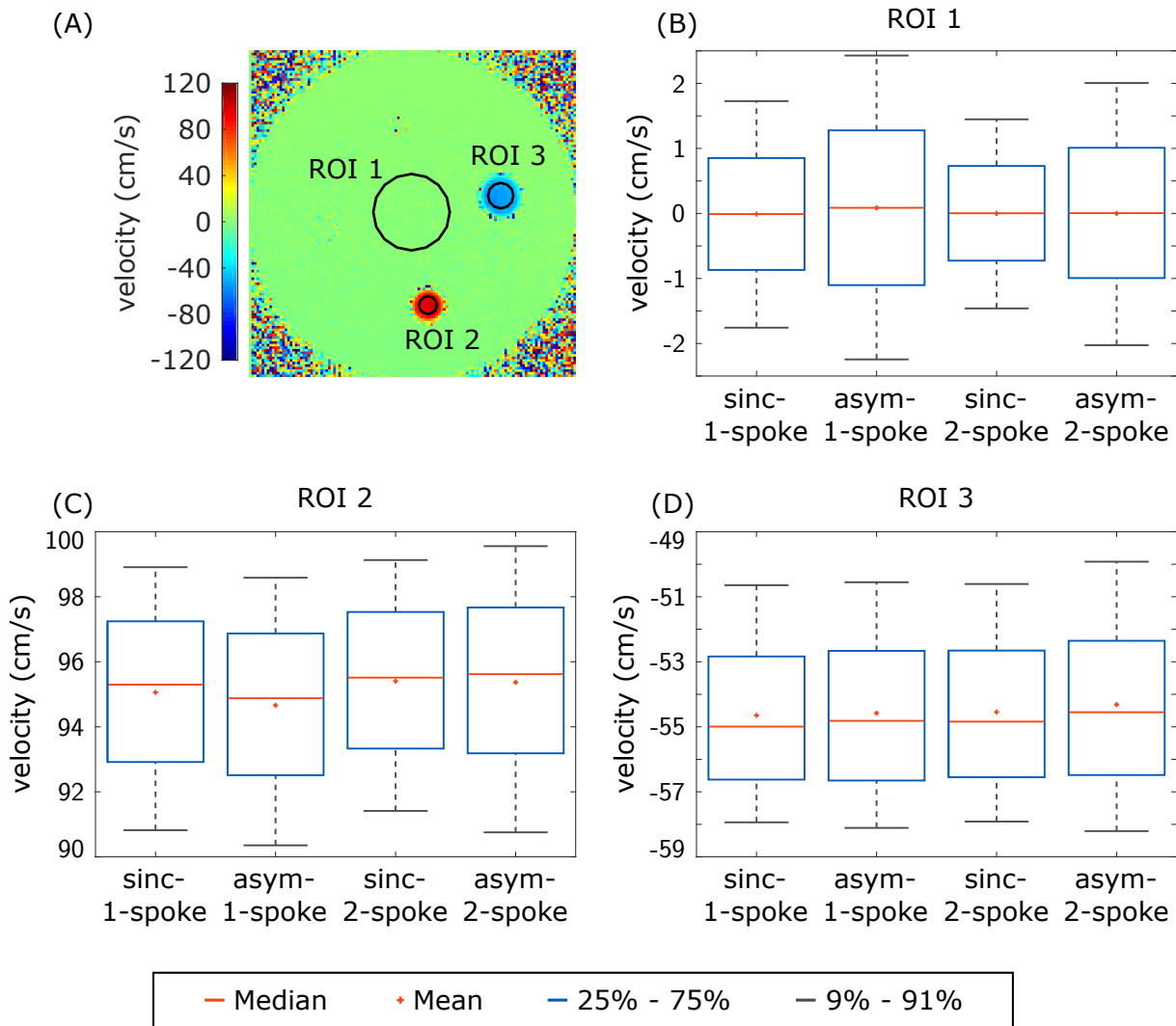


Figure 4.26: Velocity quantification in the straight flow phantom with sinc-shaped and asymmetric RF pulses, for both, single- and 2-spoke, excitation. The three ROIs used for statistical analysis are shown in the example velocity map (A). Resulting box plots are shown for all ROIs and all excitation schemes (B-D).

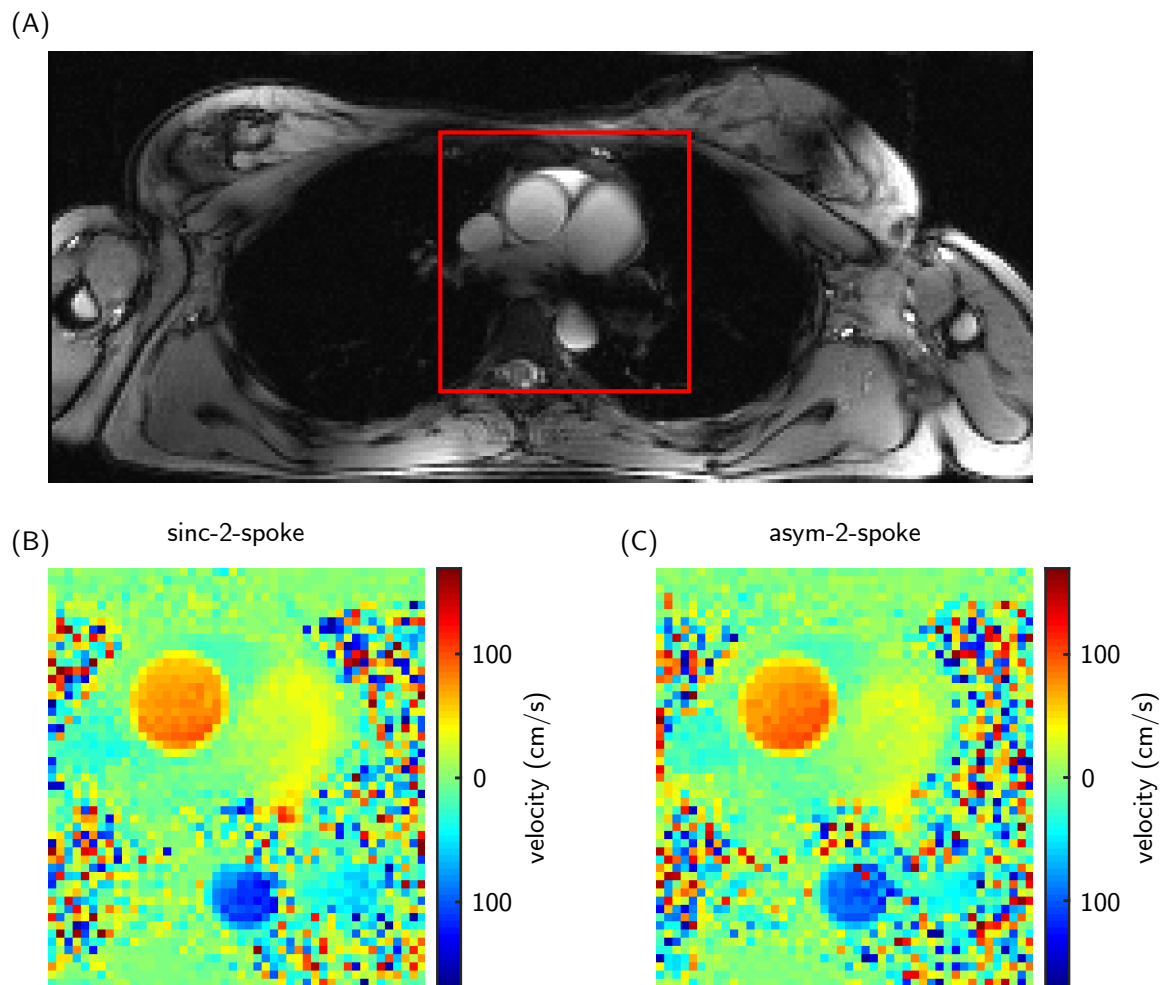


Figure 4.27: Comparison of in vivo flow quantification with two-spoke excitation using sinc-shaped and asymmetric RF pulses. The red rectangle in the magnitude image (A) indicates the image portions of the through-plane velocity maps shown in B+C. A quantitative comparison over the cardiac cycle can be seen in figure 4.28.

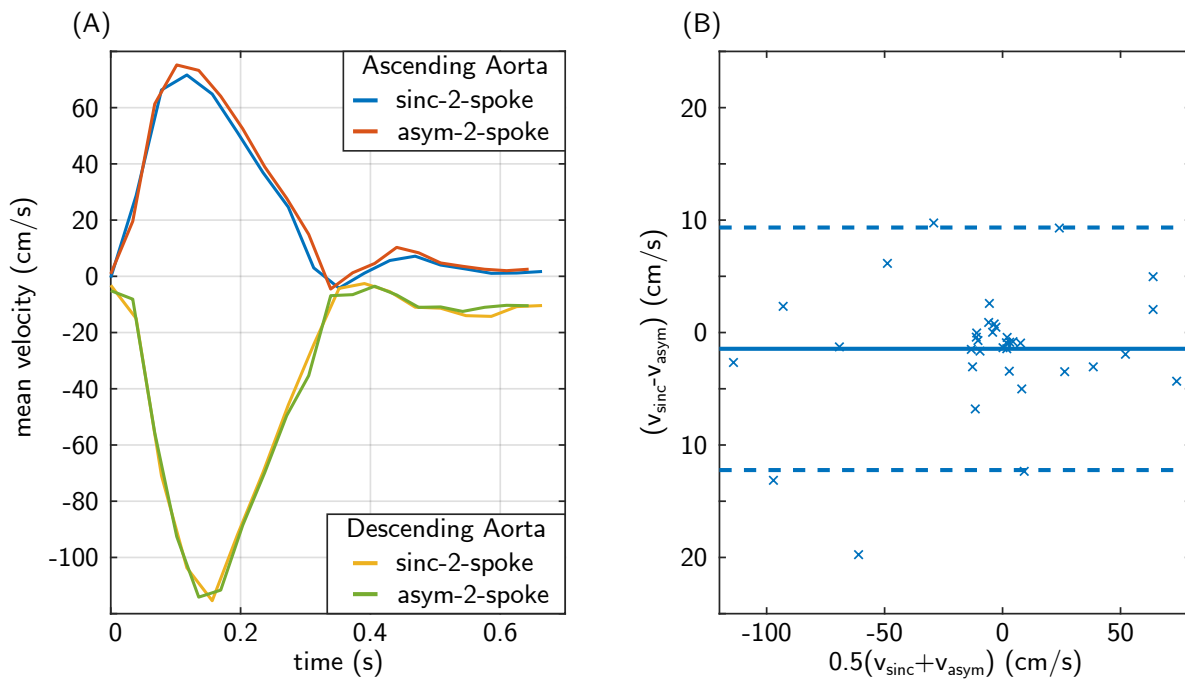


Figure 4.28: Mean velocity in the ascending and descending aorta over the cardiac cycle (A) acquired with sinc-shaped and asymmetric 2-spoke RF pulses. A quantitative comparison can be seen in the corresponding Bland-Altman plot (B). The solid line indicates the mean value of -1.4 cm/s and the dashed lines mark the 95% confidence interval.

4.3 Impact of the displacement artifact on wall shear stress quantification

4.3.1 Phantom measurements

As shown in the previous subsections, the encoding scheme has a substantial impact on the quantified velocity vector field. To evaluate the propagation of these influences on the estimation of WSS, phantom measurements were conducted in a simplified model of an aortic stenosis (c.f. figure 3.9). For each measurement, an individual mask of the flowing region was segmented based on magnitude thresholding, leading to individual geometries.

Figure 4.29 shows the velocity vector field acquired with the SYNC SPI sequence that is regarded as a gold standard here (c.f. subsection 3.2.3). The black contour illustrates the true geometry of the phantom and the velocity vector field is shown for every voxel within the mask based on the magnitude image. The SYNC SPI acquisition does not lead to any visible displacement artifacts, as can be seen by the good agreement of the illustrated velocity vectors with the real phantom geometry in figure 4.29. As expected, the maximum velocity is also measured at the location of the smallest diameter within the stenosis. Due to the fact that all encoding directions are equivalent for the SYNC SPI sequence, only a single orientation of the imaging axes was acquired.

In contrast to the SYNC SPI, two acquisitions were performed with swapped RO and PE axes for the encoding schemes ECHO and FAST (figure 4.30 and 4.31). For encoding scheme ECHO no significant differences are observed by exchanging the orientation of the imaging axes. The spatial encoding time points are synchronized, leading to a displacement along the velocity vector, which minimizes displacement artifacts. However, because the velocity encoding time points are not synchronized with the spatial encoding time points, the quantified velocity vector field is prone to artifacts due to acceleration and higher time derivatives. This effect becomes apparent at the stenosis in figure 4.30. The quantified velocities are shifted downstream, leading to the maximum velocity being detected downstream of the stenosis.

Because the spatial encoding time points along the RO and PE axes are not synchronized for encoding scheme FAST, a dependency of the displacement artifact on the orientation of these axes can be observed, as shown in figure 4.31. This is most obvious at the point, at which the high velocity jet hits the boundary of the phantom (figure 4.31B). Depending on the orientation of the imaging axes, the phantom geometry is distorted either outwards or inwards. With regard to the quantified velocities within the stenosis, differences between the two orientations also become apparent in figure 4.31C. If the velocity vectors are along

the RO direction, the desynchronization between the spatial and velocity encoding time point leads to the same effect as for encoding scheme ECHO. The maximum velocity is quantified downstream of the stenosis. Along the PE direction, however, there is only a minor difference between the spatial and velocity encoding time points in the order of a few hundred μs . This small difference leads to almost no bias in the quantified velocity vector, if the flow is strictly oriented along PE direction. As a result, the maximum velocity is correctly obtained at the location of the smallest diameter within the stenosis.

Based on the previously described velocity vector fields, the WSS was estimated on the surface of the individual masks, defining the flowing regions. Corresponding results are shown in figure 4.32-4.34. The collision of the high velocity jet with the phantom wall leads to a local WSS hot spot. Furthermore, high WSS values are obtained within the stenosis. These features are clearly depicted by the results based on the SYNC SPI sequence (figure 4.32).

For encoding scheme ECHO, the estimated WSS maps also show the local hot spot (figure 4.33A+B), independent of the orientation of the imaging axes. Due to the displacement of the maximum velocities downstream within the stenosis, however, WSS values are substantially underestimated within the stenosis (figure 4.33C+D). Relative to the WSS obtained from the SYNC SPI measurement, this underestimation is up to 17%.

Figure 4.34 illustrates the WSS estimates obtained from encoding scheme FAST. Here, a dependency of the estimated WSS on the orientation of the imaging axes is observed. While the first orientation (figure 4.34A+C) preserves the local hot spot at the collision point of the high velocity jet with the phantom wall, it leads to an underestimation of the WSS within the stenosis of 14%, similar to encoding scheme ECHO. The second orientation, on the contrary, produces WSS values in accordance with the SYNC SPI sequence within the stenosis, but alters the WSS at the hot spot. Qualitatively, the wall shear stress pattern is visibly changed and the maximum values at the hot spot are reduced. Quantitatively, this reduction in peak WSS is 13% relative to the SYNC SPI results.

For further quantitative comparison between the WSS estimates based on the different encoding schemes, the individual geometries were parameterized by the two angles θ and φ as depicted in figure 4.36B. This parameterization allows a comparison on a pixel basis. Figure 4.35A+C-F shows the parameterized WSS maps for the SYNC SPI sequence as well as for encoding scheme ECHO and FAST. The two different orientations of the encoding axes are depicted by the subscripts 1 and 2, corresponding to the orientations on the left and right side of figure 4.33 and 4.34, respectively.

Correlation plots between the WSS estimate of the SYNC SPI sequence and the other

measurements are shown in figure 4.36. Here, the red line indicates the angular bisector. In accordance with the previous discussed results, it is evident that encoding scheme FAST is strongly dependent on the orientation of the imaging axes. The second orientation results in an underestimation of the WSS compared to the SYNC SPI sequence (figure 4.36D). This can also be seen quantitatively from the PEARSON'S linear correlation coefficient, shown in figure 4.37. Because regions of high WSS are clinically more relevant, pixels with less than one third of the maximum WSS of the SYNC SPI results were excluded from the analysis (figure 4.36). The correlation coefficients between all measurements, except for the second orientation of encoding scheme FAST, are above 0.86. While the correlation coefficient between the different orientations is 0.93 for encoding scheme ECHO, this is reduced to 0.36 for encoding scheme FAST.

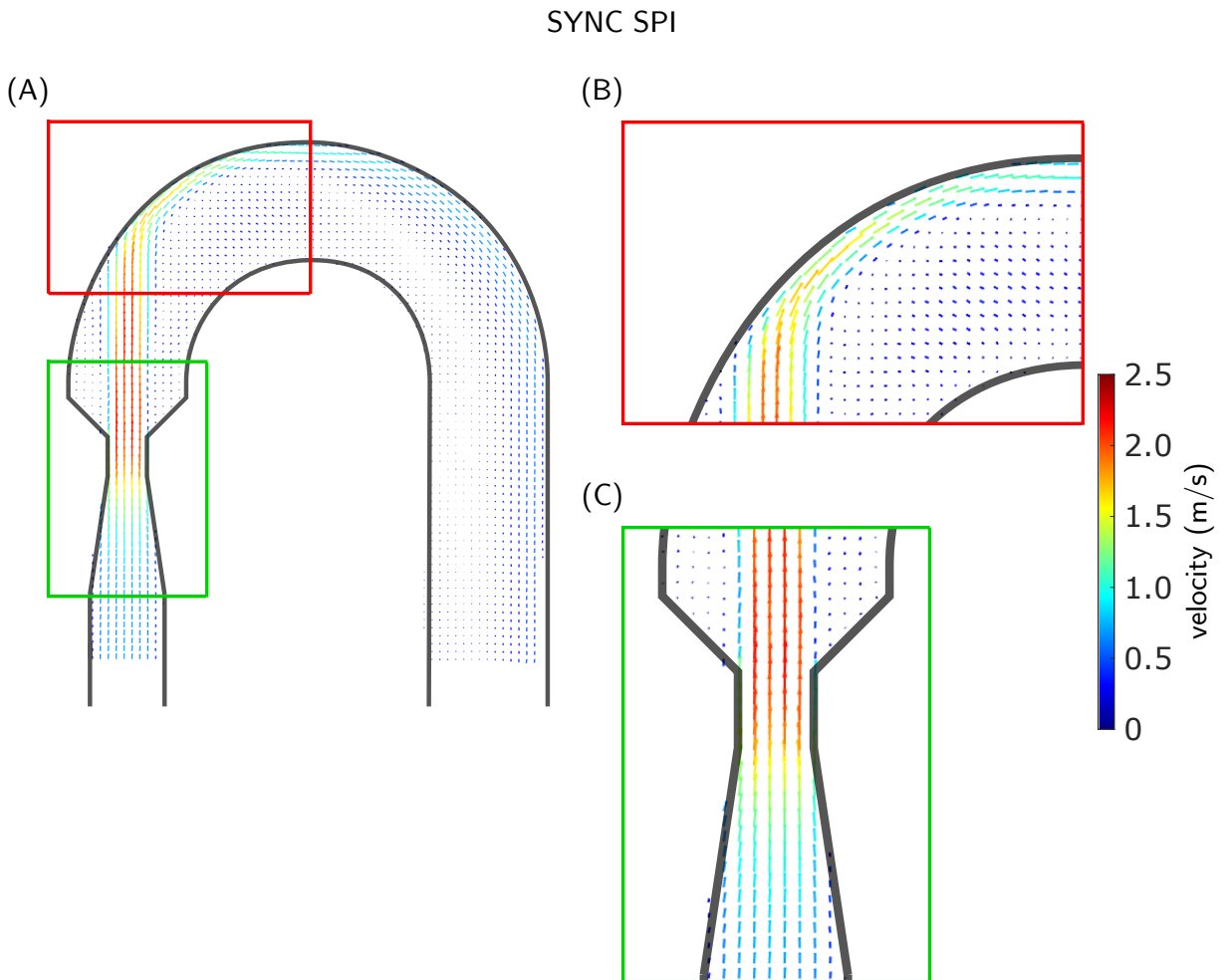


Figure 4.29: Central slice of the velocity vector field obtained from the SYNC SPI sequence. The two magnified parts (B+C) correspond to the marked parts in the overview (A). The true phantom geometry is shown in black.

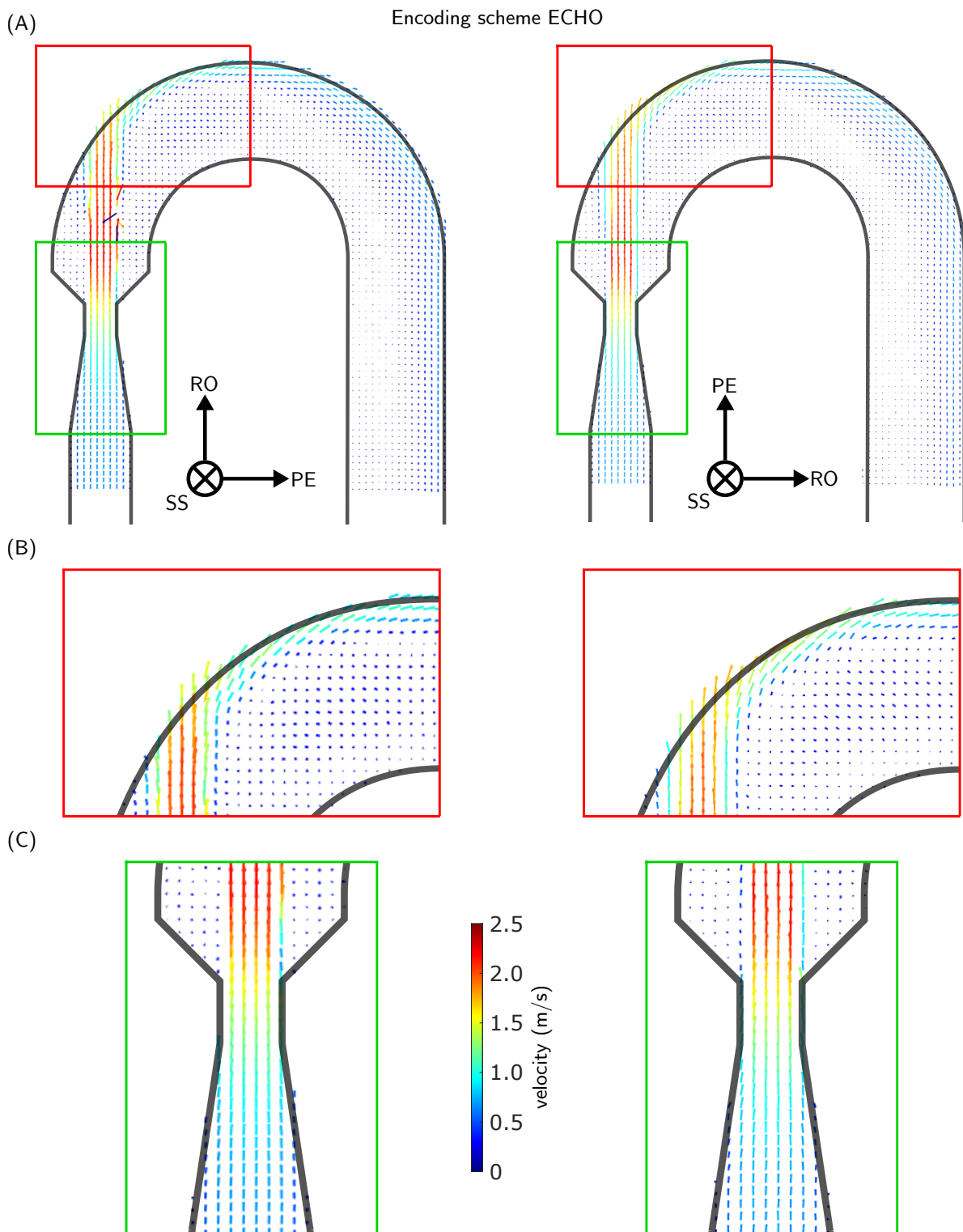


Figure 4.30: Central slice of the velocity vector field obtained with encoding scheme ECHO. The two magnified parts (B+C) correspond to the marked parts in the overview (A). The true phantom geometry is shown in black. The experiment was performed twice, with exchanged orientations of the RO and PE axes (left + right).

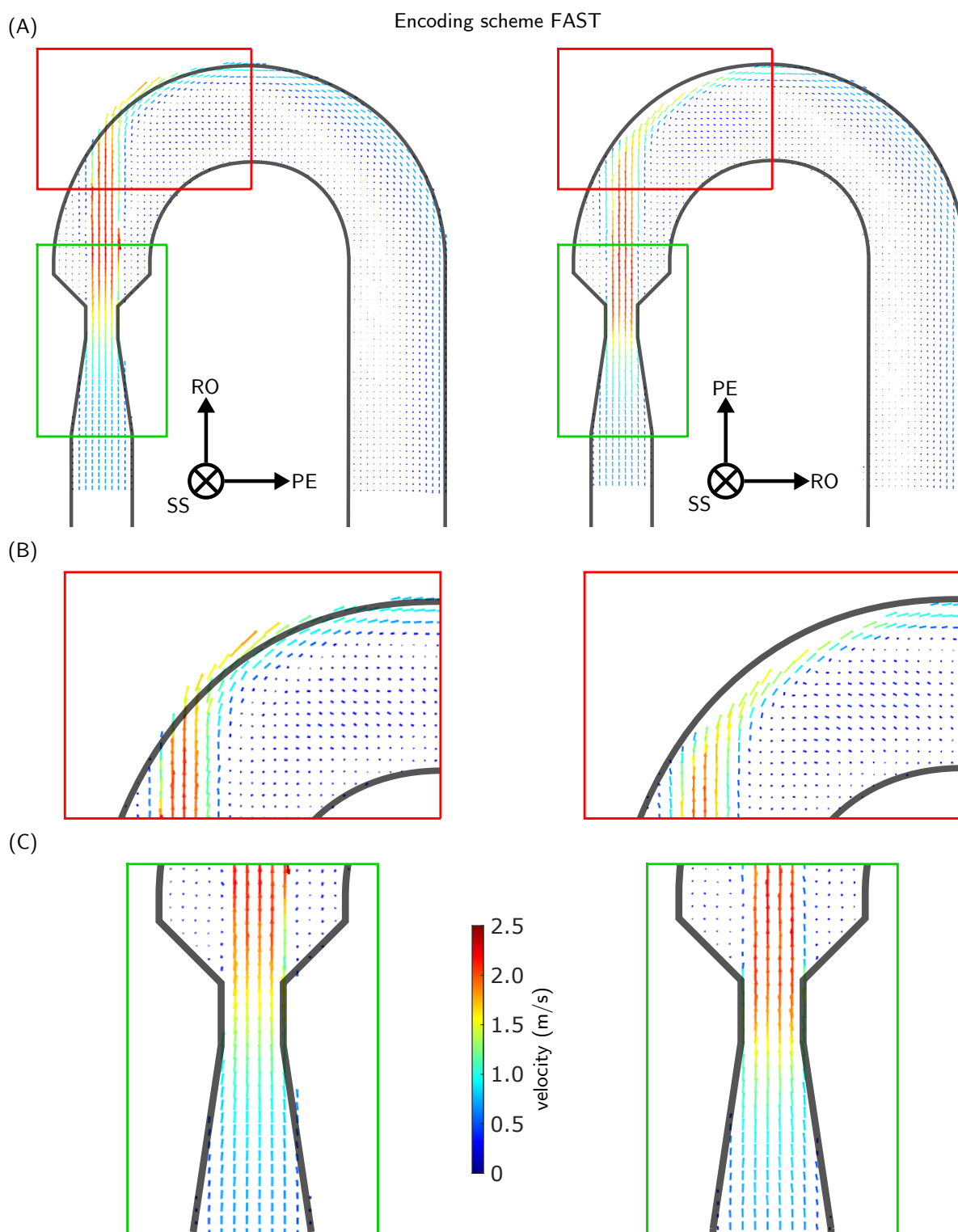


Figure 4.31: Central slice of the velocity vector field obtained with encoding scheme FAST. The two magnified parts (B+C) correspond to the marked parts in the overview (A). The true phantom geometry is shown in black. The experiment was performed twice, with exchanged orientations of the RO and PE axes (left + right).

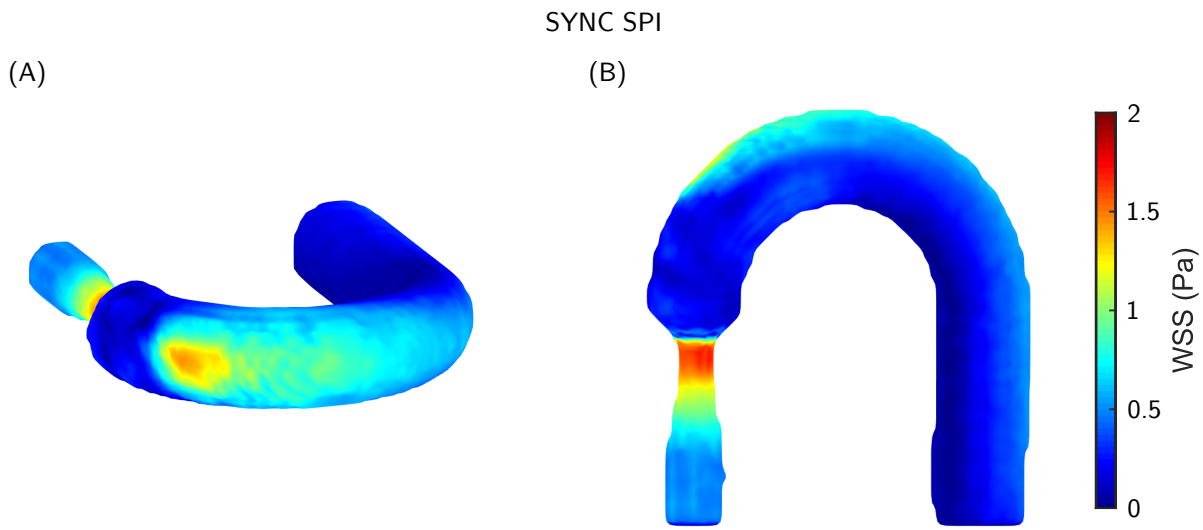


Figure 4.32: WSS estimation based on the velocity vector field acquired with the SYNC SPI sequence (c.f. figure 4.29).

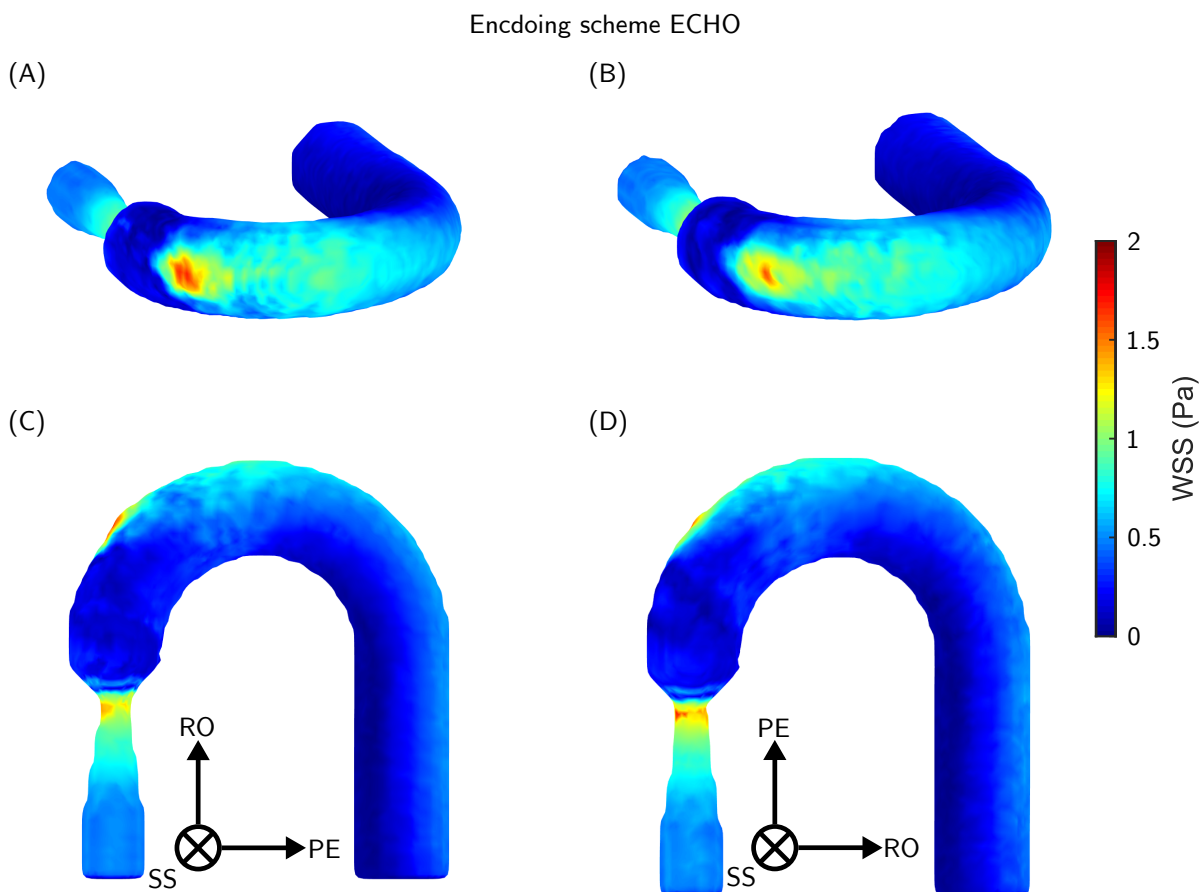


Figure 4.33: WSS estimation based on the velocity vector field acquired with encoding scheme ECHO (c.f. figure 4.30). The results from two measurements with different orientations of the imaging axes are shown (left + right).

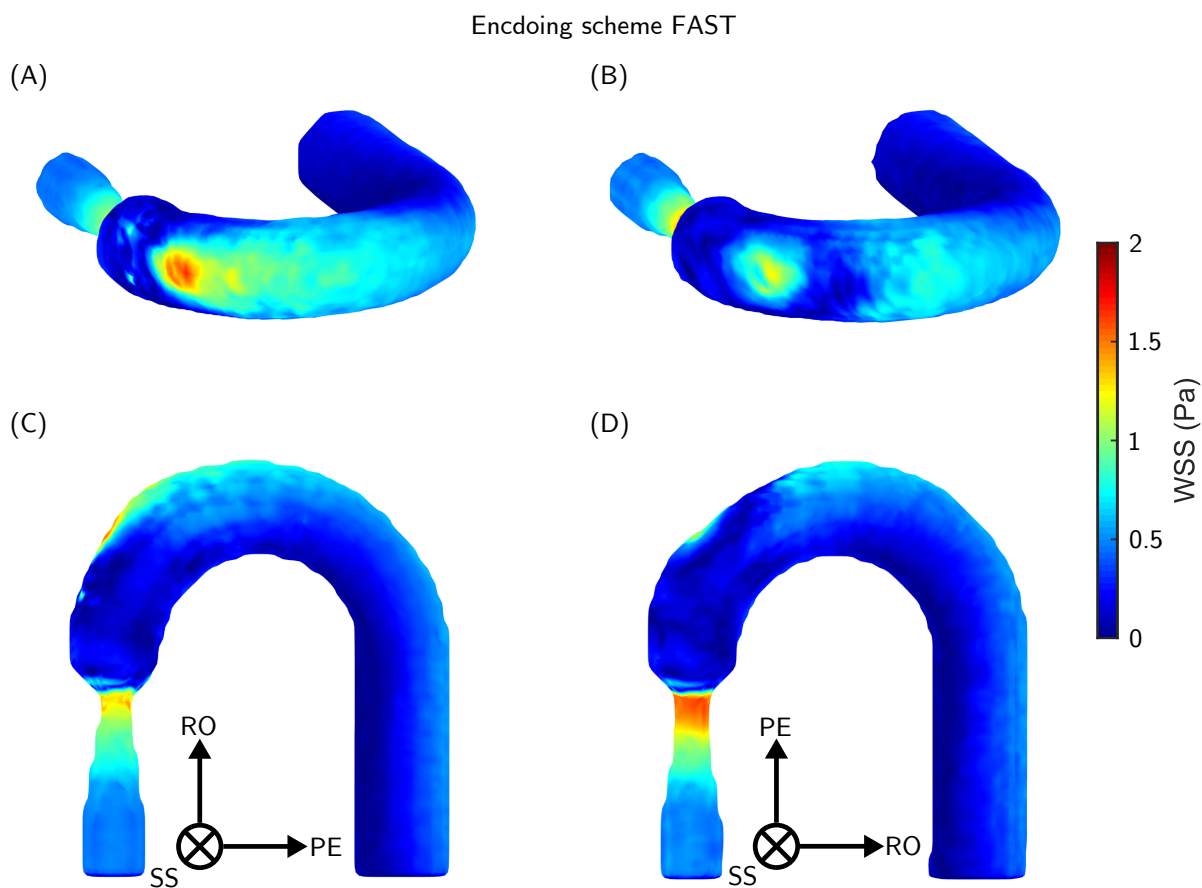


Figure 4.34: WSS estimation based on the velocity vector field acquired with encoding scheme FAST (c.f. figure 4.30). The results from two measurements with different orientations of the imaging axes are shown (left + right).

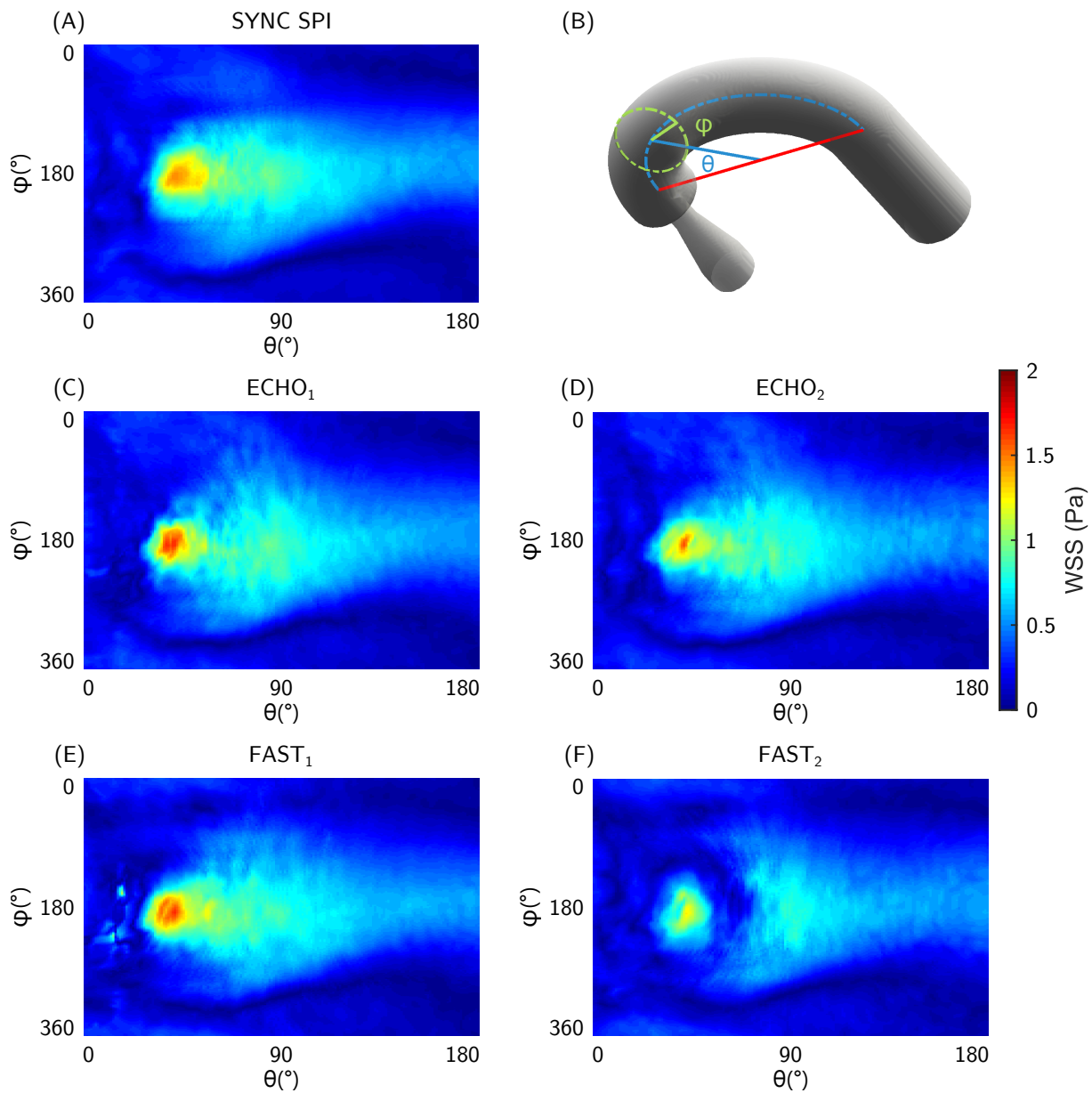


Figure 4.35: Parameterization of the WSS estimates shown in figure 4.32-4.34, according to the schematic in B.

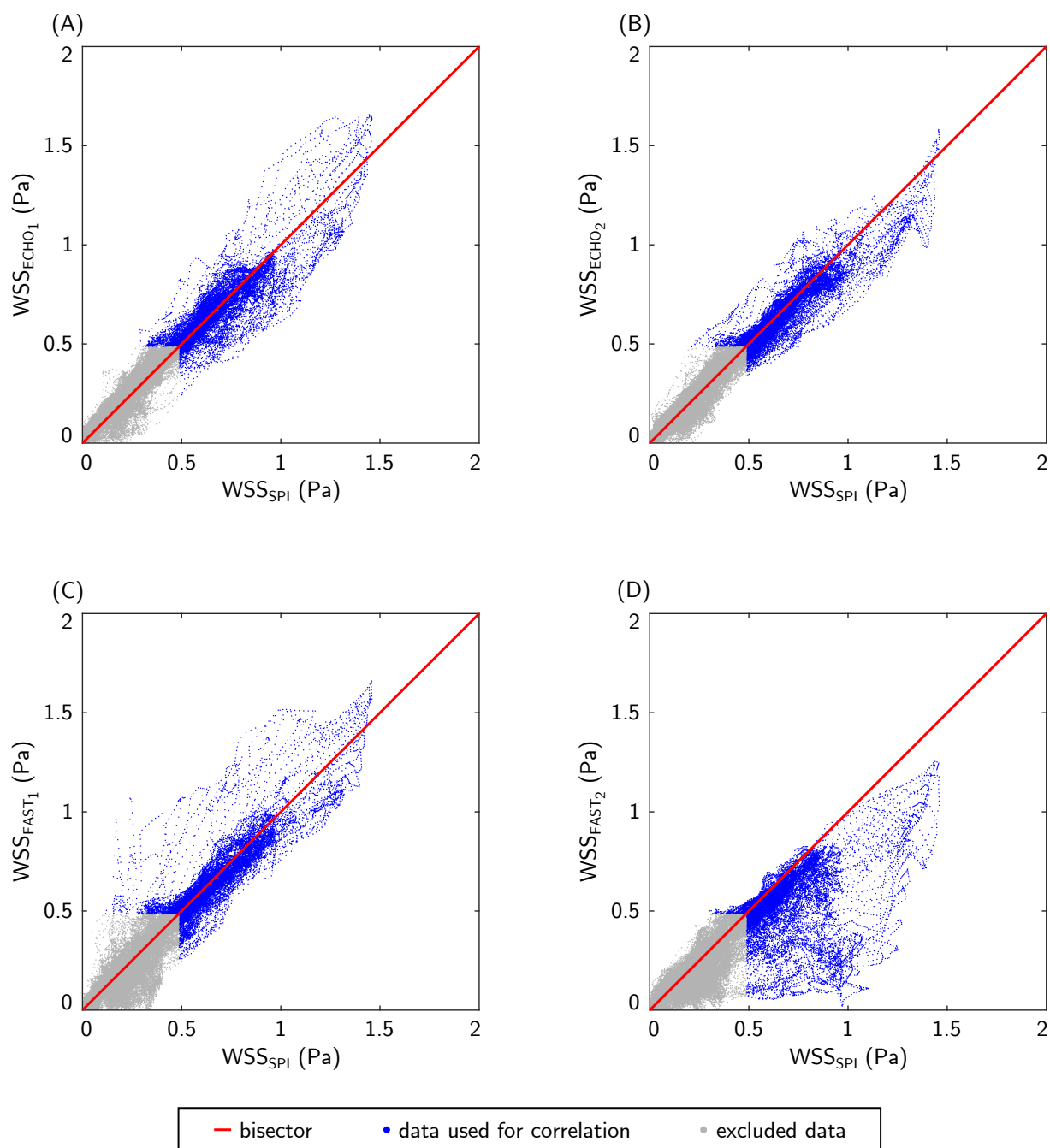


Figure 4.36: WSS estimates of encoding scheme ECHO (A+B) and FAST (C+D) as a function of the WSS estimate of the SYNC SPI. The red line indicates the angular bisector. Only the data shown in blue was used for the calculation of the PEARSON'S linear correlation coefficient shown in figure 4.37.

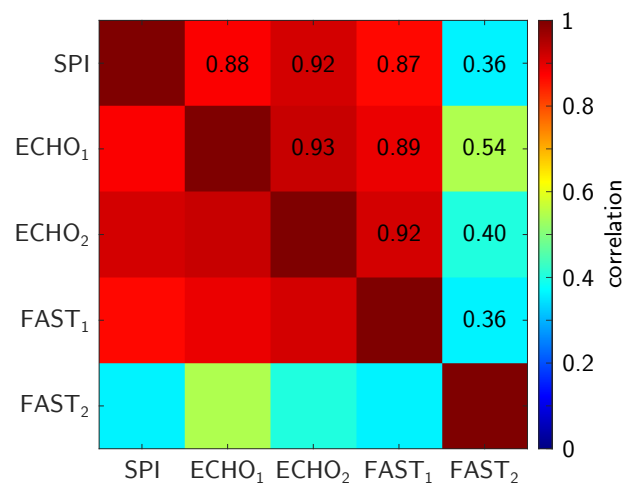


Figure 4.37: PEARSON'S linear correlation coefficient between all WSS estimates.

4.4 VENC optimization

4.4.1 Phantom measurements

To take into account the signal loss due to intravoxel velocity distributions in PC velocimetry and the associated increase in velocity noise, velocity spectra of constant flow in the straight flow phantom were acquired. An example slice of the FOURIER velocity encoded image is shown in figure 4.38A. Note that the axes of this image represent a spatial coordinate in the vertical direction and velocity in the horizontal direction. Figure 4.38B-E shows the corresponding velocity spectra along the blue and green dotted lines, corresponding to a central voxel and an edge voxel of the tube, respectively. Furthermore, measurements were performed with two different pump settings of constant flow rates of 20 mL/s and 80 mL/s. The measured spectra show an additional peak at 0 cm/s, arising from signal from static tissue that, however, was neglected in the further analysis. A GAUSSIAN distribution was fitted to all measured data along the velocity dimension and example fits are illustrated in red in figure 4.38B-E. With increasing pump rate, the distribution slightly broadens for the central voxel. For the edge voxel, in contrast, the low pump rate already leads to a significantly broadened distribution, which further increases with high pump rates. Quantitatively, the full width at half maximum of the GAUSSIAN fit increases from 2.5 cm/s to 11.0 cm/s and from 12.8 cm/s to 30.6 cm/s for the central and edge voxel, respectively.

Since conventional PC velocimetry yields the mean velocity within each voxel, the mean of the GAUSSIAN fit is expected to provide equivalent results to such a measurement, which is confirmed by the results shown in figure 4.39. The illustrated velocity maps are obtained from the mean of the GAUSSIAN fit for different constant pump settings. Line plots of the velocity profiles along the dashed lines in the corresponding velocity maps show a good agreement between the FOURIER velocity encoded data and conventional PC measurements.

Based on the measured velocity spectra, noise-optimized *VENC* values were calculated for each voxel, according to the method described in subsection 3.4.2 and the corresponding results are shown in figure 4.40. The velocity noise, depicted in figure 4.40A, shows the expected linear decrease with decreasing *VENC* value, before it reaches a minimum and begins to diverge due to the signal loss induced by intravoxel dephasing. For each voxel the noise-optimized *VENC* value is determined, which minimized the velocity noise. Corresponding results for pump settings of constant flow rates of 20 mL/s, 40 mL/s, 60 mL/s, and 80 mL/s are illustrated in figure 4.40B-E. At the edge of the tubes, the velocity spec-

tra are broader due to the high spatial variation of the velocity profile, resulting in higher optimal $VENC$ values of up to 30 cm/s for symmetric encoding (corresponding to 60 cm/s for single-sided encoding).

Phantom experiments with pulsatile flow (figure 4.41) with peak mean velocities of 60 cm/s lead to similar results of optimal $VENC$ values of up to 30 cm/s, which will double, if single-sided encoding is used. Due to additional temporal gradients of the velocity vector field, the maximum optimal $VENC$ values did not appear at the same time as the peak velocity (at approximately 300 ms), but with a delay of approximately 50 ms.

In addition to the phantom experiments, in vivo data targeting the femoral artery of a female healthy volunteer was acquired and evaluated for noise-optimized $VENC$ values. The obtained results agree with the values from the pulsatile phantom experiments with optimal $VENC$ values of up to 30 cm/s for symmetric encoding. Note that the in vivo data is not shown here.

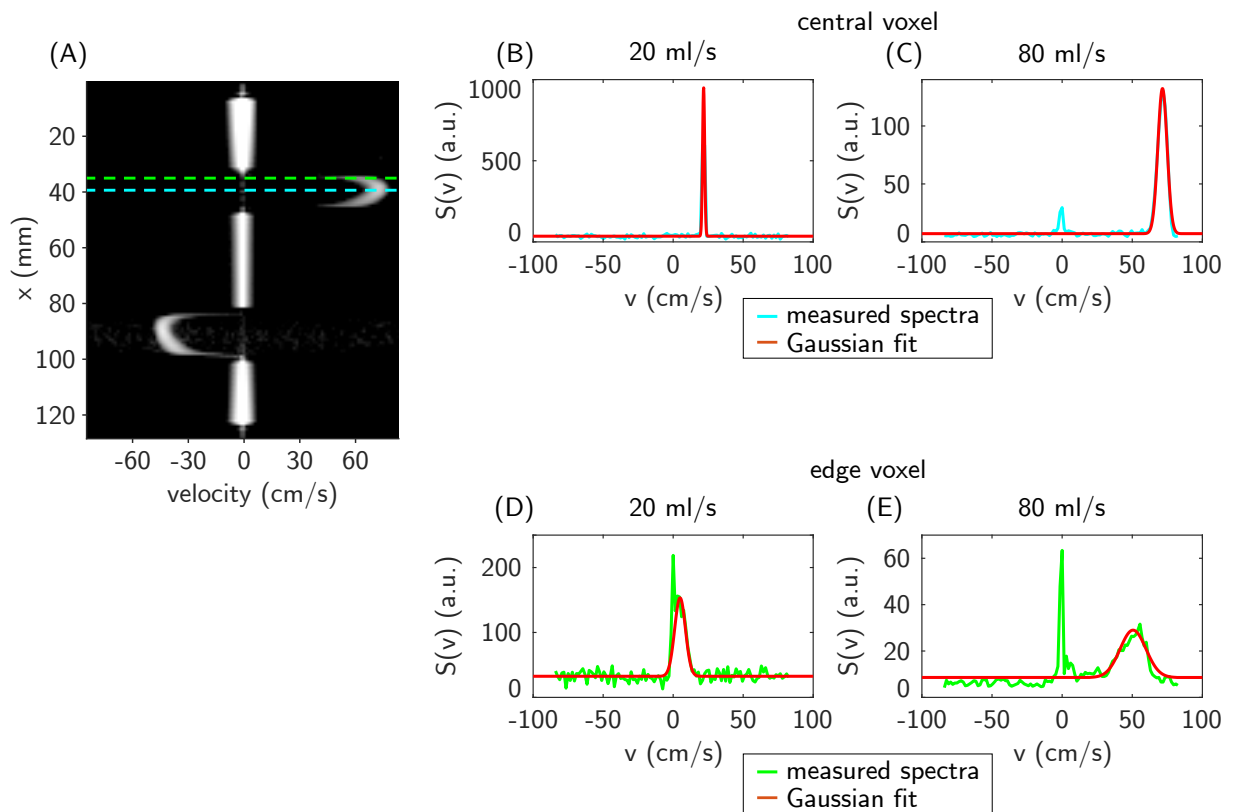


Figure 4.38: FOURIER velocity encoded image (A) with a resolution of 1.5 cm/s in velocity direction acquired in the straight flow phantom with a pump setting of 80 mL/s. Corresponding spectra for a central voxel (B+C) and an edge voxel (D+E) are shown for pump settings of 20 mL/s (B+D) and 80 mL/s (C+E). The positions of these voxels are indicated by the blue and green dashed lines (A). In addition to the measured velocity spectra, GAUSSIAN fits are shown in red.

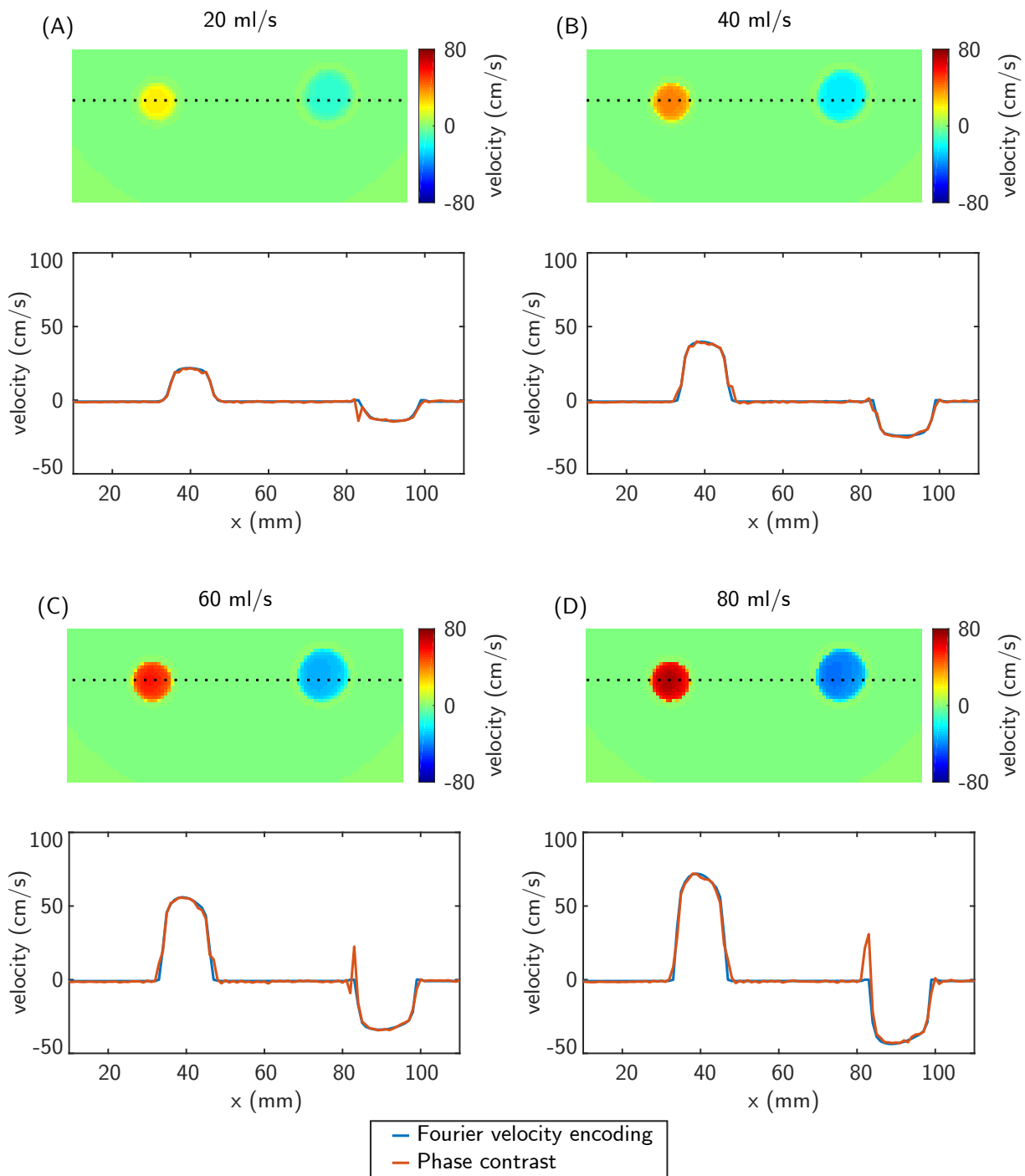


Figure 4.39: Velocity maps obtained from the mean of the GAUSSIAN fit for different pump settings with corresponding line plots along the black dotted lines. In addition, velocity profiles from a conventional PC measurement are shown.

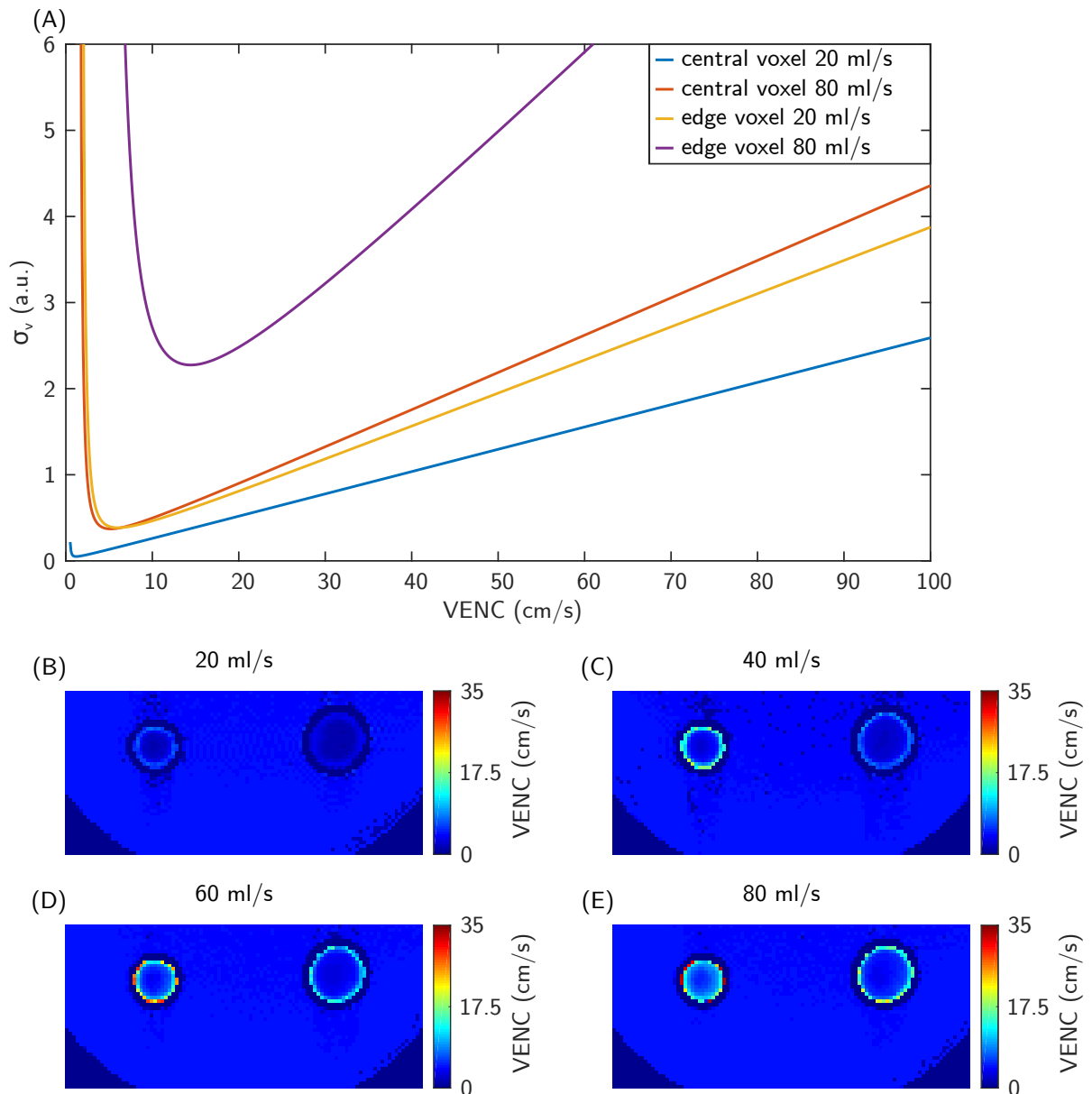


Figure 4.40: Velocity noise σ_v as a function of the $VENC$ value (A) for an example central and edge voxel and for two different pump settings of 20 mL/s and 80 mL/s. An overview of the optimized $VENC$ values in each voxel is shown for different pump settings of 20 mL/s, 40 mL/s, 60 mL/s, and 80 mL/s (B-E).

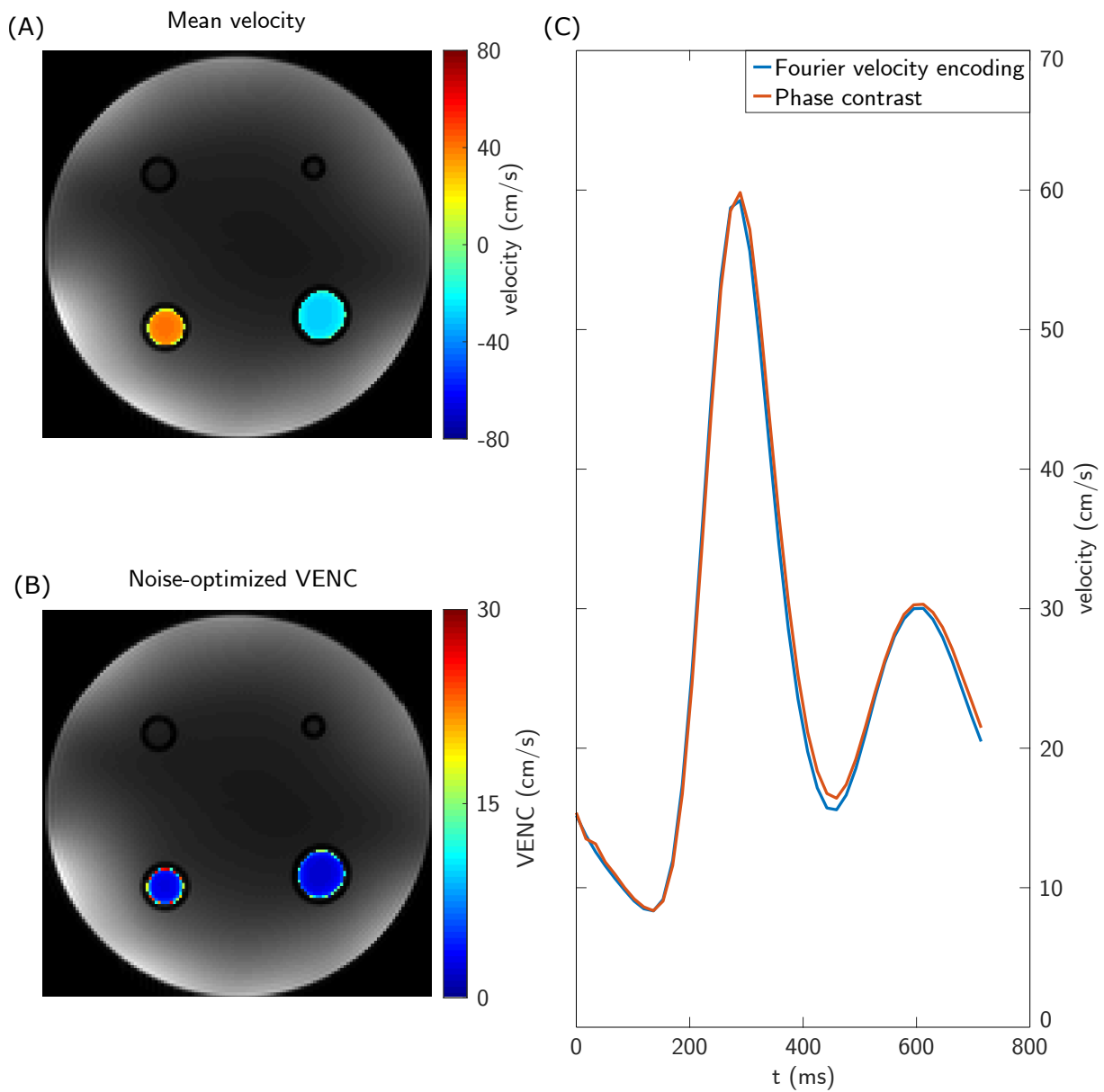


Figure 4.41: Mean velocity (A) and noise-optimized $VENC$ values (B) corresponding to the time point at 300 ms after the trigger pulse (C).

4.5 Acceleration quantification

4.5.1 Phantom measurements

Similar to velocity quantification, acceleration quantification is prone to the displacement artifact. Figure 4.42 illustrates the differences between acceleration maps acquired with encoding scheme ECHO and the acceleration-encoded SYNC SPI sequence. Because both sequences synchronize the spatial encoding time points of all imaging axes, no geometrical distortions of the circular phantom are observed. The non-synchronous spatial and acceleration time points of encoding scheme ECHO lead to a bias of the quantified acceleration vector field. The maps of the individual acceleration components appear rotated by 31° , compared to the SYNC SPI measurement. This also becomes apparent in the corresponding quiver plots in figure 4.43. The SYNC SPI sequence leads to an acceleration vector field that points inward in radial direction. In comparison, encoding scheme ECHO leads to a distorted acceleration vector field that appears twisted. Note that the SYNC SPI measurement shows some image artifacts, prominently in the middle of the phantom, in vertical direction.

4.5.2 In vivo measurements

Figure 4.44A shows a magnitude image during mid-systole obtained with an optimized B_1 phase shim. The red area was used in figure 4.44B-D to mask noise regions and to evaluate the standard deviation in the quantified vector fields at end-diastole. The measured velocity vector field shows low velocity noise with a standard deviation of 0.09 m/s. However, the calculated acceleration yields a poor quality with a standard deviation of 27 m/s. In comparison, the measured acceleration vector field has a standard deviation of 4 m/s. Furthermore, since only a 2D acquisition of the velocity vector field could be performed, only the temporal term $\frac{\partial \vec{v}}{\partial t}$ and parts of the convective term $(\vec{v} \cdot \nabla) \vec{v}$ could be calculated. This yields deviations between the calculated and measured acceleration, especially in the aortic root (black arrow in figure 4.44) of up to 65 m/s. The long acquisition time of the acceleration-encoded SYNC SPI sequenced rendered it unfeasible for in vivo applications.

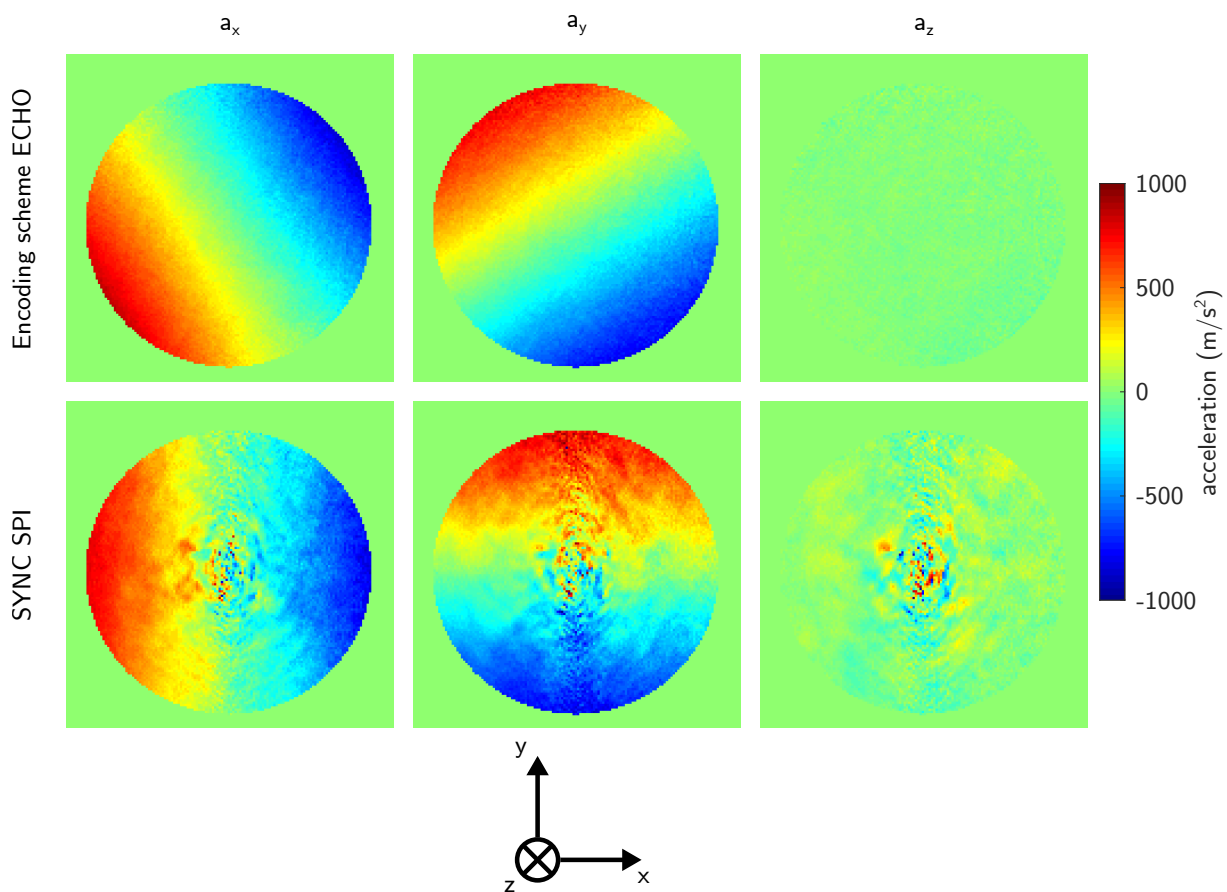


Figure 4.42: Maps of the three acceleration components in the rotation phantom acquired with encoding scheme ECHO and the acceleration-encoded SYNC SPI sequence.

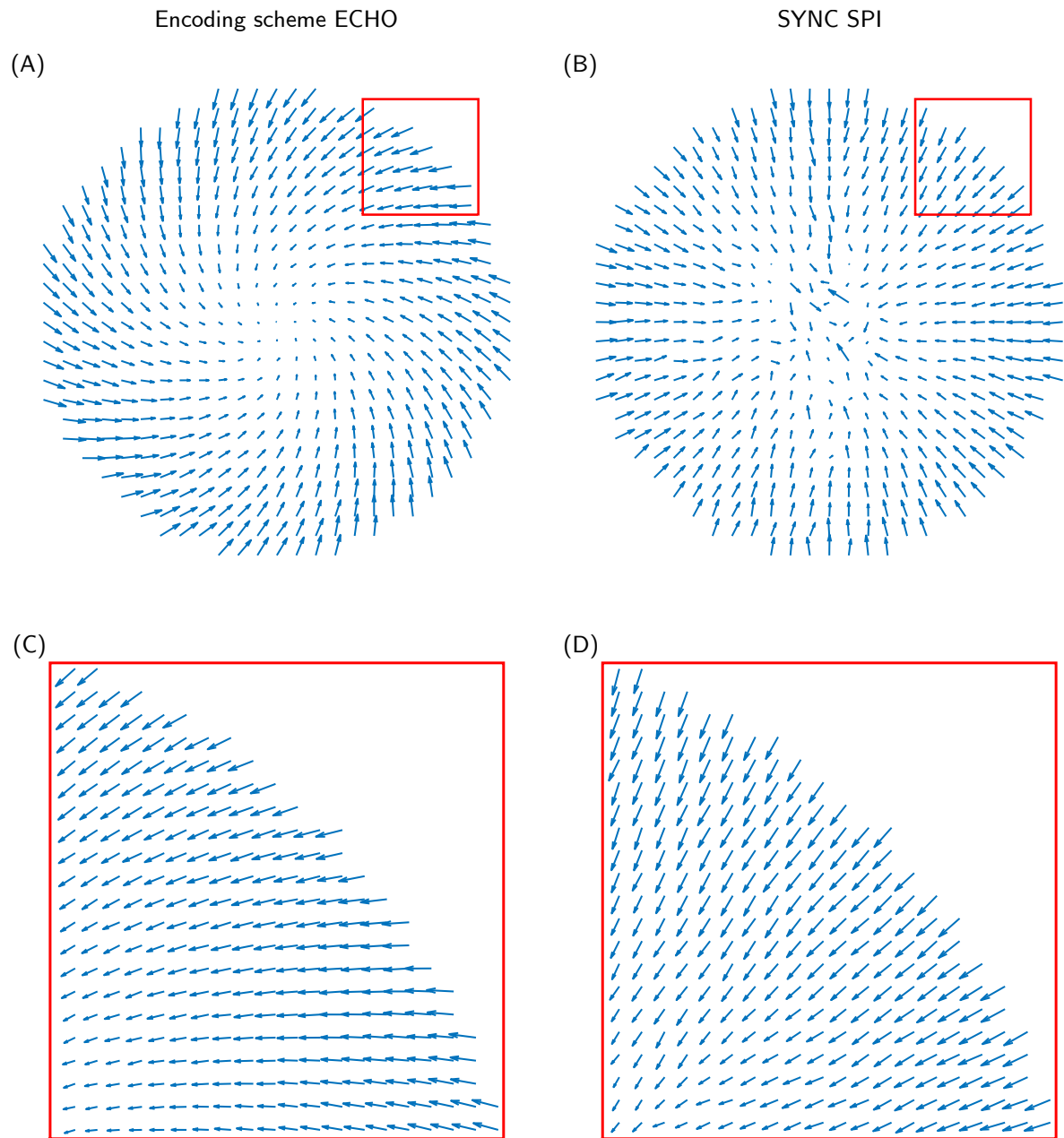


Figure 4.43: Quiver plots of the acceleration maps shown in figure 4.42. The magnified parts (C+D) correspond to the marked parts in the overviews (A+B). For better visualization, only every fifth vector was plotted in A+B.

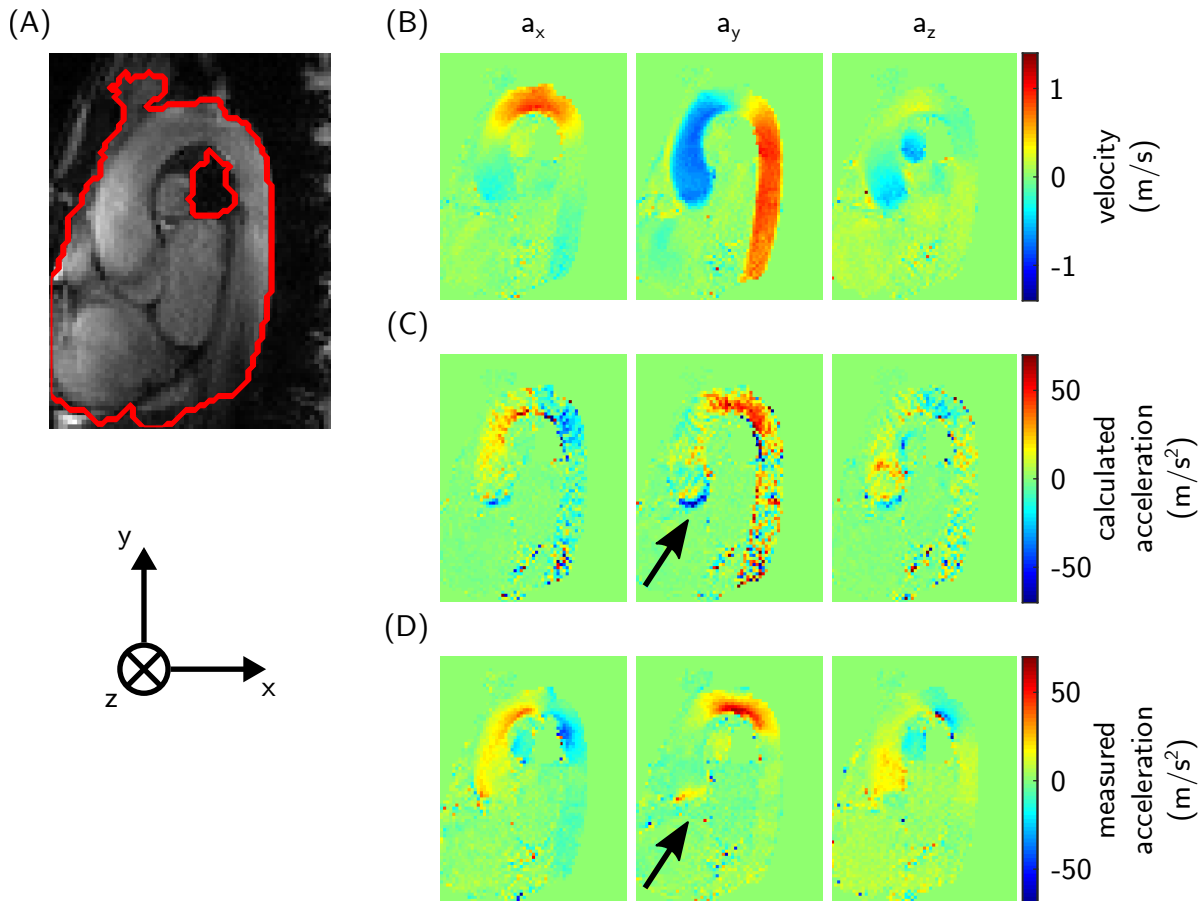


Figure 4.44: Magnitude image (A) and mask (red) used to mask noise regions in the quantitative maps (B-D). All images correspond to the same time-frame in mid-systole. Shown are the three measured velocity components (B), calculated acceleration components (C), and measured acceleration components (D).

4.6 Reynolds stress tensor quantification

4.6.1 Phantom measurements

From the data of multiple measurements with ICOSA6 encoding (c.f. subsection 2.5.7), which differ in the applied m_1 value, the velocity vector field and the components of the RST were quantified. The latter was quantified from single measurements with a single m_1 value as well as from the complete set of acquired data with twelve different m_1 values.

Figure 4.45A shows a normalized magnitude image acquired in the in-vitro flow test case, which consisted of 13 identical consecutive hills. Flow is in the direction from left to right and the displayed section covers the 10th (left) and 11th (right) hill. The corresponding reconstructed components of the velocity vector field (figure 4.45B) show that the velocities are restricted to the x-y plane. Furthermore, it was experimentally confirmed that the velocity does not change along the z-direction within the acquired 2D slice. The recirculation region in the wake of the hills is clearly depicted by the measured velocity vector field.

Example images of the logarithm of the normalized image magnitude for all acquired m_1 values are shown in figure 4.46A, corresponding to the second encoding direction according to equation 2.111. From these images it becomes apparent that this test case covers a high range of turbulence intensities, which is quantitatively confirmed by figure 4.46B, displaying the measured normalized image magnitude of two example regions marked in figure 4.46A. In addition, the projection of the obtained three-dimensional GAUSSIAN fits along the second encoding direction are indicated. As described in the subsection 3.4.4, data points with less than 10% normalized image magnitude were excluded from the fit to account for the RICIAN nature of the magnitude noise. Figure 4.46C+D shows the same data in logarithmic representation over the square of m_1 , which corresponds to a linearization of the GAUSSIAN distributions. Besides the fit to the full data, corresponding to twelve different m_1 values, GAUSSIAN distributions were fitted to the data of each individual m_1 value (c.f. HARALDSSON et al. [20]). Figure 4.46C+D shows corresponding results for the full data set (solid lines) and two example fit results to individual m_1 values of 15 mT ms²/m and 45 mT ms²/m (dashed lines). In the case of high turbulence (figure 4.46D), the fit to a single measurement of 45 mT ms²/m leads to a substantial overestimation of the variance of the GAUSSIAN fit and, therefore, to an underestimation of the RST.

These differences become more apparent in figure 4.47-4.49. First, all six components of the RST, quantified by the GAUSSIAN fit to the full data set, are illustrated in figure 4.47.

As expected, τ_{xx} and τ_{xy} are the highest normal and shear stresses with peak values of $0.17 \text{ m}^2/\text{s}^2$ and $0.10 \text{ m}^2/\text{s}^2$, respectively. In contrast, lower shear stresses of $0.05 \text{ m}^2/\text{s}^2$ and $-0.02 \text{ m}^2/\text{s}^2$ are obtained for τ_{xz} and τ_{yz} . Figure 4.48 and 4.49, on the contrary, display results from the GAUSSIAN fits to individual m_1 values (here five example values). For low m_1 values, amplification of the noise is observed, whereas high m_1 values lead to an underestimation of peak stress of up to 3-fold for τ_{xx} , compared to the results shown in figure 4.47. Furthermore, the measurement of a single m_1 value fails to correctly quantify the smallest shear stress components τ_{xz} and τ_{yz} .

Based on the quantified RST via the full data set of twelve different m_1 values, the turbulent kinetic energy was calculated, yielding peak values of $0.17 \text{ kJ}/\text{m}^3$, as illustrated in figure 4.50.

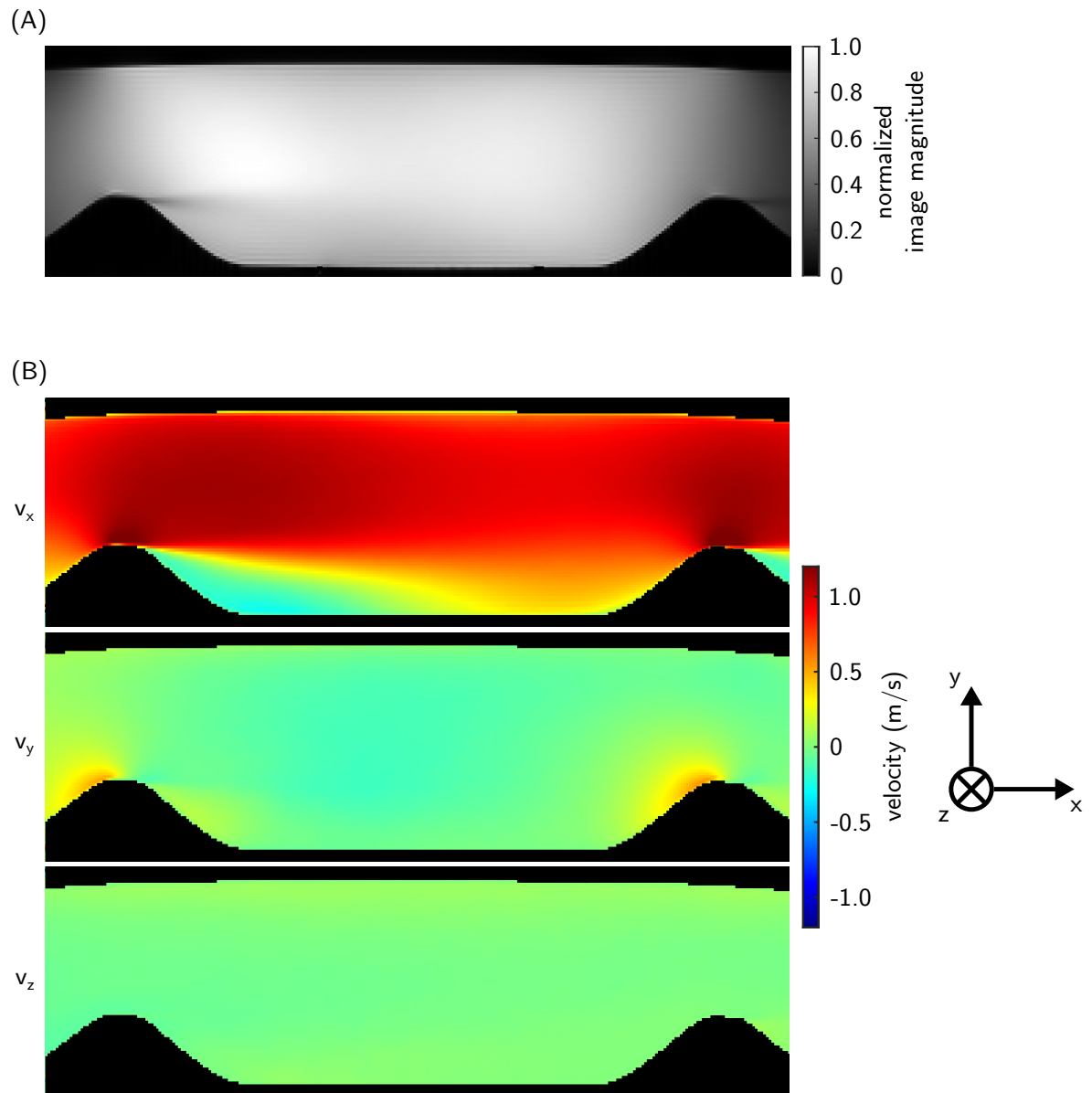


Figure 4.45: Normalized image magnitude (A) and velocity components (B) reconstructed from the data corresponding to the five lowest m_1 values.

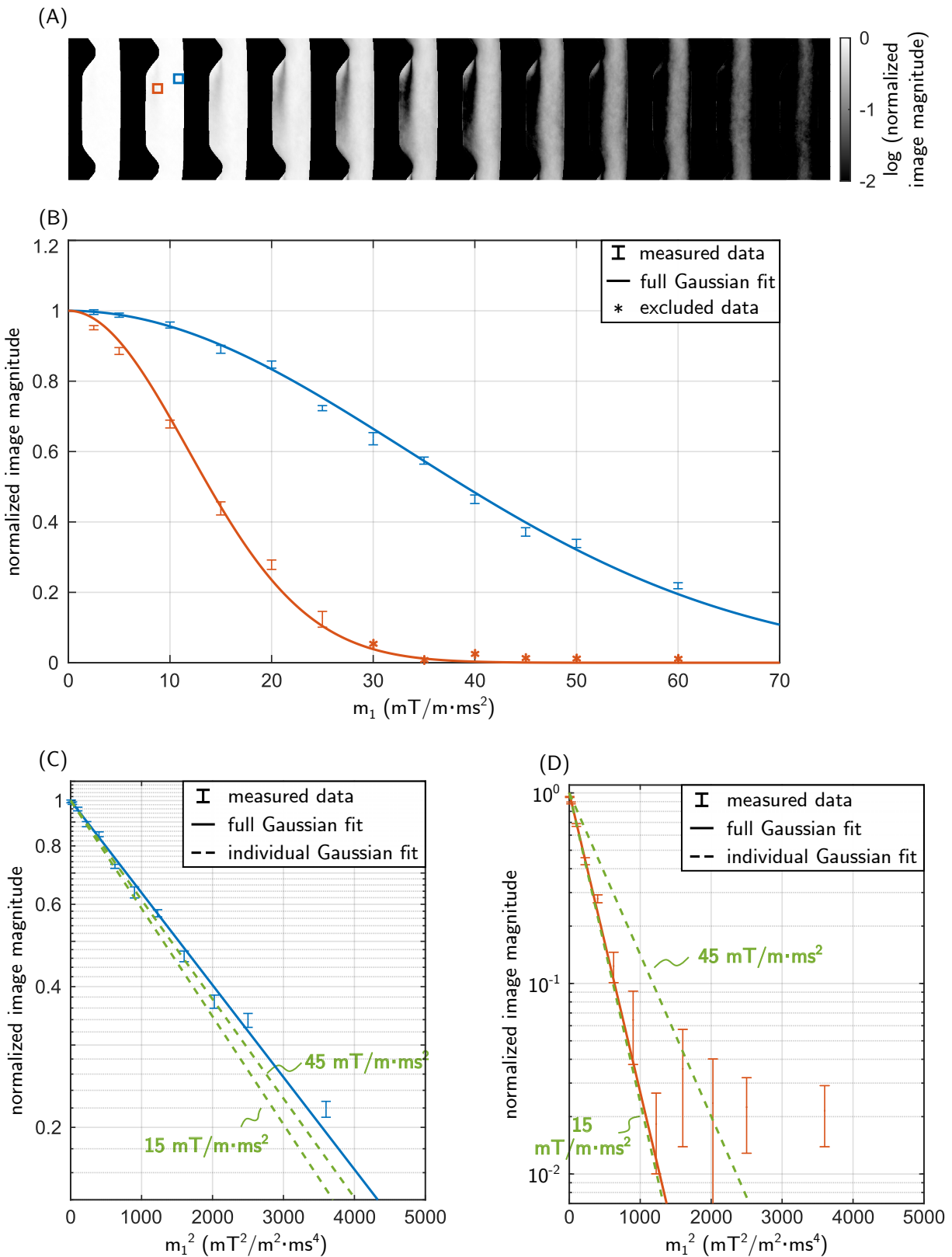


Figure 4.46: Logarithm of the normalized image magnitude (A), corresponding to the second encoding direction of the ICOSA6 encoding for all m_1 values. Data points marked by an asterisk (B) were excluded from the GAUSSIAN fits to the complete data set. A semi-logarithmic display of the normalized magnitude data (C+D) illustrates the differences between a GAUSSIAN fit to the the full data set and to individual m_1 values.

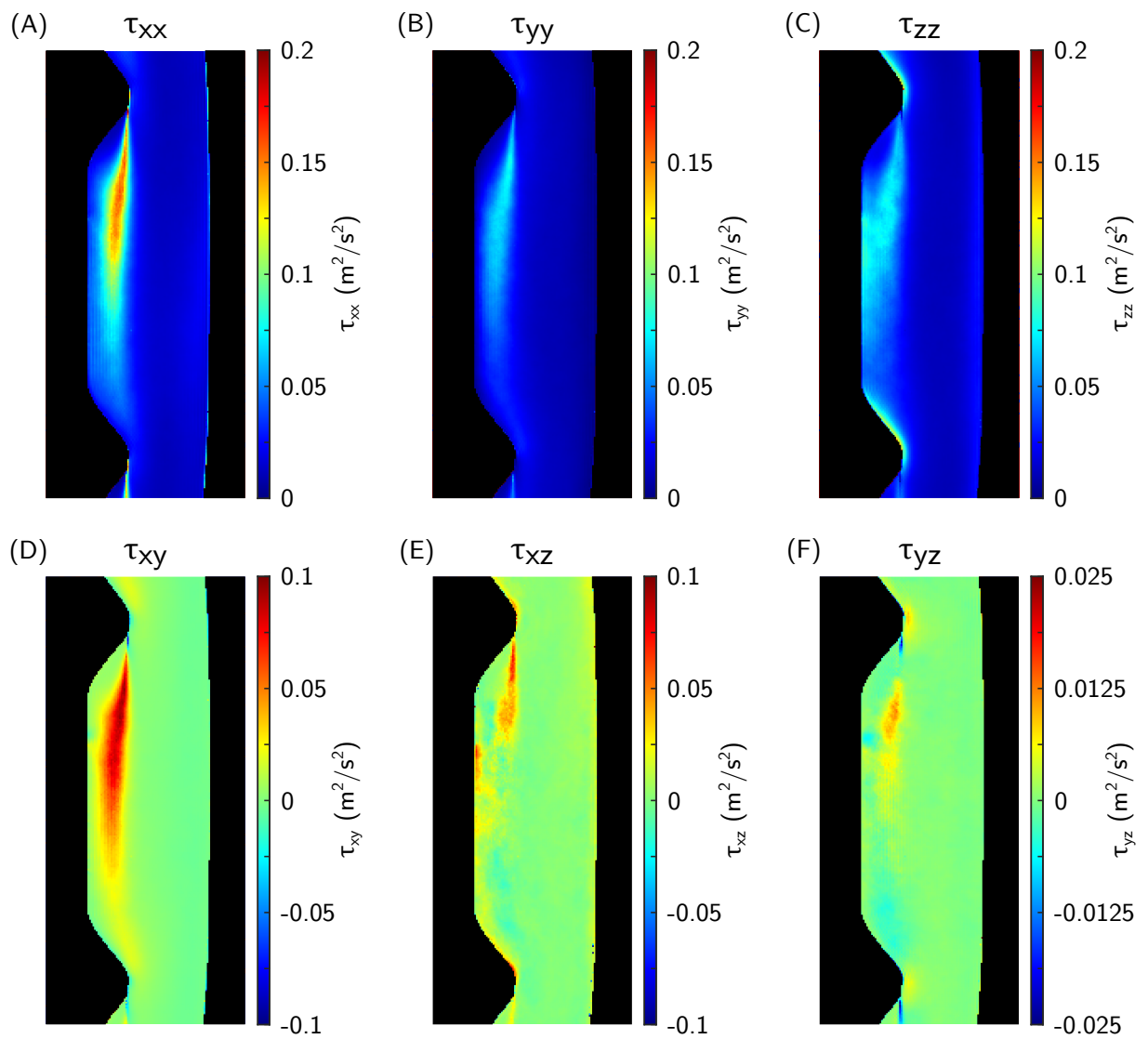


Figure 4.47: Calculated RST components obtained from the GAUSSIAN fit to the complete data set. Note that the scaling is not identical for each component.

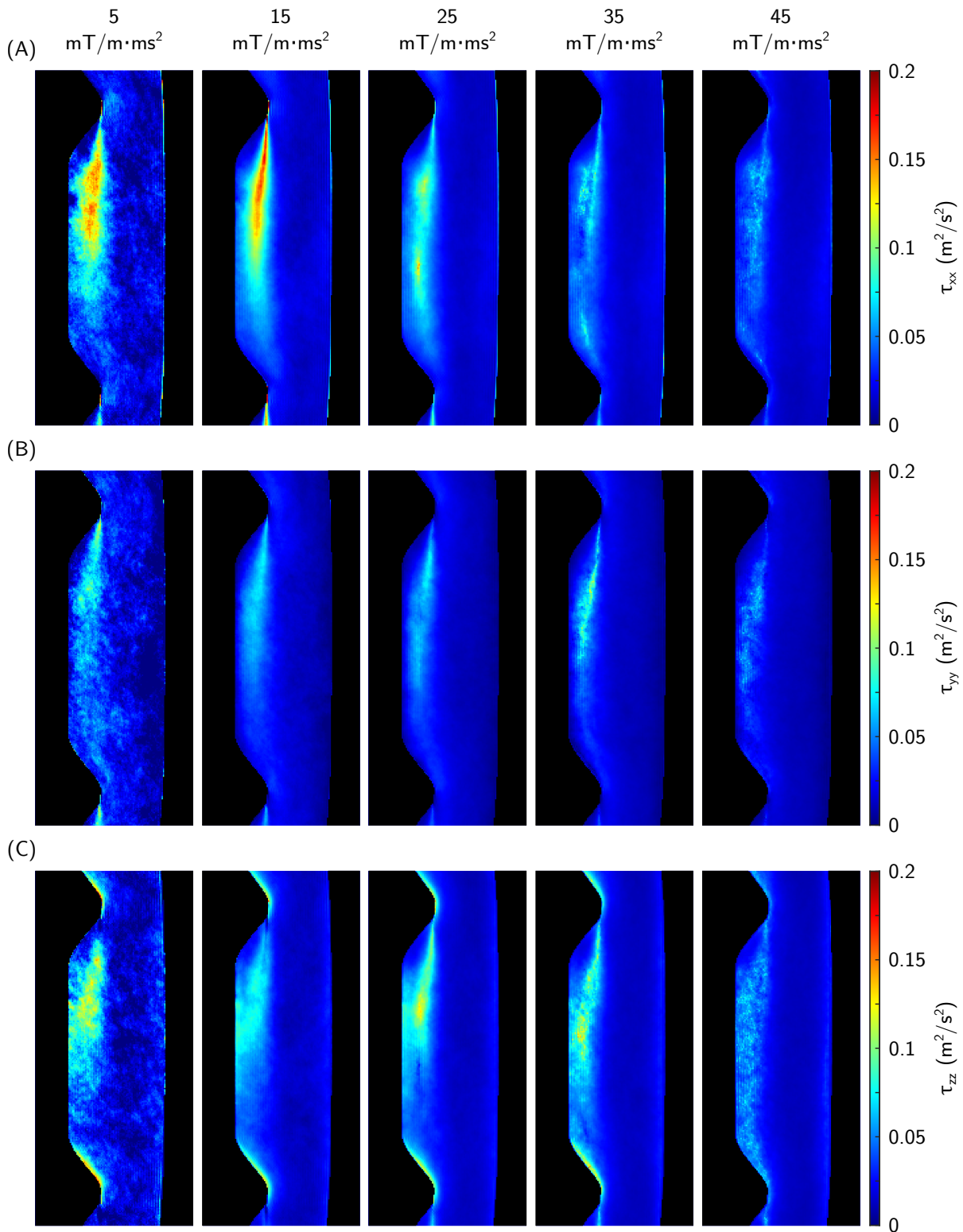


Figure 4.48: Normal stresses obtained from the GAUSSIAN fits to individual m_1 values.

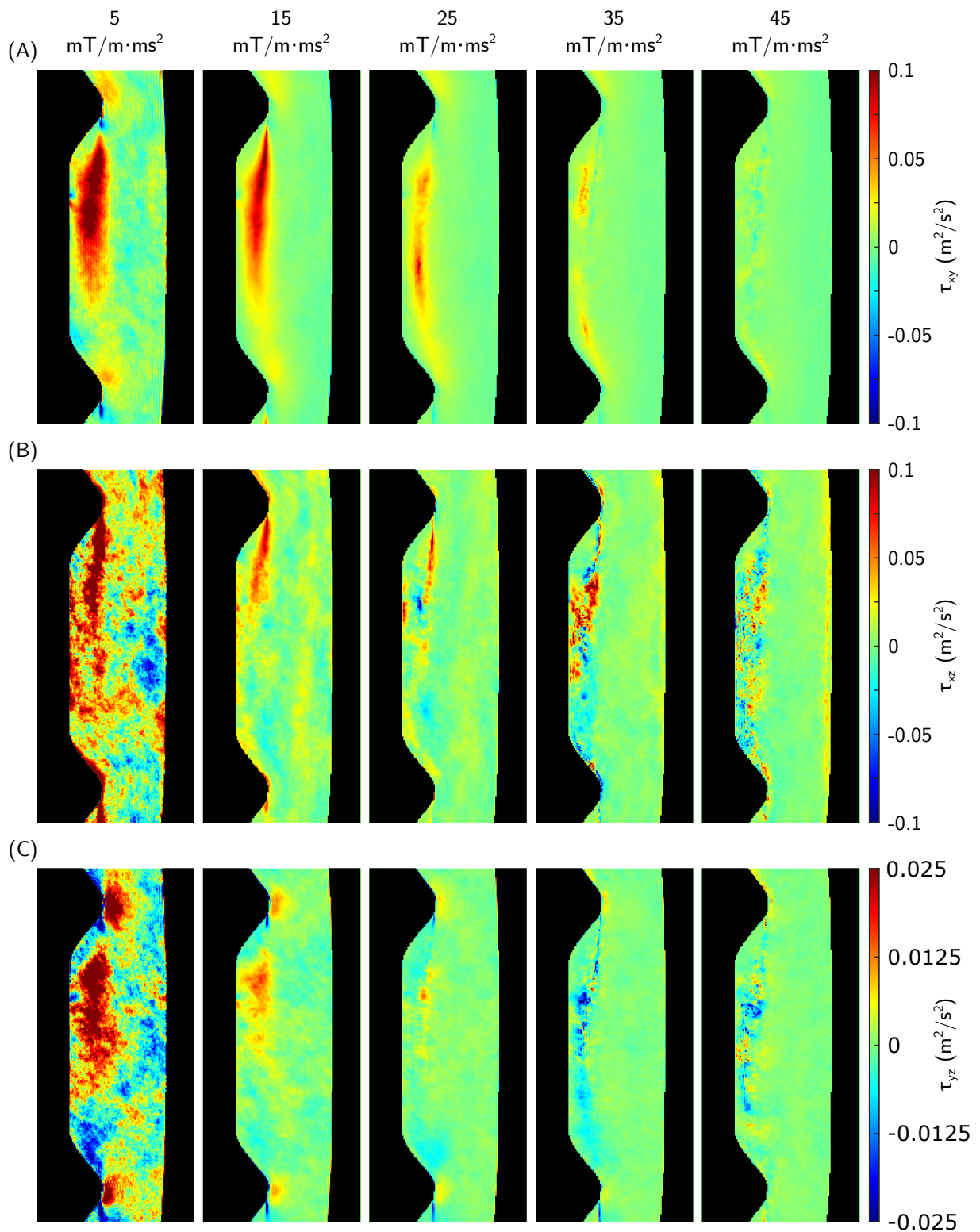


Figure 4.49: Shear stresses obtained from the GAUSSIAN fits to individual m_1 values. Note that the scaling is not identical for each component.

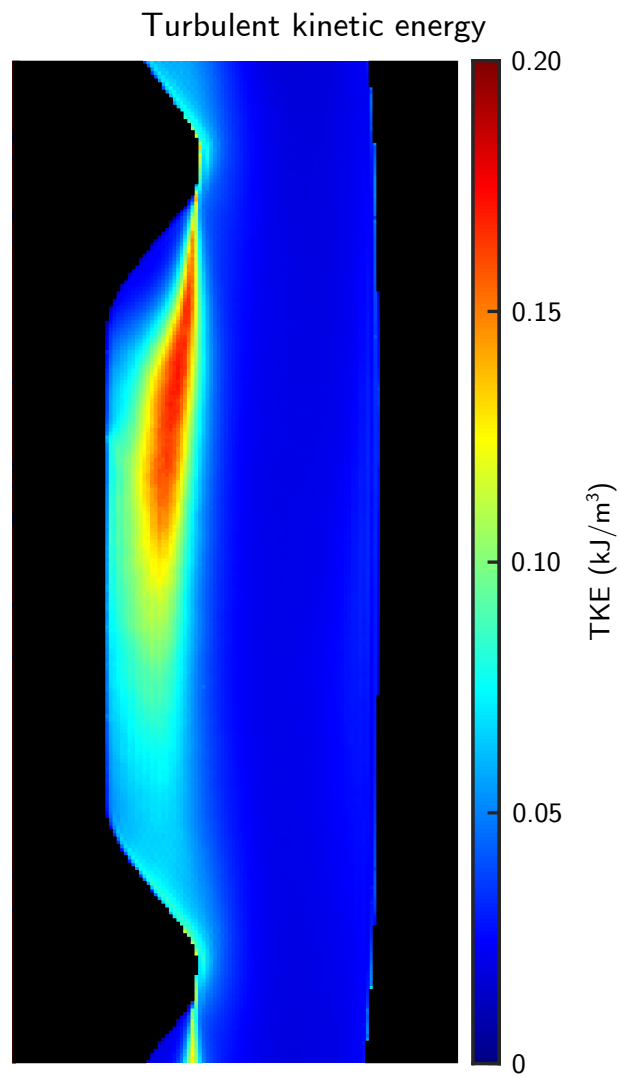


Figure 4.50: Turbulent kinetic energy given by the trace of the RST shown in figure 4.47.

5 Discussion and Outlook

The main objective of this work was the accurate quantification of fluid mechanical properties by MRI. This included a detailed analysis of the so-called displacement artifact that arises during the imaging of non-stationary magnetization. Different encoding schemes for velocity quantification were investigated and expanded to multi-spoke excitation, which requires special attention regarding the gradient moments experiences by each magnetization subset. Furthermore, the influence of displacement artifacts on the estimated WSS and direct acceleration mapping was evaluated. In this context, a new encoding scheme was presented, which allows gold-standard-like acceleration mapping. In addition, a new method for optimizing velocity noise in velocity-encoded measurements was proposed that includes the effect of intravoxel velocity distributions. Last, turbulent flow was investigated in a well-known fluid dynamic test case to determine the accuracy of RST mapping with MRI.

5.1 Velocity quantification

The presence of displacement artifacts in velocity encoded MRI experiments and their origin is not a new research topic. In fact, it was investigated already three decades ago [15, 16, 36, 38–40]. In the meantime, MR-based velocimetry has undergone a tremendous development and is now used in clinical routine. The fundamental problem of displacement artifacts has remained, but got less and less attention over time. In the context of multi-spoke RF pulses, these artifacts need to be reconsidered, but beyond that it is of crucial importance to know their influence even with conventional excitation. To this end, three different encoding schemes were investigated and applied to multi-spoke excitation that differ in their respective displacement artifacts. First, encoding scheme FAST was analyzed, which is frequently used for velocity-encoded MRI. This encoding scheme is the fastest among the examined ones. Furthermore, the exact calculation of realistic encoding gradients (trapezoidal and triangular) is published [48]. Second, encoding scheme ECHO that synchronizes the spatial encoding time points of all three imaging axes at the center of the echo. And third, the newly proposed encoding scheme ISO that synchronizes the spatial encoding time points of the PE and SS axes at the isophase point of the RF pulse. For the latter two, the calculation of realistic encoding gradients with minimal total duration is presented in this work.

The description of the effects of these different encoding schemes on the quantified velocity vector field can conveniently be reduced to the spatial and velocity encoding time points. Common among the different encoding schemes are the locations of the velocity encoding time points. Because the bipolar velocity encoding gradients are applied simultaneously on all imaging axes, the velocity encoding time points all coincide within a few hundred μs . The exact position of the velocity encoding time points is given by the center of gravity of the bipolar gradient difference function along each encoding direction [41]. The differences between the different encoding schemes, however, become apparent with regard to the spatial encoding time points. Due to the nature of the MRI data acquisition, the spatial encoding time point in RO direction is always located at the center of the echo.

Since encoding scheme FAST is not explicitly designed to control the spatial encoding time points in PE and SS direction, they are between the end of the RF pulse and the beginning of the data acquisition period (c.f. figure 4.1). Their exact location, in fact, depends on the imaging parameters. As a result, encoding scheme FAST leads to a dependency of the displacement artifact on the orientation of the imaging axes, as demonstrated in the presented phantom studies (c.f. figure 4.11-4.14). In general, none of the spatial encoding time points are synchronized for encoding scheme FAST, thus, geometrical distortions in the magnitude images may always be present. Due to the proximity between the spatial encoding time points in PE and SS direction, however, these are minimized if the velocity vector has a vanishing component along the RO direction. Furthermore, higher order derivatives of the position of the non-stationary magnetization (e.g. acceleration) cannot be neglected in many applications. This introduces an additional bias of the quantified velocity vector field, which again depends on the orientation of the imaging axes (c.f. figure 4.15+4.16). In summary, encoding scheme FAST has the advantage of being the fastest encoding scheme, but simultaneously suffers from the dependency of the displacement artifact on the orientation of the imaging axes. This dependency massively complicates the reproducibility of measurements, which are carried out with this scheme.

Encoding scheme ECHO, in contrast, is explicitly designed to synchronize all spatial encoding time points at the center of the echo (c.f. figure 4.2). Therefore, no geometrical distortions in the magnitude images are produced. This was experimentally confirmed in all phantom experiments. At the same time, however, the spatial encoding time points do not coincide with the velocity encoding time points, leading to a bias in the quantified velocity vector field in the presence of higher orders of motion (c.f. figure 4.15+4.16). In clinical cases, this may become apparent in pathologies such as a stenosis. The advantage of encoding scheme ECHO, however, is that the associated displacement artifacts are independent of the orientation of the imaging axes. A typical application example would,

therefore, be 4D flow imaging of the aorta in a sagittal orientation. In this case, the RO direction cannot be aligned orthogonal to the velocity, due to limitations of the total acquisition time. In this case, the other two encoding schemes could lead to substantial geometrical distortions.

Last, a synchronization of the spatial velocity encoding time points in PE and SS direction with the isophase point of the RF pulse can be achieved with encoding scheme ISO (c.f. figure 4.3). Similar to encoding scheme FAST, this leads to a dependency of the displacement artifacts on the orientation of the imaging axes. In the special case of a vanishing velocity vector component along the RO direction, however, encoding scheme ISO produces images free of geometrical distortions (c.f. figure 4.11-4.16). Therefore, the use of this encoding scheme is rather limited to specific applications, such as through-plane velocity quantification in slab selective 3D imaging. In this case, any displacement along the SS direction is compensated, while the other schemes would alias moving spins to the opposite side of the slab. A possible clinical target are the carotid arteries, which have been investigated in a transversal oriented 3D volume [59].

In summary, the best suited encoding scheme has to be chosen for each individual measurement. They all have their own advantages and disadvantages, depending on the desired application, whether it is clinical or technical, 2D or 3D, in-plane or through-plane flow. However, in general, the dependency of the displacement artifact on the orientation of the imaging axes poses a practical issue. Patients are often scanned several times, for example to monitor the progression of a disease or the success of a therapy. It is likely that the imaging axes between these measurements are not precisely aligned, leading to a different bias in each of the measurements due to displacement artifacts. This makes it extremely difficult to compare the individual results and may have impact on clinical decisions.

5.1.1 Multi-spoke RF pulses

The expansion of velocity quantification towards multi-spoke excitation might be an important step to improve the characterization of human haemodynamics at UHF. The advantages associated with UHF MRI allow for velocity quantification with improved SNR [9, 10]. This, in turn, can be used either for a faster image acquisition or for an improved spatial resolution.

In the context of multi-spoke excitation and within the small flip angle approximation, the displacement artifact in the final image can be treated as a superposition of the individual artifacts. As a consequence, the spatial encoding time points of each magnetization

subset have to be controlled, which may require additional bipolar gradients between consecutive RF pulses. It is particularly important to apply the same first gradient moment to all magnetization subsets for the central k-space line. Otherwise, velocity-dependent signal modulations are observed, which lead to locally increased velocity noise (c.f. figure 4.10). Besides the synchronization of all spatial encoding time points at the center of the echo, encoding scheme ECHO has the additional advantage that flyback gradients can be used between consecutive slice selection gradients. This significantly shortens the overall excitation duration compared to encoding scheme ISO.

Within the scope of this work, only 2-spoke excitation has been demonstrated, however, these considerations hold true for an arbitrary number of spokes and the corresponding encoding gradients can be calculated, following the provided general solutions. Furthermore, these solutions can be applied to excitation using so-called kT-points [60]. In combination with universal pulses [34], the findings of this work may allow for calibration-free measurements of human haemodynamics at UHF.

Even for multi-spoke RF pulses, the displacement artifacts can be understood and controlled by the different encoding schemes. However, the different displacements of the individual partial magnetizations represent an inherent limitation of the presented technique. This limitation can be overcome by two complementary options. One is to choose a small number of spoke pulses, e.g. two, and the other is to minimize the time interval between these pulses.

Encoding scheme FAST and ECHO are, therefore, with regard to the latter option, preferable to encoding scheme ISO, since they minimize the inter-pulse duration. Furthermore, as demonstrated in this work, asymmetric multi-spoke RF pulses can be used for velocity quantification. These pulses have the potential to significantly shorten the inter-pulse duration compared to conventional sinc-shaped RF pulses, without compromising the velocity quantification (c.f. figure 4.23+4.24 and 4.26). In general, asymmetric pulses are suitable for both, 2D and 3D, acquisitions, even though a slight signal loss may be generated in the 2D case due to the non-zero imaginary part along the slice profile.

The reduction of the number of spoke pulses, in contrast, is independent of the encoding scheme and generally represents a compromise between excitation homogeneity and displacement artifact. For 3 T and for many applications at 7 T, B_1 shimming (single-spoke excitation) is sufficient [61–63]. Certain applications at 7 T [13, 64, 65] or even higher field strengths, such as 9.4 T [66], however, clearly benefit from multi-spoke RF pulses. Especially the imaging of large target regions should be emphasized here [67]. Considering the situation for systems with field strengths above 9.4 T, the use of multi-spoke excitation

may be necessary to obtain satisfactory results at all. The aim of the investigation of the combination of multi-spoke excitation with velocity quantification was, therefore, not to show the improved performance in terms of flip angle homogenization of multi-spoke RF pulses compared to B_1 shimming. Rather, the aim was to investigate velocity encoding and compensation with different encoding schemes when using multi-spoke RF pulses.

The *in vivo* experiments demonstrated an excellent agreement between 2-spoke excitation and B_1 shimming (c.f. figure 4.18+4.19). A quantification of the displacement artifacts, however, was not feasible due to the relatively poor in-plane resolution of $2\text{ mm} \times 2\text{ mm}$. This could be further improved, if navigator-based imaging is used instead of data acquisition only during breath-hold.

5.1.2 VENC optimization

Typically, the velocity noise of a PC measurement is assumed to be proportional to the ratio between the VENC value and the signal-to-noise-ratio ($\sigma_v \sim \frac{VENC}{SNR}$) [68]. This relation has led to increased popularity of multi-VENC methods [69–72] that acquire multiple phase difference images corresponding to multiple VENC values. The high VENC data can then be used to correct for velocity aliasing in the (low noise) low VENC data. However, this theory is based on the assumption that the velocity distribution within a voxel is a DIRAC δ function. This implies that the SNR is independent of the VENC value. Under real conditions, however, and due to the finite resolution of MR images, the velocity distribution can cover a broad spectrum. In this case, as shown in this work (c.f. figure 4.38), the intravoxel velocity distribution has to be taken into account. As a consequence, simply lowering the VENC value, as assumed in multi-VENC methods, does not necessarily result in an improved velocity noise. Indeed, there is a large range, in which the linear relationship between the velocity noise and the VENC value holds true (c.f. figure 4.40A). But below a certain noise-optimal VENC value the SNR loss, due to intravoxel dephasing, leads to an increase in the velocity noise.

The method proposed in this work allows for a determination of noise-optimal VENC values under the consideration of intravoxel velocity distributions. While, this might not be feasible in clinical routine, due to the long acquisition times of FOURIER velocity encoded sequences, it can be used for *in vitro* studies.

The highest noise-optimized VENC values were obtained close to the vessel wall, of up to 30 cm/s (60 cm/s) for symmetric (single-sided) encoding (c.f. figure 4.40+4.41). This can be attributed to the finite resolution of the MR images and the strong spatial velocity gradient at the edge of the vessel. These findings have, for example, implications for WSS

estimation. WSS is derived from velocities close to the vessel wall and is particularly sensitive to noise, because it requires the calculation of spatial derivatives of the velocity vector field. The choice of appropriate VENC values should, therefore, always account for these effects.

5.2 Acceleration quantification

The quantification of the acceleration vector field might be of clinical interest, as it provides valuable functional information [73–75]. Furthermore, the acceleration vector field plays an important role in fundamental fluid mechanics, as it is directly included in the NAVIER-STOKES equation (c.f. left side of equation 2.121). In principle, it is possible to derive the acceleration vector field from a measured velocity vector field, but this approach has limitations. For correct quantification of a 2D acceleration vector field, a 3D velocity vector field has to be acquired. In clinical applications, this might render the acquisition unfeasible. Furthermore, the accuracy of the derived acceleration vector field can be substantially limited by the amplification of the noise of the velocity vector field [76]. Therefore, a direct quantification of the acceleration vector field is desirable.

Since the direct quantification of the acceleration vector field by MRI is similar to velocity quantification, it is prone to the same errors. Any desynchronization between the spatial encoding time points of the imaging axes may result in geometrical distortions. Similarly, any desynchronization between the acceleration encoding time points and the spatial encoding time points leads to a bias in the quantified acceleration, if higher orders of motion (e.g. jerk) cannot be neglected.

The presented extension of encoding scheme ECHO for acceleration quantification enables measurements free of geometrical distortions, by synchronizing all spatial encoding time points at the center of the echo. At the same time, however, this method is susceptible to errors in the quantified acceleration vector field, which are induced by higher orders of motion (c.f. figure 4.42+4.43).

The newly proposed acceleration-encoded SYNC SPI sequence, however, synchronizes all encoding time points of all three imaging axis. This sequence provides gold-standard-like acceleration quantification, similar to velocity quantification with the velocity-encoded SYNC SPI sequence proposed by Bruschewski and colleagues [49]. Due to its nature of being an SPI sequence, the long acquisition time prohibits in vivo applications and, therefore, conventional sequences have to be applied in this case.

Here, the feasibility of direct acceleration quantification in the human aorta at 7T in combination with B_1 phase shimming to achieve a homogeneous flip angle distribution

was successfully shown. The directly measured acceleration vector field shows a substantially improved image quality compared to the acceleration derived from the measured velocity vector field (c.f. figure 4.44). Furthermore, the convective acceleration cannot be completely calculated from 2D velocity data, leading to substantial differences between directly measured and derived acceleration values. For an exact determination of the acceleration vector field, the direct measurement is, therefore, preferable to derivation from measured velocity data.

The direct measurement of the acceleration vector field provides access to an additional haemodynamic parameter that might be of clinical interest. Furthermore, the acceleration-encoded SYNC SPI sequence allows for accurate quantification of the acceleration vector field for *in vitro* studies. For *in vivo* applications, the aforementioned encoding scheme ECHO should be used.

5.3 Wall shear stress estimation

WSS is a fluid mechanical parameter that is attracting increasing clinical interest. The estimation of WSS based on PC MRI data has, therefore, been subject of several studies. Pertersson et al. [77] investigated the accuracy of WSS estimation using numerical simulations to systematically evaluate the influence of different parameters, such as VENC value, spatial resolution, and different fitting routines. Most importantly, the aforementioned study pointed out that the estimated WSS might not even be monotonically related to the actual WSS. However, distinguishing areas of low and moderate WSS may be feasible. Furthermore, several studies have shown that an increase in spatial resolution improves the accuracy of the WSS estimation, therefore, the PC data should be acquired with the highest possible resolution [10, 51, 77]. While previous studies have focused on the impact of post-processing steps or imaging parameters on the WSS estimation, studies focusing on the influence of errors in the measured velocity vector field are still needed.

Similar to the results of the velocity vector fields acquired with different encoding schemes, substantial differences between these schemes are observed with respect to the WSS estimation. Importantly, any bias in the velocity data propagates into the estimated WSS. As a consequence, WSS estimations based on velocity data acquired with encoding scheme ECHO are independent of the orientation of the imaging axes (c.f. figure 4.33). For encoding scheme FAST, in contrast, a strong influence of the orientation of the imaging axes can be observed (c.f. figure 4.34). This does not only include an underestimation of peak WSS, but also a change of the WSS pattern. The latter might be most critical for clinical decision making, as WSS patterns are linked to initiation of atherosclerosis

and induce the development of atherosclerotic plaques [78]. In comparison to the gold standard SYNC SPI measurement, however, disadvantages of encoding scheme ECHO become also apparent. Within the stenosis, encoding scheme ECHO fails to provide correct WSS values. In this case, if the vessel geometry permits, encoding scheme FAST, with an orientation of the RO axis orthogonal to the velocity within the stenosis, would be the best choice.

WSS cannot be used as an absolute quantitative parameter, because too many variables have an influence on the quantified values. However, the differentiability of regions with low and high WSS seems to be feasible [77] and can potentially provide important information. In this context, it is of utmost importance that the WSS pattern is reproducible. Therefore, encoding scheme ECHO should be used, whenever the long acquisition times of the SYNC SPI sequence render its application unfeasible.

5.4 Reynolds stress tensor quantification

Within this work, the RST has been successfully quantified in a well-known fluid dynamic test case with a REYNOLDS number of 60,000 that produces strong anisotropic turbulence. The corresponding RST, therefore, covers a large range of values. The approach used here differed from previous studies of turbulent flow [17–20], as multiple m_1 values were chosen. For intravoxel-velocity-standard-deviation (IVSD) mapping, i.e. the quantification of the RST’s diagonal elements, it has been reported that the choice of m_1 influences the quantified values [19]. Low m_1 values lead to an insignificant signal loss, while large m_1 values result in strong signal dephasing such that magnitude images reflect the noise floor. In the latter case, the RICIAN nature of the magnitude noise is the main source of error. The same holds true for the quantification of the full RST. Quantification of the full RST, however, inherently requires a large dynamic range, as the normal stresses are typically substantially higher than the shear stresses.

The results obtained by acquiring ICOSA6-encoded MRI data with multiple m_1 values indicate, in analogy to IVSD mapping, that RST quantification is highly susceptible to the applied m_1 value (c.f. figure 4.47-4.49). Due to the inherent large dynamic range of the full RST, multiple m_1 value are necessary to correctly quantify all components of the RST, not only in this particular test case. While single m_1 values might be sufficient to correctly quantify some components of the RST in certain regions of the studied flow, they cannot cover the complete dynamic range needed for an accurate quantification of the complete RST. Furthermore, the RICIAN nature of the magnitude noise has to be taken into account. Here, this was done by excluding data points from the fit routine

that did not exceed a certain magnitude threshold. In principle, however, the noise level of the MR images could also be estimated and included into the fit model.

To estimate the proposed method's accuracy, additional data, either from simulations or other reference measurements, would be needed. Additionally, these would allow to find systematic errors in the presented data. Simulation data could be obtained from large eddy simulations [79], a mathematical model for turbulence used in computational fluid dynamics (CFD). Additional experimental data could be acquired with laser doppler velocimetry (LDV). In principle, both methods are able to quantify the full RST.

Due to the long acquisition times, the measurements performed within the scope of this work are unfeasible for in vivo applications. A reduction of the number of acquired m_1 values could be used to shorten the measurement time. However, the possible associated loss of accuracy of the quantification of the RST would have to be investigated in further studies. In the context of technical applications, however, MRI-based quantification of the RST seems to be a promising tool, especially compared to alternative methods, such as LDV with measurement times in the order of weeks or months.

5.5 Outlook

Since the first in vivo measurements of haemodynamics by means of MRI were conducted in the early 1980s [4–6], the underlying techniques have been continuously further developed. Today, a multitude of different fluid mechanical properties can be quantified using MRI. This thesis contributed to overcome still persistent limitations of MR-based quantification of fluid mechanical properties and to further develop the underlying techniques.

The displacement artifact for single- and multi-spoke excitation has been evaluated for CARTESIAN imaging. In the future, it will be interesting to transfer these insights towards non-CARTESIAN imaging methods. Radial acquisitions, for example, could offer the additional benefit of inherent self-navigation, allowing for free-breathing acquisitions with high efficiency. The displacement artifacts, associated with such k-space trajectories, however, should be carefully evaluated.

With regard to in vivo studies, it remains to be seen whether the influence of displacement artifacts for both, velocity and acceleration quantification, proves to be problematic. Presumably, this will gain increased interest as soon as higher field strengths, which allow higher spatial resolutions, are used more often. For in vivo applications the SPI methods are unfeasible due to their long acquisition times. Therefore, quantification of fluid mechanical parameters in vivo will remain susceptible to errors. Especially, since

these limitations cannot be avoided, it is of utmost importance to fully understand the underlying mechanisms.

The functionality of the acceleration-encoded SYNC SPI sequence was showcased in the rotation phantom. However, it would be of interest to systematically evaluate the performance of this sequence in various settings. In combination with the velocity-encoded SYNC SPI sequence, as described by Bruschewski et al. [49], a competitive toolbox for gold-standard-like quantification of fluid mechanical parameters in vitro could be established to evaluate other measurement techniques or CFD simulations.

Concerning the quantification of the RST, further evaluation is needed. Especially, a quantitative comparison between the presented technique and other methods is essential to confirm the accuracy and to eliminate potential systematic errors. Furthermore, it was already shown in the 1990s that, in principle, the quantification of auto-correlation times of turbulent flow is possible [80, 81]. It might be worthwhile to take up these methods again and combine them with state-of-the-art techniques, as presented in this work.

This thesis is a contribution to the versatile research fields of MRI and fluid mechanics. I am convinced that the presented developments will impact applications in clinical routine as well as in basic research.

6 Appendix

6.1 Abbreviations

ACQ	acquisition
AENC	acceleration encoding sensitivity
BWT	bandwidth-time-product
CFD	computational fluid dynamics
CV	coefficient of variation
FID	Free Induction Decay
FOV	field of view
FWHM	full width at half maximum
GRAPPA	generalized autocalibrating partial parallel acquisition
GRT	gradient raster time
IDEA	Integrated Development Environment for Applications
IVSD	intravoxel-velocity-standard-deviation
LDV	laser doppler velocimetry
MR	magnetic resonance
MRI	magnetic resonance imaging
NMR	nuclear magnetic resonance
PC	phase contrast
PE	phase encoding
pTx	parallel transmission
RF	radio frequency
RO	readout
ROI	region of interest
RST	REYNOLDS stress tensor
SENSE	sensitivity encoding
SLR	SHINNAR-LE ROUX
SNR	signal-to-noise-ratio
SPI	single-point imaging
SS	slice selection
SYNC SPI	synchronized single-point imaging
TE	echo time

TR	repetition time
UHF	ultra high field
VENC	velocity encoding sensitivity
WSS	wall shear stress

6.2 Publications

Parts of this work are published in the following publications:

Journal Publications

S. Schmidt, S. Flassbeck, P. Bachert, M. E. Ladd, and S. Schmitter. Velocity encoding and velocity compensation for multi-spoke RF excitation. *Magnetic Resonance Imaging*, 66:69-85, 2020.

S. Schmidt, S. Flassbeck, P. Bachert, M. E. Ladd, and S. Schmitter. On the impact of the displacement artifact on wall shear stress estimation. *Manuscript in preparation*.

Conference Talks

S. Schmidt, S. Flassbeck, M. Breithaupt, P. Bachert, M. E. Ladd and S. Schmitter. Velocity encoded and compensated mutli-spoke RF pulses for flow quantification at ultra-high fields. *ISMRM 25th Annual Meeting*, 2017.

S. Schmidt, S. Flassbeck, M. E. Ladd and S. Schmitter. On the point of gradient moment expansion for multi-spoke RF pulses. *ISMRM 26th Annual Meeting*, 2018.

S. Schmidt, S. Flassbeck, M. E. Ladd and S. Schmitter. Acceleration mapping in the human aorta at 7T. *31st Annual MR Angiography Conference*, 2019.

S. Schmidt, S. Flassbeck, M. E. Ladd and S. Schmitter. Velocity encoded/compensated asymmetric multi-spoke RF pulses. *ISMRM 28th Annual Meeting*, 2020.

Conference Posters

S. Schmidt, S. Flassbeck, M. E. Ladd and S. Schmitter. On the influence of intravoxel velocity distributions on the noise of phase contrast velocimetry. *ISMRM 26th Annual Meeting*, 2018.

S. Schmidt, S. Flassbeck, M. E. Ladd and S. Schmitter. On the dynamic range of Reynolds stress tensor quantification. *ISMRM 28th Annual Meeting*, 2020.

Further scientific contributions are listed below:

Journal Publications

J. Emmerich, S. Flassbeck, **S. Schmidt**, P. Bachert, M. E. Ladd, and S. Straub. Rapid and accurate dictionary-based T2 mapping from multi-echo turbo spin echo data at 7 Tesla. *Journal of Magnetic Resonance Imaging*, 49(5):1253-1262, 2019.

S. Flassbeck, **S. Schmidt**, P. Bachert, M. E. Ladd, and S. Schmitter. Flow MR fingerprinting. *Magnetic Resonance in Medicine*, 81(4):2536-2550, 2019.

C. Wink, G. Ferrazzi, J. P. Bassenge, S. Flassbeck, **S. Schmidt**, T. Schaeffter, and S. Schmitter. 4D flow imaging with 2D-selective excitation. *Magnetic Resonance in Medicine*, 82(3):886-900, 2019.

A. Vali, S. Schmitter, L. Ma, S. Flassbeck, **S. Schmidt**, M. Markl, and S. Schnell. Development of a rotation phantom for phase contrast MRI sequence validation and quality control. *Manuscript submitted for publication*.

Conference Talks

S. Schmidt, S. Flassbeck, M. Breithaupt, M. E. Ladd, and S. Schmitter. Simultaneous multi-VENC imaging. *ISMRM 25th Annual Meeting*, 2017.

Conference Posters

S. Flassbeck, **S. Schmidt**, M. Breithaupt, P. Bachert, M. E. Ladd, and S. Schmitter. Quantification of flow by magnetic resonance fingerprinting. *ISMRM 25th Annual Meeting*, 2017.

S. Flassbeck, **S. Schmidt**, M. Breithaupt, P. Bachert, M. E. Ladd, and S. Schmitter. On the influence of intra-voxel dephasing in FISP-MRF with variable repetition time. *ISMRM 25th Annual Meeting*, 2017.

S. Flassbeck, **S. Schmidt**, M. E. Ladd, and S. Schmitter. On the impact of heart rate variability in flow-MRF. *ISMRM MRF-Workshop*, 2017.

S. Flassbeck, **S. Schmidt**, M. E. Ladd, and S. Schmitter. Optimization of the flow encoding pattern under consideration of spatio-temporal velocity gradients in flow-MR fingerprinting. *ISMRM 26th Annual Meeting*, 2018.

C. Wink, G. Ferrazzi, J. P. Bassenge, S. Flassbeck, **S. Schmidt**, T. Schaeffter, and S. Schmitter. 4D flow imaging with reduced field-of-excitation. *ISMRM 26th Annual Meeting*, 2018.

S. Schmidt, S. Flassbeck, M. E. Ladd, and S. Schmitter. Simultaneous multi-VENC imaging with dual-echo acquisition. *30th Annual MR Angiography Conference*, 2018.

S. Flassbeck, **S. Schmidt**, M. E. Ladd, and S. Schmitter. Flow-MRF: a novel way of quantifying blood velocities in combination with tissue relaxation parameters. *30th Annual MR Angiography Conference*, 2018.

S. Flassbeck, **S. Schmidt**, M. E. Ladd, and S. Schmitter. Reynolds stress tensor quantification using a flow-MRF approach. *ISMRM 27th Annual Meeting*, 2019.

C. Wink, **S. Schmidt**, J. P. Bassenge, S. Szermer, G. Ferrazzi, B. Ittermann, T. Schaeffter, and S. Schmitter. On the effective center of excitation and the point of gradient moment expansion for 2D-selective excitation in the presence of flow. *ISMRM 27th Annual Meeting*, 2019.

A. Vali, S. Schmitter, L. Ma, X. Huang, S. Flassbeck, **S. Schmidt**, M. Markl, and S. Schnell. Phantom for phase-contrast MRI sequence validation and quality control. *ISMRM 27th Annual Meeting*, 2019.

S. Flassbeck, **S. Schmidt**, M. E. Ladd, and S. Schmitter. Initial results of Reynolds stress tensor quantification using flow-MRF. *31st Annual MR Angiography Conference*, 2019.

M. Bruschewski, **S. Schmidt**, K. John, S. Schmitter, and S. Grundmann. Reynolds stress tensor quantification using magnetic resonance velocimetry - Focus on accuracy and dynamic range. *submitted to 20th International Symposium on Applications of Laser and Imaging Techniques to Fluid Mechanics*, 2020.

Bibliography

- [1] World Health Organization Geneva. Global Health Estimates 2016: Deaths by Cause, Age, Sex, by Country and by Region. 2018.
- [2] H. Y. Carr and E. M. Purcell. Effects of Diffusion on Free Precession in Nuclear Magnetic Resonance Experiments. *Phys. Rev.*, 94:630–638, 1954.
- [3] E. L. Hahn. Detection of sea-water motion by nuclear precession. *Journal of Geophysical Research (1896-1977)*, 65(2):776–777, 1960.
- [4] P. R. Moran. A flow velocity zeugmatographic interlace for NMR imaging in humans. *Magnetic Resonance Imaging*, 1(4):197 – 203, 1982.
- [5] P. Van Dijk. Direct Cardiac NMR Imaging of Heart Wall and Blood Flow Velocity. *Journal of Computer Assisted Tomography*, 8(3):429–436, 1984.
- [6] D. J. Bryant, J. A. Payne, D. N. Firmin, and D. B. Longmore. Measurement of Flow with NMR Imaging Using a Gradient Pulse and Phase Difference Technique. *Journal of Computer Assisted Tomography*, 8(4):588–593, 1984.
- [7] G. L. Nayler, D. N. Firmin, and D. B. Longmore. Blood Flow Imaging by Cine Magnetic Resonance. *Journal of Computer Assisted Tomography*, 10(5):715–722, 1986.
- [8] M. Markl, A. Frydrychowicz, S. Kozerke, M. Hope, and O. Wieben. 4D flow MRI. *Journal of Magnetic Resonance Imaging*, 36(5):1015–1036, 2012.
- [9] A. T. Hess, M. M. Bissell, N. A. B. Ntusi, A. J. M. Lewis, E. M. Tunnicliffe, A. Greiser, A. F. Stalder, J. M. Francis, S. G. Myerson, S. Neubauer, and M. D. Robson. Aortic 4D flow: Quantification of signal-to-noise ratio as a function of field strength and contrast enhancement for 1.5T, 3T, and 7T. *Magnetic Resonance in Medicine*, 73(5):1864–1871, 2015.
- [10] P. van Ooij, J. J. M. Zwanenburg, F. Visser, C. B. Majoie, E. vanBavel, J. Hendrikse, and A. J. Nederveen. Quantification and visualization of flow in the Circle of Willis: Time-resolved three-dimensional phase contrast MRI at 7 T compared with 3 T. *Magnetic Resonance in Medicine*, 69(3):868–876, 2013.

- [11] S. Schmitter, S. Schnell, K. Uğurbil, M. Markl, and P.-F. Van de Moortele. Towards high-resolution 4D flow MRI in the human aorta using kt-GRAPPA and B1+ shimming at 7T. *Journal of Magnetic Resonance Imaging*, 44(2):486–499, 2016.
- [12] S. Saekho, C. Yip, D. C. Noll, F. E. Boada, and V. A. Stenger. Fast-kz three-dimensional tailored radiofrequency pulse for reduced B1 inhomogeneity. *Magnetic Resonance in Medicine*, 55(4):719–724, 2006.
- [13] K. Setsompop, V. Alagappan, B. Gagoski, T. Witzel, J. Polimeni, A. Potthast, F. Hebrank, U. Fontius, F. Schmitt, L. L. Wald, and E. Adalsteinsson. Slice-selective RF pulses for in vivo B inhomogeneity mitigation at 7 tesla using parallel RF excitation with a 16-element coil. *Magnetic Resonance in Medicine*, 60(6):1422–1432, 2008.
- [14] M. A. Ertürk, X. Wu, Y. Eryaman, P.-F. Van de Moortele, E. J. Auerbach, R. L. Lagore, L. DelaBarre, J. T. Vaughan, K. Uğurbil, G. Adriany, and G. J. Metzger. Toward imaging the body at 10.5 tesla. *Magnetic Resonance in Medicine*, 77(1):434–443, 2017.
- [15] D. G. Nishimura, J. I. Jackson, and J. M. Pauly. On the nature and reduction of the displacement artifact in flow images. *Magnetic Resonance in Medicine*, 22(2):481–492, 1991.
- [16] L. R. Frank, A. P. Crawley, and R. B. Buxton. Elimination of oblique flow artifacts in magnetic resonance imaging. *Magnetic Resonance in Medicine*, 25(2):299–307, 1992.
- [17] P. Dyverfeldt, A. Sigfridsson, J.-P. E. Kvitting, and T. Ebbers. Quantification of intravoxel velocity standard deviation and turbulence intensity by generalizing phase-contrast MRI. *Magnetic Resonance in Medicine*, 56(4):850–858, 2006.
- [18] P. Dyverfeldt, J.-P. E. Kvitting, A. Sigfridsson, J. Engvall, A. F. Bolger, and T. Ebbers. Assessment of fluctuating velocities in disturbed cardiovascular blood flow: In vivo feasibility of generalized phase-contrast MRI. *Journal of Magnetic Resonance Imaging*, 28(3):655–663, 2008.
- [19] P. Dyverfeldt, R. Gårdhagen, A. Sigfridsson, M. Karlsson, and T. Ebbers. On MRI turbulence quantification. *Magnetic Resonance Imaging*, 27(7):913 – 922, 2009.
- [20] H. Haraldsson, S. Kefayati, S. Ahn, P. Dyverfeldt, J. Lantz, M. Karlsson, G. Laub, T. Ebbers, and D. Saloner. Assessment of Reynolds stress components and turbulent pressure loss using 4D flow MRI with extended motion encoding. *Magnetic Resonance in Medicine*, 79(4):1962–1971, 2018.

-
- [21] F. Bloch, W. W. Hansen, and M. Packard. Nuclear Induction. *Physical Review*, 69(3-4):127–127, 1946.
- [22] P. B. Roemer, W. A. Edelstein, C. E. Hayes, S. P. Souza, and O. M. Mueller. The NMR phased array. *Magnetic Resonance in Medicine*, 16(2):192–225, 1990.
- [23] K. P. Pruessmann, M. Weiger, M. B. Scheidegger, and P. Boesiger. SENSE: Sensitivity encoding for fast MRI. *Magnetic Resonance in Medicine*, 42(5):952–962, 1999.
- [24] M. A. Griswold, P. M. Jakob, R. M. Heidemann, M. Nittka, V. Jellus, J. Wang, B. Kiefer, and A. Haase. Generalized autocalibrating partially parallel acquisitions (GRAPPA). *Magnetic Resonance in Medicine*, 47(6):1202–1210, 2002.
- [25] J. Pauly, D. Nishimura, and A. Macovski. A k-space analysis of small-tip-angle excitation. *Journal of Magnetic Resonance (1969)*, 81(1):43 – 56, 1989.
- [26] M. Shinnar, S. Eleff, H. Subramanian, and J. S. Leigh. The synthesis of pulse sequences yielding arbitrary magnetization vectors. *Magnetic Resonance in Medicine*, 12(1):74–80, 1989.
- [27] M. Shinnar, L. Bolinger, and J. S. Leigh. The use of finite impulse response filters in pulse design. *Magnetic Resonance in Medicine*, 12(1):81–87, 1989.
- [28] M. Shinnar, L. Bolinger, and J. S. Leigh. The synthesis of soft pulses with a specified frequency response. *Magnetic Resonance in Medicine*, 12(1):88–92, 1989.
- [29] M. Shinnar and J. S. Leigh. The application of spinors to pulse synthesis and analysis. *Magnetic Resonance in Medicine*, 12(1):93–98, 1989.
- [30] J. Pauly, P. Le Roux, D. Nishimura, and A. Macovski. Parameter relations for the Shinnar-Le Roux selective excitation pulse design algorithm (NMR imaging). *IEEE Transactions on Medical Imaging*, 10(1):53–65, 1991.
- [31] T. Truong, D. W. Chakeres, D. Q. Beversdorf, D. W. Scharre, and P. Schmalbrock. Effects of static and radiofrequency magnetic field inhomogeneity in ultra-high field magnetic resonance imaging. *Magnetic Resonance Imaging*, 24(2):103 – 112, 2006.
- [32] W. Grissom, C Yip, Z Zhang, V. A. Stenger, J. A. Fessler, and D. C. Noll. Spatial domain method for the design of RF pulses in multicoil parallel excitation. *Magnetic Resonance in Medicine*, 56(3):620–629, 2006.

- [33] D. H. Y. Tse, C. J. Wiggins, and B. A. Poser. Estimating and eliminating the excitation errors in bipolar gradient composite excitations caused by radiofrequency-gradient delay: Example of bipolar spokes pulses in parallel transmission. *Magnetic Resonance in Medicine*, 78(5):1883–1890, 2017.
- [34] V. Gras, A. Vignaud, A. Amadon, F. Mauconduit, D. Le Bihan, and N. Boulant. New method to characterize and correct with sub- μ s precision gradient delays in bipolar multispoke RF pulses. *Magnetic Resonance in Medicine*, 78(6):2194–2202, 2017.
- [35] R. J. Sutherland and J. M. S. Hutchison. Three-dimensional NMR imaging using selective excitation. *Journal of Physics E: Scientific Instruments*, 11(1):79–83, 1978.
- [36] O. P. Simonetti, R. E. Wendt III, and J. L. Duerk. Significance of the point of expansion in interpretation of gradient moments and motion sensitivity. *Journal of Magnetic Resonance Imaging*, 1(5):569–577, 1991.
- [37] J. L. Duerk, O. P. Simonetti, G. C. Hurst, and D. A. Finelli. Experimental confirmation of phase encoding of instantaneous derivatives of position. *Magnetic Resonance in Medicine*, 32(1):77–87, 1994.
- [38] V. J. Wedeen, R. E. Wendt III, and M. Jerosch-Herold. Motional phase artifacts in fourier transform MRI. *Magnetic Resonance in Medicine*, 11(1):114–120, 1989.
- [39] D. N. Firmin, G. L. Nayler, P. J. Kilner, and D. B. Longmore. The application of phase shifts in NMR for flow measurement. *Magnetic Resonance in Medicine*, 14(2):230–241, 1990.
- [40] L. R. Frank and R. B. Buxton. Distortions from curved flow in magnetic resonance imaging. *Magnetic Resonance in Medicine*, 29(1):84–93, 1993.
- [41] Marc Kouwenhoven, Mark B. M. Hofman, and Michiel Sprenger. Motion Induced Phase Shifts in MR: Acceleration Effects in Quantitative Flow Measurements—A Reconsideration. *Magnetic Resonance in Medicine*, 33(6):766–777, 1995.
- [42] P. G. Walker, G. B. Cranney, M. B. Scheidegger, G. Waseleski, G. M. Pohost, and A. P. Yoganathan. Semiautomated method for noise reduction and background phase error correction in MR phase velocity data. *Journal of Magnetic Resonance Imaging*, 3(3):521–530, 1993.
- [43] M. A. Bernstein, X. J. Zhou, J. A. Polzin, K. F. King, A. Ganin, N. J. Pelc, and G. H. Glover. Concomitant gradient terms in phase contrast MR: Analysis and correction. *Magnetic Resonance in Medicine*, 39(2):300–308, 1998.

- [44] K. M. Hasan, D. L. Parker, and A. L. Alexander. Comparison of gradient encoding schemes for diffusion-tensor MRI. *Journal of Magnetic Resonance Imaging*, 13(5):769–780, 2001.
- [45] F. Durst. *Grundlagen der Strömungsmechanik*. Springer, 2006.
- [46] S. Orzada, H. H. Quick, M. E. Ladd, A. Bahr, T. Bolz, and P. Yazdanbakhsh. A flexible 8-channel transmit/receive body coil for 7 T human imaging. *In Proceedings of the 17th Annual Meeting of the ISMRM, Honolulu, Hawaii, USA*, 2009.
- [47] S. H. G. Rietsch, H. H. Quick, and S. Orzada. Impact of different meander sizes on the RF transmit performance and coupling of microstrip line elements at 7 T. *Medical Physics*, 42(8):4542–4552, 2015.
- [48] M. A. Bernstein, A. Shimakawa, and N. J. Pelc. Minimizing TE in moment-nulled or flow-encoded two-and three-dimensional gradient-echo imaging. *Journal of Magnetic Resonance Imaging*, 2(5):583–588, 1992.
- [49] M. Bruschi, H. Kolkmann, K. John, and S. Grundmann. Phase-contrast single-point imaging with synchronized encoding: a more reliable technique for in vitro flow quantification. *Magnetic Resonance in Medicine*, 81(5):2937–2946, 2019.
- [50] P.-F. Van de Moortele and K. Ugurbul. Very fast multi channel B1 calibration at high field in the small flip angle regime. *In Proceedings of the 17th Annual Meeting of the ISMRM, Honolulu, Hawaii, USA*, 2009.
- [51] W. V. Potters, P. van Ooij, H. Marquering, E. vanBavel, and A. J. Nederveen. Volumetric arterial wall shear stress calculation based on cine phase contrast MRI. *Journal of Magnetic Resonance Imaging*, 41(2):505–516, 2015.
- [52] S. Schmidt, S. Flassbeck, P. Bachert, M. E. Ladd, and S. Schmitter. Velocity encoding and velocity compensation for multi-spoke RF excitation. *Magnetic Resonance Imaging*, 66:69–85, 2020.
- [53] S. Schmidt, S. Flassbeck, M. Breithaupt, P. Bachert, M. E. Ladd, and S. Schmitter. Velocity encoded and compensated multi-spoke RF pulses for flow quantification at ultra-high fields. *In Proceedings of the 25th Annual Meeting of the ISMRM, Honolulu, Hawaii, USA*, 2017.
- [54] S. Schmidt, S. Flassbeck, M. E. Ladd, and S. Schmitter. On the point of gradient moment expansion for multi-spoke RF pulses. *In Proceedings of the 26th Annual Meeting of the ISMRM, Paris, France*, 2018.

- [55] S. Schmidt, S. Flassbeck, M. E. Ladd, and S. Schmitter. On the influence of intravoxel velocity distributions on the noise of phase contrast velocimetry. *In Proceedings of the 26th Annual Meeting of the ISMRM, Paris, France, 2018.*
- [56] S. Schmidt, S. Flassbeck, M. E. Ladd, and S. Schmitter. Acceleration mapping in the human aorta at 7T. *In Proceedings of the 31st Annual MR Angiography Conference, Nantes, France, 2019.*
- [57] S. Schmidt, S. Flassbeck, M. E. Ladd, and S. Schmitter. Velocity encoded/compensated asymmetric multi-spoke RF pulses. *In Proceedings of the 28th Annual Meeting of the ISMRM, Sydney, Australia, 2020.*
- [58] S. Schmidt, S. Flassbeck, M. E. Ladd, and S. Schmitter. On the dynamic range of Reynolds stress tensor quantification. *In Proceedings of the 28th Annual Meeting of the ISMRM, Sydney, Australia, 2020.*
- [59] A. Harloff, F. Albrecht, J. Spreer, A. F. Stalder, J. Bock, A. Frydrychowicz, J. Schöllhorn, A. Hetzel, M. Schumacher, J. Hennig, and M. Markl. 3D blood flow characteristics in the carotid artery bifurcation assessed by flow-sensitive 4D MRI at 3T. *Magnetic Resonance in Medicine*, 61(1):65–74, 2009.
- [60] M. A. Cloos, N. Boulant, M. Luong, G. Ferrand, E. Giacomini, D. Le Bihan, and A. Amadon. kT-points: Short three-dimensional tailored RF pulses for flip-angle homogenization over an extended volume. *Magnetic Resonance in Medicine*, 67(1):72–80, 2012.
- [61] A. T. Curtis, K. M. Gilbert, L. M. Klassen, J. S. Gati, and R. S. Menon. Slice-by-slice B1+ shimming at 7 T. *Magnetic Resonance in Medicine*, 68(4):1109–1116, 2012.
- [62] W. Mao, M. B. Smith, and C. M. Collins. Exploring the limits of RF shimming for high-field MRI of the human head. *Magnetic Resonance in Medicine*, 56(4):918–922, 2006.
- [63] G. J. Metzger, E. J. Auerbach, C. Akgun, J. Simonson, X. Bi, K. Uğurbil, and P.-F. van de Moortele. Dynamically applied B1+ shimming solutions for non-contrast enhanced renal angiography at 7.0 tesla. *Magnetic Resonance in Medicine*, 69(1):114–126, 2013.
- [64] S. Schmitter, L. DelaBarre, X. Wu, A. Greiser, D. Wang, E. J. Auerbach, J. T. Vaughan, K. Uğurbil, and P.-F. Van de Moortele. Cardiac imaging at 7 tesla: Single-

- and two-spoke radiofrequency pulse design with 16-channel parallel excitation. *Magnetic Resonance in Medicine*, 70(5):1210–1219, 2013.
- [65] S. Schmitter, X. Wu, E. J. Auerbach, G. Adriany, J. Pfeuffer, M. Hamm, K. Uğurbil, and P.-F. Van de Moortele. Seven-tesla time-of-flight angiography using a 16-channel parallel transmit system with power-constrained 3-dimensional spoke radiofrequency pulse design. *Investigative Radiology*, 49(5):314–325, 2014.
- [66] X. Wu, G. Adriany, K. Uğurbil, and P.-F. Van de Moortele. Correcting for Strong Eddy Current Induced B₀ Modulation Enables Two-Spoke RF Pulse Design with Parallel Transmission: Demonstration at 9.4T in the Human Brain. *PLOS ONE*, 8(10):1–7, 2013.
- [67] X. Wu, S. Schmitter, E. J. Auerbach, K. Uğurbil, and P.-F. Van de Moortele. Mitigating transmit B₁ inhomogeneity in the liver at 7T using multispoke parallel transmit RF pulse design. *Quantitative Imaging in Medicine and Surgery*, 4(1):4–10, 2014.
- [68] A. T. Lee, G. Bruce Pike, and N. J. Pelc. Three-Point Phase-Contrast Velocity Measurements with Increased Velocity-to-Noise Ratio. *Magnetic Resonance in Medicine*, 33(1):122–126, 1995.
- [69] E. J. Nett, K. M. Johnson, A. Frydrychowicz, A. M. Del Rio, E. Schrauben, C. J. Francois, and O. Wieben. Four-dimensional phase contrast MRI with accelerated dual velocity encoding. *Journal of Magnetic Resonance Imaging*, 35(6):1462–1471, 2012.
- [70] H. Ha, G. B. Kim, J. Kweon, Y.-H. Kim, N. Kim, D. H. Yang, and S. J. Lee. Multi-VENC acquisition of four-dimensional phase-contrast MRI to improve precision of velocity field measurement. *Magnetic Resonance in Medicine*, 75(5):1909–1919, 2016.
- [71] F. M. Callaghan, R. Kozor, A. G. Sherrah, M. Vallyly, D. Celermajer, G. A. Figtree, and S. M. Grieve. Use of multi-velocity encoding 4D flow MRI to improve quantification of flow patterns in the aorta. *Journal of Magnetic Resonance Imaging*, 43(2):352–363, 2016.
- [72] A. Schnell, A. A. Ansari, C. Wu, J. Garcia, I. G. Murphy, O. A. Rahman, A. A. Rahsepar, M. Aristova, J. D. Collins, J. C. Carr, and M. Markl. Accelerated dual-enc 4D flow MRI for neurovascular applications. *Journal of Magnetic Resonance Imaging*, 46(1):102–114, 2017.

- [73] J.-P. Tasu, E. Mousseaux, A. Delouche, C. Oddou, O. Jolivet, and J. Bittoun. Estimation of pressure gradients in pulsatile flow from magnetic resonance acceleration measurements. *Magnetic Resonance in Medicine*, 44(1):66–72, 2000.
- [74] F. Staehle, B. A. Jung, S. Bauer, J. Leupold, J. Bock, R. Lorenz, D. Föll, and M. Markl. Three-directional acceleration phase mapping of myocardial function. *Magnetic Resonance in Medicine*, 65(5):1335–1345, 2011.
- [75] A. J. Barker, F. Staehle, J. Bock, B. A. Jung, and M. Markl. Analysis of complex cardiovascular flow with three-component acceleration-encoded MRI. *Magnetic Resonance in Medicine*, 67(1):50–61, 2012.
- [76] F. Balleux-Buyens, O. Jolivet, J. Bittoun, and A. Herment. Velocity encoding versus acceleration encoding for pressure gradient estimation in MR haemodynamic studies. *Physics in Medicine and Biology*, 51(19):4747–4758, 2006.
- [77] S. Petersson, P. Dyverfeldt, and T. Ebbers. Assessment of the accuracy of MRI wall shear stress estimation using numerical simulations. *Journal of Magnetic Resonance Imaging*, 36(1):128–138, 2012.
- [78] C. Cheng, D. Tempel, R. van Haperen, A. van der Baan, F. Grosveld, M. J. A. P. Daemen, R. Krams, and R. de Crom. Atherosclerotic Lesion Size and Vulnerability Are Determined by Patterns of Fluid Shear Stress. *Circulation*, 113(23):2744–2753, 2006.
- [79] X. Gloerfelt and P. Cinnella. Large Eddy Simulation Requirements for the Flow over Periodic Hills. *Flow, Turbulence and Combustion*, 103:55–91, 2019.
- [80] J.-H. Gao and J. C. Gore. Turbulent flow effects on NMR imaging: Measurement of turbulent intensity. *Medical Physics*, 18(5):1045–1051, 1991.
- [81] J. C. Gatenby and J. C. Gore. Mapping of Turbulent Intensity by Magnetic Resonance Imaging. *Journal of Magnetic Resonance, Series B*, 104(2):119 – 126, 1994.

Danksagung

Mein Dank gilt allen Personen, die mich auf dem Weg zu meiner Promotion begleitet und unterstützt haben.

Zunächst vielen Dank an Sie, Herr Prof. Peter Bachert, für die Begutachtung meiner Arbeit und die Vertretung gegenüber der Fakultät. Zudem möchte ich mich für die lange Zeit bedanken, in der Sie mich seit meiner Bachelorarbeit begleiten.

Herrn Prof. Schad, Ihnen danke ich für die Erstellung des Zweitgutachtens. Mein Dank gilt außerdem meiner restlichen Prüfungskommission, Herrn Prof. Herrmann und Herrn Prof. Bartelmann.

Des Weiteren möchte ich mich bei Ihnen, Herr Prof. Mark Ladd, herzlich bedanken. Sie haben mir meine Promotion in Ihrer Abteilung, sowie den Besuch vieler spannender Konferenzen und Workshops ermöglicht.

Ein ganz besonderer Dank gilt Dir, Sebastian Schmitter, für Deine fantastische Betreuung während der letzten Jahre. Auch wenn die Wege etwas länger waren, so hat Deine Unterstützung doch immer von Berlin nach Heidelberg gefunden. Ohne Dich würde es diese Arbeit so nicht geben. Es hat sehr viel Spaß gemacht, mit Dir zusammen zu arbeiten und ich hoffe, dass noch weitere gemeinsame Projekte folgen werden.

Danke auch an Dich, Sebastian Flassbeck, für die vielen Diskussionen und unzähligen Zeilen Code, die meine Arbeit maßgeblich vorangebracht haben. Mit Dir konnte ich stets alle meine Ideen diskutieren und Du hattest für fast jede meiner Fragen die passende Antwort. Doch nicht nur bei der Arbeit, sondern auch in unseren gemeinsamen Urlauben waren wir ein super Team. Außerdem konnte ich mich am Wochenende stets auf Deine Gesellschaft im 7T verlassen.

Mein Dank geht auch nach Rostock an Martin, Kristine und Sven. Die Kollaboration mit Euch war stets unkompliziert und es freut mich, dass ein Großteil dieser Arbeit bei Euch Anwendung findet.

Zudem geht ein großer Dank an die ganze 7T-Gruppe. Mit den richtigen Leuten macht das Arbeiten einfach gleich viel mehr Spaß. Unsere sportliche Mittagspause und unsere freitäglichen Bier um Vier haben meine Promotion sehr bereichert. Fabian, Dir gilt in dieser Hinsicht auch mein besonderer Dank für die hoffentlich noch vielen kommenden Fußballtennis-duelle.

Jana, bei Dir möchte ich mich für die vielen gemeinsamen Abende bedanken. Danke, dass Du immer ein offenes Ohr für mich hast. Du bist eine wahre Freundin für mich geworden!

Den größten Dank schulde ich meiner Familie, die mich zu jedem Augenblick bedingungslos unterstützt hat. Mama und Papa, ich hätte mir nicht mehr Zuspruch von Euch wünschen können und meine ganze Dankbarkeit in diesen wenigen Zeilen auszudrücken, ist schlicht nicht möglich. Marcel und Svenja, für Euch gilt das Gleiche. Bessere Geschwister kann ich mir nicht vorstellen. Auch meinen Großeltern gilt mein tiefster Dank. Ihr bereichert mein Leben jeden Tag. Opa Theo, die finale Version dieser Arbeit konntest Du leider nie in deinen Händen halten, aber ich schätze mich glücklich, Dir noch so viel von meiner Arbeit erzählt haben zu können.

Mareike, Du hast die letzten drei Jahre zu den schönsten meines Lebens gemacht und in Dir habe ich meine bessere Hälfte gefunden. Du bist immer für mich da und gehst mit mir durch alle Höhen und Tiefen. Dafür werde ich Dir immer dankbar sein!